NASA Contractor Report 175014

# Structure-Property Characterization of Rheocast and VADER Processed IN-100 Superalloy


Jung-Jen Allen Cheng and Diran Apelian
*Drexel University*
*Philadelphia, Pennsylvania*



June 1985

Prepared for the
Lewis Research Center
Under Grant NAG 3-14

NASA
National Aeronautics and
Space Administration

TABLE OF CONTENTS

# I. INTRODUCTION

The development of superalloys reflects a growing demand for materials with superior elevated temperature property response. Specifically, certain sections of gas turbines are constantly exposed to combinations of high temperature and corrosive atmosphere. Enhancement in the overall peformance, e.g., reliability and fuel economy, of rotating disk engine components mandates improvements in high-temperature strength and resistance to fatigue failure. It is known that turbine disk operating temperatures are generally not greater than 760°C (1400°F) (1). While stress rupture and creep strength are important, greater attention is directed to tensile strength and low-cycle fatigue response.

Both processing and alloy composition control final properties. In the late 1960's and early 1970's, gas turbine disk materials with increasing strength and operating temperature capabilities were introduced to meet increasing requirements of high-performance engines. Superalloys such as IN-100, MERL 76 and Rene 95 which are richer in alloying additions than their predecessors, were introduced. There is now a realization, however, that property improvements by alloying addition are frequently insufficient to meet the strongest requirements placed on these materials (2). Attempts to improve

property levels by increasing alloying content followed by conventional ingot metallurgy processing, such as vacuum induction melting (VIM) or vacuum arc remelting (VAR), lead to increases in both macrosegregation and microsegregation. Thus, problems arising from extensive segregation and relatively coarse grain size decrease improvements in properties that may arise from alloying additions. Moreover, such increased alloying additions frequently preclude mechanical working. Therefore, minimizing segregation and refining grain size have been the major considerations in superalloy processing for turbine disks.

One alternative is to resort to powder metallurgy (P/M) processing which leads to homogeneous fine-grained structures. Since each powder particle is a "microcasting", the extent of chemical segregation is restricted to the maximum powder-particle size and is thus reduced to the micrometer scale. These powders can be easily consolidated by a variety of techniques, such as hot isostatic pressing (HIP), extrusion or forging, e.g., Gatorizing (3). However, superalloy P/M processing and manufacturing are complex and expensive operations. In addition, high operating stress levels and long operating lives require a high level of material cleanliness to reduce inadvertent inclusions in the component (4). Unfortunately, P/M processing includes many steps where the powders are "handled" and are thus prone to contamination.

Other alternative approaches include the production of fine-scale microstructures via processes, such as vacuum arc double electrode remelting (VADER) and rheocasting (stircasting), where the

solidification phenomena are closely controlled. The VADER melting process, developed by Special Metals Corporation of New Hartford, NY, allows one to produce small, crack-free ingots with fine grain size and low levels of chemical segregation (5). Similarly, ingots of fine equiaxed nondendritic structure with reduced shrinkage and segregation can also be produced by the rheocasting process that was developed at MIT by Flemings et al. (6). The structural characteristics inherent in the VADER and rheocasting processes are recognized as factors that might improve the properties and performance of the turbine disk or permit the direct processing of ingots to shape components.

The overall objective of this thesis is to: (i) design and build a high temperature and high vacuum rheocasting furnace, (ii) prepare rheocast ingots, (iii) evaluate the effect of processing variables on the resultant rheocast structure, (iv) characterize the rheocast structure and explain the evolution of such a structure, (v) obtain VADER processed ingot and then characterize its structure and (vi) investigate the structural response to postsolidification thermal treatments and establish processing-structure-property relationships. Nickel-base superalloy IN-100 was selected for this study because it was not readily adaptable to conventional VIM/VAR processing and is currently manufactured by P/M technology. A schematic of the overall program is given in Figure 1.

## II. BACKGROUND AND LITERATURE REVIEW

### A. Nickel-Base Superalloys

Nickel-base superalloys have played an essential role in advanced transportation and power technologies for over three decades. Application of these alloys as components for aircraft, automotive and stationary power systems have permitted higher operating temperatures with resultant increased efficiencies. It is known that their use in the turbine section of an aircraft engine has increased from less than 10% of the total weight in the 1940's to an excess of 50% of the current weight of the engine (7). Today, nickel-base superalloys are used in space vehicles, rocket engines, nuclear reactors, submarines, steam power plants, petrochemical equipment and other high-temperature applications; however, their most common use is still in gas turbines (8).

Due to the challenging service environment and the alloy development in response to the needs of that development, the entire superalloy technology has been one of the most provocative of all metallurgical activities for the past 40 years. Process developments in superalloys have been equally exciting. In fact, some specific achievements in the advance of superalloys, that is, stepwise increases in the capability of superalloys, can be clearly attributed to the advent of vital process developments. The process advances in nickel-base superalloys are (a) melting and refining technologies

(9-14), (b) directional solidification (15), (c) single crystal process (15,16), (d) rapid solidification technologies, "Microcasting" (17- 22), and (e) mechanical alloying: oxide dispersion strengthened alloys (23). These process developments are further reviewed in Appendix A.

Nickel-base superalloys are the most complex of all superalloys. The simplest alloys contain Cr, Al, Ti, C, B and Zr; the most complex alloys contain several of these additional elements: Co, Mo, W, Ta, Fe, V, Nb and Hf (24). The main phases present in nickel-base superalloys are the alloy matrix $\gamma$, precipitated phase $\gamma'$ and carbides. The $\gamma'$ phase has an ordered FCC ($Ll_2$ type) structure and precipitates coherently in the FCC $\gamma$ matrix (25-32). The existence of various types of carbides is dependent upon the particular alloy composition and thermal treatment. The common classes of carbides in nickel base superalloys are MC, $M_{23}C_6$, $Cr_3C_7$ and $MC_6$ (7,33,34). In addition to main phases, other phases, such as borides (7), TCP type phases (35) and grain boundary $\gamma'$ (33,36), can also be present in nickel-base superalloys. The strength of nickel-base superalloys is mainly influenced by the relative contribution of two features--solid solution hardening of the matrix $\gamma$ and precipitation hardening due to $\gamma'$ precipitates; see Figure 2 (37-42). The general microstructures and strengthening mechanisms in nickel-base superalloys are further discussed in Appendix B.

## B. Commercial Solidification Processes for Nickel-Base Disk Superalloys

In order to produce turbine disks for early engines, nickel-base superalloys (basically wrought alloys) were first cast to form an ingot and then were hot worked into the desired shape. The wrought alloys, which have a low content of precipitation hardening elements (i.e., Ti, Al) exhibit a wide working temperature range and require relatively low flow stresses and are thus hot workable (43).

By the late 1950's, turbine engine operating temperatures were clearly limited by the operation-temperature capability of the best available wrought alloys (2). The approach taken to solve this problem was to increase the content of precipitation hardening elements. Unfortunately, increasing the concentration of alloying elements concomitantly increases the required flow stress during working, and also reduces the hot working temperature range or window (44). The picture is further complicated by the fact that these alloys are prone to excessive segregation during solidification, which diminishes their ductility and further restricts their hot workability.

In the following sections, current commercial vacuum melting and P/M technologies for the production of nickel-base disk superalloys are reviewed.

### B-1 Vacuum Induction Melting (VIM)

Vacuum induction melting for nickel-base disk superalloys was first developed by Dr. Darmara of Special Metals Corporation (New Hartford, NY) in the early 1950's. Since then, tremendous advances

have been made in VIM technology, both in the size of the melt and in process control . The VIM process minimizes the reaction of reactive alloying elements with the atmosphere and allows excellent compositional control and purity. The charge is simply melted in a crucible by induction. Sufficient pumping capacity has to be provided to maintain the chamber pressure during melting to the range of ~10 μm ($1 \times 10^{-2}$ torr). VIM processing has been reviewed in detail by Cremisio (9), Boesch et al. (5) and Pridgeon et al. (45).

The advantages of VIM over air melting for nickel-base disk superalloys are (a) prevents contact with air and minimizes inclusions, (b) removes dissolved gases and volatile constituents, (c) homogenizes melt composition by induction stirring, and (d) accelerates refining kinetics (45). However, using the VIM process in making nickel-base disk superalloys exhibits the following disadvantages: (a) solutes are segregated on a macro and micro scale, (b) an inhomogeneous grain structure and massive shrinkage are developed, (c) hot tearing takes place, and (d) ingots cannot be directly hot worked(46).

B-2. Vacuum Arc Remelting (VAR)

In the VIM process one cannot control the solidification structure, but rather the aim is to attain the desired chemistry and purity; whereas in the VAR process one controls the solid-liquid interface motion, specifically, the width of the mushy zone and the local solidification time. In VAR, the VIM ingot that is the electrode is positioned vertically and remelted into a water-cooled metal crucible. The energy for melting is generated by electric arcs that are

struck between the bottom of the electrodes (usually the cathode) and the ingot top surface (usually the anode). Metal is transferred to the crucible drop by drop and the VAR ingot is slowly built up. Solidification in the VAR process is directional because heat is extracted from the bottom of the molten metal pool.

The VAR process exhibits the following advantages over the ViM process: (a) controlled mushy zone length, (b) refined grain size, (c) Shorter local solidification time, (d) Reduced macrosegregation and (e) elimination of shrinkage pipe(5,9,45).

The advantages of VAR are overshadowed by two major disadvantages: macrosegregation and nonuniform grain size in the ingot. The deleterious segregate phases that diminish the ingot's hot workability are "tree rings" and "freckle" segregates (39). These result from interdendritic liquid that are rich in solute content. The nonuniform grain size in the ingot results in a poor distribution of second phases (42).

B-3. Powder Metallurgy (P/M)

In the late 1960's and early 1970's, gas turbine disk materials with increasing strength and operating temperature capabilities were introduced to meet increasing requirements of high performance. Alloys like IN-100, MERL 76, Rene 95 and AF 115, which are rich in alloying additions, are prone to excessive segregation and suffer from poor workability after VAR. The local solidification time for these alloys needed to be reduced substantially from that obtained by VAR processing. This was achieved through powder metallurgy.

In powder metallurgy, the first breakthrough was the ability to produce clean prealloyed powders in commercial quantities. Such a powder particle is in fact a "microcasting", and the particulates can be easily consolidated by a variety of processes (e.g., sintering, HIP, hot extrusion, forging and cold pressing) and may be densified to net shape without any postdensification deformation (19,46). Furthermore, the compacted powders can be subsequently hot extruded to give rise to an ultrafine grain size. This fine recrystallized grain structure exhibits high superplastic behavior when deformed at high temperatures under appropriately low strain rate conditions, e.g., Gatorizing (3).

P/M processing of nickel-base superalloys offers the following advantages when compared to conventional vacuum casting processes: (a) extremely fine grain size, (b) reduced Microsegregation, (c) drastically reduced segregate spacing (microsegregation), which enables the component to be homogenized upon thermal procersing, and (d) hot workability.

There are, however, several problems with P/M processing. In practice, it has been found that the maximum allowable operating stresses are not only dependent on major alloying elements but are also limited by the defects present in the powders. Moreover those defects cannot be detected by current NDT techniques (2). The defects may be ceramic particles or organic particulates. Utilizing finer powder fractions can reduce the defect size, but their elimination cannot be guaranteed (47). Furthermore, powder handling is not only a costly operation (due to the requirement of clean-room processing, glove boxes and other cleanliness conditions), but also a serious

safety hazard (4).

C. Vacuum Arc Double Electrode Remelting (VADER)

The VADER process, patented by Special Metals Corporation (48), is a potential alternative to P/M processing. A schematic diagram of the process is shown in Figure 3. In VADER, an arc is established between two consumable electrodes and the molten metal is allowed to drip into a stationary, rotating or withdrawing mold located beneath the electrodes. The metal drips from the faces of the two electrodes, and essentially these droplets are consolidated in-situ in the mold. The droplets fall with very little, if any, superheat. In fact, droplet temperature measurements indicate that they are slightly below the liquidus temperature of the alloy, e.g., droplet temperature measurements on IN-718 alloy were found to be 11°C (20°F) below the liquidus temperature as measured by DTA analysis (45). Accordingly, it is suggested that metal droplets contain solid particles or nuclei as they fall into the mold (4,5,45). However, the origins of the solid particles or nuclei formed in the metal droplets are still uncertain. Further work is needed to understand the exact mechanism of VADER processing.

VADER processed ingots of nickel-base superalloys consist of equiaxed nondendritic fine grains (4,5). The formation of fine-grained VADER castings is explained by the hypothesis of numerous nuclei being present in the semiliquid mass and subsequent grain growth being interfered with by precipitated phases. The VADER process has the following benefits compared to conventional VIM-VAR processing:

(a) uniform fine grain size (typically 100 μm), (b) reduced macro-segregation, (c) less prone to internal cracking, (d) improved hot workability, (e) more energy efficient (5).

## D. Rheocasting (Stircasting)

Rheocasting is another process that may improve the hot workability of nickel-base disk superalloys. In the subsequent sections, rheocasting applications (D-1), rheocast structure (D-2), the mechanism controlling the evolution of the rheocast structure (D-3) and mechanical properties of rheocast products (D-4) are reviewed.

### D-1. Rheocasting Applications

Rheocasting, a casting of semisolid slurries, was invented and developed at MIT by Flemings et al. (49). Rheocast slurries are thixotropic and show a hysteresis loop phenomenon similar to other well-known thixotropic systems (50). The concept of rheocasting is explained by the use of a simple eutectic phase diagram (Figure 4). While the melt is cooled through the mushy zone, it is mechanically stirred; subsequently, the melt is held at a given temperature (corresponding to a certain fraction solid) - isothermal hold - while it is continuously sheared. Rheocast metal has been produced continuously at volume fractions solid ranging up to about 70% (49). After shearing, the rheocast slurry may be cast into a receiving crucible, for example, through bottom pouring (continuous), or it may be allowed to solidify in the original processing crucible (batch). The resultant cooling rates will obviously differ. Various different alloys have

been rheocast in either batch or continuous mode. Work has been reported on Al-base (30,51,52), Cu-base (53), Pb-Sn (54), Fe-base (55), Co-base (56) and Ni-base (57) alloys. The basic rheocasting concept has been extended to produce composite materials and wrought-slurry castings similar to squeeze casting. Some of the more notable processes that have derived from the rheocasting process are compocasting (58), thixocasting (6) and thixoforging (59).

D-2. Rheocast Structure

Dendritic solidification, which arises because of the break-down of the plane front solid-liquid interface, is well established and has been reviewed in detail (14,60). The evolution of the grain structure in a casting is also well understood and that there is a relationship between the size of the dendrites and the resultant grain size (60). The conventional dendritic structure is altered by manipulating the processing condition. For example, Kattamis et al. (61) have shown that magnesium alloys, grain refined by zirconium catalysts, exhibit a spherical morphology where grains have a size equal to that of the dendrite arms. Also, by fragmenting the dendrite arms by rheocasting, one can produce a cast structure having an equiaxed nondendritic morphology (50,54).

Rheocast structures have been shown to be affected by four independent variables: shear rate, cooling rate, stirring time and volume fraction of primary solid particles (6,49-59,62-65). However, these observations and explanations are focused on the resultant structures that were obtained by stirring in the mushy zone and

subsequently water quenching the casting. It has been concluded that:

- The primary solid particle size decreases as the shear rate, cooling rate or stirring time increases. In addition, as the volume fraction solid increases, one observes larger primary solid particles.

- Particle shape is strongly affected by shear rate, stirring time and volume fraction solid. Increasing shear rate, stirring time or volume fraction solid results in an increase in the sphericity of the primary solid particles.

Furthermore, rheocast structures offer the following advantages over conventional cast structures (14,49):

- Reduced shrinkage and potential of crack formation
- Microporosity, if present, is uniformly distributed
- Formation of a fine and nondendritic grain structure
- Reduced segregation.

D-3. Mechanism of Rheocasting

Various hypotheses, such as dendrite arm remelting, mechanical fracture of dendrite arms and enhanced nucleation, have been reported as mechanisms giving rise to the rheocast structure. Unfortunately, none of them have been seriously studied and confirmed. Vogel et al. (65), however, have proposed a model for the fragmentation of the dendrites during stirring based on the formation of high-angle grain

boundaries in the dendrites following bending of the dendrite arms. Due to fragmentation of the dendrites, the effect of stirring would change the primary solid particle morphology from purely dendritic to spherical. This model, known as the Vogel-Doherty-Cantor model, has been studied and confirmed by Lee (52). Recently, Doherty et al. (63) reviewed the literature on the development of the rheocast structure and presented some new evidence in support of the model for rheocasting. Highlights of their findings are discussed below.

Vogel et al. (64) showed that the solute gradient ahead of the primary solid particle became steeper with stirring since the thickness of the solute-enriched layer was reduced due to stirring. Because of this, the propensity of the solid-liquid interface to be unstable increases, giving rise to dendritic solidification. However, nondendrite spherical primary solid particles have been observed (6). This conflict has been explained by Vogel (30), who pointed out that a high density of growing particles gives rise to shape stability by virtue of a reduction in the thermal and solute gradients, because of "soft impingement" of the diffusion field between adjacent growing particles. As a consequence, Doherty et al. (63) concluded that the observed shape stability in rheocastings must arise from the high density of growing particles.

Spencer et al. (54) showed that a Sn-15 w/o Pb alloy behaved as a normal metallic solid with a significant shear strength when partially solidified without stirring at solid volume fraction of more than 20%. However, after plastic shear strains had been imposed on the two-

phase dendritic structure, the strength of the mixture rapidly collapsed to give liquidlike (slurry) mechanical properties. Microstructural studies by Spencer et al. (54) showed that the initial dendritic structure was fragmented by stirring the partially solidified alloy. The result was a high density of almost spherical solid particles. In addition, many of the spheres contained trapped liquid. Similar structures were also produced by stirring while the alloy was cooled from above the liquidus temperature (50,53,65). However, it was not certain whether these high-density spherical particles were formed due to enhanced primary nucleation or dendrite fragmentation. Vogel et al. (65) observed no significant increase in the number of nuclei when stirring was applied during the early stages of freezing, and therefore have suggested that the formation of the additional number of small particles is due to dendritic fragmentation only. However, their observations were based on the results of a single experiment. Therefore, before further studies are completed, the possibility of the formation of high-density spherical particles due to enhanced primary nucleation during stirring cannot be ruled out.

Joly and Mehrabian (50) have also reported that at low shear rates clusters of primary solid particles build up, whereas at high shear rates such clusters break up. However, they did not offer a comprehensive model of the development of the rheocast structure. Vogel et al. (65), on the other hand, have proposed a model that attempts to account for both the initial fragmentation of the dendrites and the Joly-Mehrabian clustering reactions. The model is based on the

formation and melting of grain boundaries, produced either by deformation or by sintering. Figure 5 shows the schematic model of this grain boundary fragmentation mechanism. The dendrite arm in soft ductile material is first bent through an angle $\theta$ when exposed to turbulent fluid flow. This plastic bending will introduce large misorientations into the dendrite arms. Such disloca- tions, if randomly distributed, will have a high elastic energy, which can be reduced by the migration of the dislocations to form grain boundaries. If a grain boundary has an interfacial energy $\gamma_{gb}$ greater than twice the solid-liquid interfacial energy $\gamma_{S-L}$, the grain boundary will be replaced by a thin layer of liquid, and thus the dendrite will break apart along the prior boundary. On the other hand, if a boundary forms with $\gamma_{gb} < 2\gamma_{S-L}$, the boundary should survive and remain in the microstructure such that it can be detected metallographically.

A considerable quantity of evidence has been produced in support of the Vogel-Doherty-Cantor model (30,52,63,65,66). Some of the evidence is listed below:

(i) Bent but unrecrystallized regions have been observed within rheocast particles.

(ii) Grain boundaries have frequently been seen within isolated rheocast particles.

(iii) Most of the grain boundaries observed were indeed the expected low-angle boundaries (less than 15°), and the remainder were large-angle but low-energy boundaries, such as twin boundaries

or boundaries that were known from sintering experiments done by Gleiter et al. (67). It is known that two separate solid particles could sinter together if they came into contact at a relative misorientation corresponding to a low-angle boundary.

(iv) In rheocast materials, two types of solute profile have been detected at grain boundaries. One profile shows no segregation of solute at the boundary, which is expected for boundaries resulting from recrystallization; the other profile shows a local peak in solute content, which is expected for boundaries resulting from sintering (52,63).

(v) Large-angle grain boundaries can indeed be produced by the hot bending of single crystals of high-purity aluminum (52).

Even though some features of the fragmentation phenomenon have been shown above to support the Vogel-Doherty-Cantor model, the following questions about the model have not yet been addressed and require investigation:

(i) All evidence given so far has only confirmed that low-energy boundaries did exist inside primary solid particles of the rheocast structure. However, the effect of processing variables(e.g., stirring time) on the quantity of low-energy boundaries has not been qualitatively or quantitatively studied. It is expected that the movement of a grain boundary may be rapid at such a high temperature in the solid-liquid phase region.

(ii) Will low-angle grain boundaries still survive or be detectable inside rheocast grains after the sample has been furnace cooled instead of water quenched to room temperature?

(iii) This model is suitable only to explain the morphology change of ductile primary solid particles by stirring during solidification. It does not consider the response of brittle primary solid particles, e.g. Fe- or Si- rich primary solid particles in the solidification of hypereutectic alloy systems, upon the process of rheocasting. Those brittle solid particles may be mechanically fractured immediately after bending.

(iv) In this model, it is suggested that a thin layer of liquid will replace the unstable high-energy grain boundary and the dendrite will break apart along the prior boundary. However, the speed of the liquid penetrating through the grain boundary has not been considered at all. Roques-Carmes et al. (68) have investigated the penetration of aluminum grain boundaries by liquid gallium and have shown that the speed of penetration is very rapid (e.g., it took about 5 minutes to penetrate a distance of 2 mm at a temperature of 120°C). Accordingly, in rheocasting the dendrite arm formed at the early stage of solidification is so fine that it can take less than a second for liquid to penetrate the boundary in the dendrite arm. However, it has also been suggested that the resistance to grain boundary sliding under stirring-induced shear force at a temperature near the melting point of the material can be expected to be extremely small. After the grain

boundary is formed inside the dendrite arm by plastic bending, the dendrite may break apart simply because ofgrain boundary sliding with no requirement of the grain boundary energy or even before the liquid could actually penetrate the grain boundary. Therefore, to clearly understand the exact mechanism of dendrite arm fragmentation during rheocasting, further qualitative and quantitative investigations are needed.

D-4. Mechanical Properties

The mechanical properties of various rheocast alloys have been reported by Flemings et al. (69) and have recently been reviewed by Lee (53). The structures evaluated consisted of duplex structures (i.e., coarse and spherical primary solid particles surrounded by fine and dendritic liquid phase) that were produced by stirring during solidification and subsequent water quenching.

All the rheocast duplex structures were reported to exhibit tensile properties lower than those of conventionally cast or wrought alloys (52,69). Lee (52) suggested that the large quantity of sheet-shaped oxides and impurity particles developed in the rheocast alloys is likely to be responsible for the poor tensile properties of Al-base alloys. The effect of stirring on the fracture toughness in Al alloys has also been studied by Vogel (30) and Lee (52). The results indicate that the rheocast structure is tougher than the conventionally cast product (30,52). Doherty (70) suggested that the fracture toughness in rheocast alloys is improved because the crack path is modified by the

presence of large, soft spherical primary solid particles in the hard liquid matrix. In addition, Lee et al. (52) pointed out that the reduction of porosity by stirring appeared to be another contributing factor.

E. Healing of Casting by Hot Isostatic Pressing (HIP)

HIP, which is routinely used to consolidate and manufacture near net shape parts in P/M, has been found to be the only effective way to eliminate microporosity and voids in castings (71). Densification parameters in the HIP process are pressure, temperature and time. HIP collapses voids and porosity by creep or plastic deformation (72). It not only creates a fully dense casting but also improves the structural homogeneity of the casting (73). HIP does not usually affect dimensions since the pores are small (74). However, HIP has the limitation that it cannot heal the surface-connected porosity (75). A more detailed review of the HIP process is given in Appendix C.

F. Mechanical Properties of Nickel-Base Turbine Disk Superalloys

Turbine disks operate at temperatures below 750°C (1400°F) (1); the maximum temperature occurs at the outer edge or rim of discs. In the hub section, toward the center of the disk, temperatures are much lower. Materials therefore require sufficient tensile strength. In addition, fatigue resistance is a parameter that cannot be ignored. Low-cycle fatigue (LCF) is considered to be the life-determining property for turbine disks.

F-1. Tensile Properties

As was discussed in section A of this chapter, nickel-base superalloys are strengthened mainly by solid solution hardening of γ and precipitation hardening of γ'. In addition, carbides, which appear to nucleate preferentially at grain boundaries, have a significant and beneficial effect on high-temperature strength and their morphology influences the ductility level of the alloy (7,42,78-80). Other phases, such as TCP phases, borides and grain boundary γ' denuded zone, also have a specific effect on the properties of the alloy (36,71,79,81-83). The grain size of the alloy also exhibits a great effect on the tensile properties of superalloys. It has been shown that decreasing grain size increases the yield and ultimate tensile strength; however, it decreases the ductility at a testing temperature of 650°C (1200°F) (84). Furthermore, cast nickel base superalloys respond favorably to HIP (85). More details of tensile properties affected by the above additional factors in nickel-base disk superalloys are reviewed in Appendix D.

F-2. Low-Cycle Fatigue (LCF) - Fatigue Crack Propagation (FCP) Rate

Fatigue is usually the life-limiting factor for modern aircraft turbine engine disks. Good resistance to FCP is important, as well as resistance to crack initiation. Of particular interest and importance to the industrial sector are the kinetics of crack propagation. For example, there is a schedule of NDT inspections to detect defects

(cracks) and flaws, and it is important to ensure that crack initiation and propagation to failure will not occur prior to the next scheduled inspection.

The FCP rate (da/dn) can be correlated with the stress-intensity factor range ($\Delta K$) according to the Paris-Erdogan relationship (86):

$$da/dn = C\Delta K^m \qquad (1)$$

where

a: crack length

n: number of cycles

$\Delta K$: stress-intensity-factor range, ($\Delta K = K_{max} - K_{min}$)

C,m: function of testing conditions

Clearly, the FCP rates are primarily a function of $\Delta K$ (86-88). However, the load ratio ($R_{ratio} = K_{min}/K_{max}$) (87,89,90), loading variables (i.e., cyclic frequency and wave form) (91,92), testing temperature and environments (84,91-97), and microstructures (71,84,92,97-104) can also significantly affect the FCP rates. The microstructures that have been studied include grain size, $\gamma'$ particle size and grain boundary phases and morphology. At constant testing conditions and constant $\gamma'$ particle size and volume fraction of fine $\gamma'$, it has been shown that increasing grain size reduces the FCP rate (84). A fine grain size promotes rapid intergranular crack propagation, while a coarse grain size promotes slower, transgranular crack growth. The effects of these factors on the FCP rates of nickel-base

disk superalloys are reviewed in Appendix D.

# III. EXPERIMENTAL PROCEDURE

## A. Materials

The nominal composition of the as-received IN-100 ingot that was subsequently rheocast is shown in Table I. All the chemical analyses in this study were carried out at Cabot Corporation, Kokomo, IN. The carbon content of the alloy is 0.06 w/o, which is lower than that of the commercial cast IN-100, i.e., 0.18 w/o. All the as- received ingots were made by the VIM process and were purchased from Cannon Muskoegan.

The VADER ingot, which was processed at Special Metals Corp. of New Hartford, NY, was also a low carbon IN-100 alloy. The composition of the VADER ingot is also given in Table I.

## B. Solidification Apparatus and Processing

### B-1 Rheocasting of IN-100 Nickel-Base Superalloy

It is complicated to rheocast nickel-base superalloy because the design of the rheocasting apparatus has to meet the following major requirements:

(i) a high-temperature furnace to melt IN-100 alloy.

(ii) a high-vacuum environment throughout the whole operation of melting, stirring and furnace cooling. A special design of stirring shaft and a high-vacuum seal are needed.

(iii) high-quality crucibles and stirring paddles that can be

used at a temperature higher than 1400°C (2550°F).

(iv) an immobile crucible assembly during stirring.

(v) a good temperature control during rheocasting.

A GCA vacuum hot-press furnace was modified to a high-vacuum rheocasting furnace. A schematic diagram of the apparatus is shown in Figure 6. A ferrofluidic vacuum rotary feed through seal was used, which transmitted 100% positive rotation into the vacuum chamber by means of a solid through-shaft design and a Ferrometric (magnetic) seal. A more detailed schematic of the crucible assembly is shown in Figure 7, where the various components are indicated. A photograph of the total assembly ready for a rheocasting run is shown in Figure 8. Note that a plate (indicated by "X") in Figure 8, is placed on top of the crucible assembly and is held down by four high temperature bolts and springs. This ensures that the crucible is held down and is immobile while the paddle is rotated.

The charge was induction melted in a crucible. A 30 kw Inductotherm unit was used; the $Al_2O_3$ crucible was heated by the use of a graphite suceptor. At the 12 o'clock position of the vacuum chamber (Figure 6), an annular stainless steel tube was installed, which performed three functions: permitting vertical motion of the stirrer, functioning as a water-cooling jacket, and maintaining the vacuum at all times. Within the stainless steel water cooling jacket, a stainless steel rotating shaft, which was attached to a ferrofluidic seal shaft, was immersed at the 6 o'clock position within the jacket. This shaft was connected to the alumina stirrer paddle.

In order to maintain a constant seal, the water-cooled jacket was welded to a flange, which in turn was fastened to the ferrofluidic casing. The rotational movement of the inner shaft was provided by a variable speed motor connected via a belt to the pulley and was mounted in the rotating shaft. The tool assembly was coupled to a hydraulic piston that provided the vertical motion of the paddle.

At the temperature corresponding to the desired fraction solid, the paddle was lowered into the crucible via the hydraulic ram, and then the driving belt was engaged. Upon completion of the stirring action, the pulley was disengaged and the assembly was raised vertically via the hydraulic ram. The prepared rheocast slurry was left to solidify in the crucible.

The crucible was made of high density and high-purity alumina ($Al_2O_3$). The crucible had an inner diameter of 3 7/8" (9.9 cm), height of 7 5/8" (19.4 cm) and wall thickness of 1/8" (0.3 cm). The stirring paddle was also made of high-density and high-purity $Al_2O_3$, which was cut to size to fit the alumina crucible, ensuring a maximum clearance of 1/2" (1.3 cm) on both sides and the bottom of the paddle. A photograph and a schematic diagram of the paddle and crucible are shown in Figure 9. It has been calculated by Lee (52) that, when a hollow rotor is used to stir Al-base slurry, the estimated average shear rate increases as the clearance between the rotor and the crucible wall decreases. Accordingly, in these rheocasting experiments a clearance of 1/2" (1.3 cm) was selected and provided adequate stirring. The paddle had a rectangular shape and was 2 7/8" (7.3 cm)

wide, 1/2" (1.3 cm) thick and 10 1/2" (26.7 cm) long. Cracks were observed on the surface of both the crucible and the paddle after furnace cooling, and therefore crucibles and paddles were used only once for a given run.

Two to four W-5% Re/W-26% Re thermocouples were inserted through the wall of the graphite suceptor, which touched the outside wall of the alumina crucible at different locations along its length, Figures 7 and 8. A strip-chart recorder was used to obtain continuous temperature-time curves during melting and subsequent rheocasting. To establish the temperature difference between the liquid metal and the outside wall of the crucible, a temperature calibration run was made a priori. An as-received IN-100 ingot was melted in vacuum and held at a temperature of 30°C (54°F) above the liquidus. Two thermocouples were placed into long alumina tubes (one end closed) and slowly lowered into the melt until they reached positions 1/2" and 2" (1.3 cm and 5.1 cm), respectively, above the bottom of the crucible. The furnace power was then lowered and the temperature reading for each thermocouple was recorded. The thermal profiles during solidification for all of the thermocouples are shown in Figure 10.

The processing approach and the variables that were evaluated are shown in Figure 11. As is indicated by a vertical arrow in this Figure, the stirring was initiated while the charge was completely molten. The temperature at which the slurry was equilibrated and stirred for a period of time ($t_s$) was dictated by the desired fraction solid in the slurry. The lower the temperature within $T_L$ and $T_S$, the higher the

fraction of solid present in the slurry. In order to obtain the relatonship of volume fraction solid as a function of temperature, a differential thermal analysis (DTA) of IN-100 was carried out at Special Metals Corporation. Three samples in the as-received VIM condition were analyzed. Figure 12 shows the thermal analysis, $\Delta T$ versus T, of IN-100. The liquidus, solidus and $\gamma'$ solvus temperatures are shown. At any temperature in the mushy zone, the ratio of the shaded area (Figure 12), to the total shaded area gives an estimate of the fraction of liquid present at that temperature. The resultant volume fraction solid ($f_s$), which was present as a function of the temperature in the mushy zone, is shown in Figure 13.

The process variables examined were:

(i) Fraction solid, $f_s$- maintained at 35%, 50% and 65%.

The highest volume fraction solid of 65% was selected because at the volume fraction solid of 70%, the stirring paddle kept collapsing.

(ii) Stirring speed, $\gamma$ - stirred at 325, 450 and 560 rpm.

The stirring speed of 560 rpm was the upper limit. Above this limit the slurry splashed out on the inner surface of the furnace chamber.

(iii) Isothermal stirring time, $t_s$ - held at 15 and 45 minutes while stirring.

These two isothermal stirring times were chosen simply to study the effect of isothermal stirring time on the structure and properties of rheocast ingots.

The following procedure was used during rheocasting. The furnace chamber was evacuated to about $4 \times 10^{-2}$ μm ($4 \times 10^{-5}$ torr) by means of mechanical and diffusion pumps. The power to the induction unit was then turned on. In order to fully melt the charge, the power was raised to a maximum of 5 kw. Upon complete melting of the charge, the vacuum was increased to 0.6 μm ($6 \times 10^{-4}$ torr); this level of vacuum was maintained throughout the rheocasting operation. The paddle was then lowered into the melt to its proper stirring position and rotated. Simultaneously, the alloy was slowly cooled with a constant cooling rate through its solid-liquid temperature range. When the temperature corresponding to the desired volume fraction solid was reached, the temperature was equilibrated and the slurry was stirred for a given period of time, $t_s$. Finally, for runs stirred at the volume fraction solid of 35%, the paddle was immediately raised out of the crucible when the stirring was terminated and the slurry was allowed to completely solidify in the furnace. However, for runs stirred at the volume fractions solid of 50% and 65%, the slurry became viscous and the paddle could not be raised from the slurry. As a consequence, for those runs stirred at 50% $f_s$ and 65% $f_s$, the slurry was simply furnace cooled without lifting the paddle.

During the initial runs, both crucible and paddle failed. The crucible collapsed when the power rate was rapidly increased. It was found that a rate of 1 kw/hr was the maximum allowable rate while minimizing thermal shock. The stirring paddle also collapsed when it was lowered into the melt. To prevent the stirring paddle from

failuring, the following two additional steps were taken: (i) during melting of the charge, the paddle was preheated by lowering it to a position just above the melt surface, and (ii) subsequently, the paddle was lowered into the melt slowly, 1 cm/min.

Table II lists rheocasting runs made under different processing variables. The solidified ingots with or without the rotating paddle, were sectioned for structural characterization studies and post solidification thermal treatments. A schematic diagram of the sectioning mode is shown in Figure 14.

B-2 Vacuum Arc Double Electrode Remelting (VADER)

The microstructure and mechanical properties of the rheocast ingots were evaluated and compared to the VADER cast ingots. A schematic of the VADER melting process is shown in Figure 3. In the VADER process, two consumable electrodes, which could be either VIM or electron beam refined ingots, are arced against each other with no additional power input into the remelted pool. The molten metal is allowed to drip into a stationary mold located under electrodes. The arc polarity can be reversed to offset the different consumption rates between the cathode and anode (abour 10%). The mold can be rotated up to 100 rpm to distribute droplets and create a uniform metal meniscus. The experimental unit utilized at Special Metals Corp. was capable of producing products ranging from 4 to 12 inches (10 to 30 cm) in

diameter and up to 150 lbs (68 kg) in weight.

A 100 lb (45.5 kg) ingot of IN-100 Ni-base superalloy was produced by the VADER process at Special Metals Corporation. In order to characterize the structural features and to evaluate the material's crack propagation resistance, the VADER ingot was sectioned into 10 specimens, as shown in Figure 15.

C. Postsolidification Thermal Treatments

C-1 Hot Isostatic Pressing (HIP)

Ingots made from runs #6 (nonstirred), #10, #20 and #26 (Table II) were cut vertically into two sections. One section from each run listed above together with ingots made from runs #19, #22 and #29 and VADER (Table II) were then subjected to HIP at 15 ksi (103.4 MPa), 1180°C (2160°F) for 3 hours. The HIP pressure and time used were those for commercial nickel-base superalloys. The HIP temperature depends on the γ' solvus temperature, and in order to find out the "correct" temperature, nonstirred, rheocast and VADER specimens were homogenized at 1180°C (2160°F) and 1200°C (2190°F) for 3 hours under an argon atmosphere. A K-type (Alumel-Chromel) thermocouple was inserted into each sample to control the temperature of the specimen at the accuracy of ±0.6°C (1°F) during isothermal holding. The resultant microstructures were examined, and based on this analysis, a HIP temperature of 1180°C (2160°F) was chosen.

HIP of the samples was carried out at Special Metals Corporation. Four Pt-Pt 10% Rh thermocouples were placed adjacent to the ingots to

monitor the temperature. The temperature was controlled at 1180°C ± 20°C (2160°F ± 35°F). The HIP ingots were subsequently cooled in the furnace under an argon protective atmosphere.

C-2 Heat Treatment

The HIP ingots were then heat treated in a commercial salt solution; the heat treatment was carried out at Carpenter Technology Corporation, Reading, PA. The heat treating cycle included a solution treatment and three aging treatments as listed below:

- Solutionizing at 1120°C (2050°F) for 2 hours and oil quenching
- Primary aging at 870°C (1600°F) for 0.67 hours (40 minutes) and air cooling
- Secondary aging at 650°C (1200°F) for 24 hours and air cooling
- Final aging at 760°C (1400°F) for 4 hours and air cooling.

The above cycle is the heat treatment cycle also used by the NASA Lewis Research Center for processing of their commercial P/M IN-100 superalloy components.

D. Specimen Preparation and Mechanical Testing

D-1 Tensile Test

Two specimens cut from each heat treated HIP ingot were machined and subsequently tensile tested. Figure 16 indicates the locations in each ingot from which the specimens were sectioned. A

schematic diagram of the test specimen, which conforms with the specifications given by ASTM E8, is shown in Figure 17. Testing was carried out at a cross-head speed of 0.05 inch/minute (0.127 cm/minute) in a standard Instron machine at 650°C (1200°F); protective atmosphere was not provided. All of the tensile testing was done at the NASA Lewis Research Center. Percent elongation (with a 1.15-inch (2.92-cm) gage), yield strength (0.2% offset) and ultimate tensile strength were determined.

D-2 Fatigue Crack Propagation (FCP) Rate Test

Compact tension (CT) specimens, as shown in Figure 18, were used for the FCP rate test. These samples were sectioned and subsequently machined from heat treated HIP ingots. The specimen locations in each ingot are illustrated in Figure 16. Due to the size of the ingot, the dimensions of the CT specimens were modified as shown in Figure 19.

All of the FCP rate testing and evaluation were also done at the NASA Lewis Research Center, because of the superior testing equipment available. CT specimens were precracked at room temperature according to guidelines set forth in ASTM E647-78T and subsequently tested at 650°C (1200°F) in air under load control using a 0.33 Hz triangular waveform and an R ratio (minimum load/maximum load) of 0.05.

In addition to the specimens of ingot material, specimens from P/M IN-100 superalloy were also machined and tested. The P/M data

were provided by NASA Lewis Research Center, and were prepared by the Gatorizing process, in which powder is hot compacted, extruded and then isothermally forged at a low strain rate where material behavior is superplastic (3).

## E. Structural Evaluation

### E-1 Reheating Experiment

To clearly distinguish between the primary solid phase that had been present during rheocasting and the liquid phase surrounding the primary solid phase, a set of reheating experiments was carried out. The reheating experiments were performed in a high-temperature tube furnace; a quartz tube of 2" (5.08 cm) diameter (I.D.) and 36" (91.44 cm) long was used. To prevent oxidation, the experiments were carried out in an argon environment. A Pt-Pt 10% Rh thermocouple was placed into the tube such that the thermocouple tip was adjacent to the sample. The sample was heated to the temperature at which it had been rheocast, $T_{fs}$ (see Figure 11), and then isothermally held for a period of 5 minutes. Subsequently, the sample was quickly removed and water quenched. For the purpose of comparison, samples obtained from nonstirred ingots were also included in the study. An isothermal temperature corresponding to a volume fraction solid of 35% and periods of 5 and 20 minutes were used for the nonstirred specimens in the reheating cycles.

E-2 Structural Characterization

The surfaces of the nonstirred (run #6), rheocast and VADER ingots were ground and then macroetched in a solution of HCl, $H_2O$ and $H_2O_2$ in a ratio of 5:5:2, respectively. Pictures of macrostructures were taken by a simple light microscope. For microstructure studies, several samples were sectioned from different locations of each nonstirred, rheocast and VADER ingot. In addition, one sample was sectioned from each HIP and HIP plus heat treated ingot. These samples were then mounted and hand polished through 600 grit abrasive paper, followed by a final polishing using 6-μm and 1-μm diamond pastes. Glycergia etch (10 ml glycerin, 15 ml HCl and 5 ml $H_2O$) was used as an etchant. Optical and scanning electron micrographs were obtained at different magnifications. The K ratio profiles of segregation were studied through X-ray analysis using wavelength dispersive spectroscopy (WDS). The K ratio is an intensity ratio and is defined as follows:

$$K = \frac{\text{intensity of sample primary emission}}{\text{intensity of pure element standard primary emission}}$$

This calculated K ratio is roughly proportional to the actual composition of the solute in the alloy and is used here for relative comparison. Two solutes, Ti and Cr, were selected for this segregation study.

The fracture surfaces of CT specimens were examined with a scanning

electron microscope (SEM). The fractographs of CT specimens were taken along the center line of the specimen. Optical micrographs were also used to characterize fracture morphology. Sections perpendicular to the direction of crack propagation were cut from the CT specimens, mounted, polished and subsequently etched in a Glycergia agent.

### E-3 Microhardness

The microhardness values for lightly etched samples were obtained using a LECO M-400 microhardness tester. Microhardness values were taken at the center and near the boundaries of the grains for each IN-100 specimen that was sectioned from ingots before and after postsolidification thermal treatment.

## IV. RESULTS AND OBSERVATIONS

This section is divided into three major subsections: processing (A); HIP and thermal treatments (B); and mechanical properties (C). Microstructural analysis results of the differently processed (VADER and rheocast) IN-100 alloy are presented in Section A. Specifically, in section A-1 the results from the nonstirred casting are given; section A-2 addresses the rheocast structures processed; and the microstructural analysis of the VADER processed IN-100 is given in section A-3.

### A. Processing of VADER and Rheocast IN-100 Alloy

#### A-1 NonStirred Casting (Table II - Run #6)

The longitudinal macrostructure of the nonstirred ingot is shown in Figure 20(a). Essentially the VIM as-received charge was remelted in the rheocasting apparatus without stirring. The macrostructure of the top region of the ingot consists of columnar grains; the bottom region, fine-equiaxed grains; and the center region, coarse-equiaxed grains and large shrinkage cavities. Many interconnected cracks are present around the whole ingot.

Micrographs in Figure 20(b) represent the structures from the locations indicated by arrows in Figure 20(a) of the nonstirred ingot. The grains are clearly dendritic, with sizes ranging from approximately

1500 μm in region A to approximately 200 μm in region C. The dendritic arm spacing is ~120 μm in region C and is ~200 μm in region A. The voids are located randomly along the interdendritic regions and grain boundaries; in addition, they are irregular in shape and size. The amount of these pores is maximum in region C and minimum in region A.

The phases found in the IN-100 ingot consist of primary or eutectic γ-γ' islands and MC carbides, which are all surrounded by secondary precipitated γ' in the matrix of γ. The size, distribution and morphology of these phases in the nonstirred ingot are shown in Figure 21. The γ-γ' eutectic islands, located at the interdendritic areas and grain boundaries, represent the final solidified regions. These islands vary in size and shape and are nonuniformly distributed in the nonstirred ingot. Most of the carbide particles are scriptlike, and only a few of these particles were observed to be blocky. The voids are always accompanied by the γ-γ' eutectic islands or carbide particles, Figure 21(b).

Representative SEM micrographs of secondary precipitated γ' inside the dendrite arms and near the boundaries are shown in Figures 22(a) and 22(b), respectively. The γ' particles located inside the dendrite arms exhibit both the cuboid and facet dendritic shape, with a particle size of approximately 0.2-0.7 μm, Figure 21(a). However, the γ' particles located near the boundaries are irregular in shape, with particle size ranging from 1 μm to 3 μm (coarser than the particles located within the dendrite arms). The volume fraction of γ' is approximately 60% throughout the sample.

The segregation ratio, in general, is defined as $C_{max}/C_{min}$, where $C_{max}$ is the highest solute content and $C_{min}$ is the lowest solute content in a dendrite or grain. However, due to the complexity of the grain boundary phase, the actual segregation ratio in a dendrite or grain is difficult to obtain. Therefore, the composition ratio, $S = C_{mid}/C_o$, where $C_{mid}$ is the solute content at the midpoint between the center and boundary of a dendrite or grain and $C_o$ is the solute content at the center of a dendrite or grain, was selected as the segregation ratio for the purposes of comparison. Table III illustrates the segregation ratio of Cr and Ti in the nonstirred ingot. Among 20 arbitrarily chosen dendrite arms, the evaluated segregation ratios show scatter for both Cr and Ti. The mean and standard deviation of Ti and Cr segregation ratios in the nonstirred ingot are $1.31 \pm 0.09$ and $1.07 \pm 0.02$, respectively (Table IV). Figure 23 shows a representative K ratio profile of segregation in the dendrite arms of the nonstirred ingot.

A-2 Rheocasting

The structures of the various rheocast ingots of IN-100 are shown in Figures 24 through 31. These structures were obtained by cooling the IN-100 superalloy, while vigorously stirring the melt or slurry, from its liquidus temperature down to a selected temperature corresponding to a given fraction of solid (Figure 11). The rheocast structures shown in Figures 24 to 31 clearly show that the resultant microstructure is nondendritic.

The effect of stirring speed on the rheocast macro and microstructure is seen in Figures 24 through 27. In these runs, the stirring speed was kept fixed at 325 rpm (Figure 24), 450 rpm (Figure 26) or 560 rpm (Figure 27). In all these cases, the stirring time and the volume fraction solid present at the isothermal hold time were kept fixed at 15 minutes and 35% volume fraction solid, respectively.

For an ingot of low stirring speed (i.e., 325 rpm), the macrostructure shows a nonuniform distribution of grain size and morphology, Figure 24(a). The coarse grains are accumulated in a "V" shape near the center, while the fine grains are distributed close to the edge and bottom of the ingot. Many intergranular pores are observed in this low stirring speed sample. As the stirring speed increases from 325 rpm to 450 rpm, the uniformity of grain size and morphology increases (cf. Figures 24(a) and 26(a)). Few large grains are present at the center of the ingot, as shown in Figure 26(a). Figure 27(a) shows the macrostructure of the rheocast ingot with a high stirring speed of 560 rpm. It is clear that large grains are not observed in this high stirring speed sample. Therefore, the distribution of particle size and morphology are more uniform in the ingot stirred at 560 rpm than in the ingots stirred at speeds of 325 rpm and 450 rpm (cf. Figures 24(a), 26(a) and 27(a)). Moreover, there is a smaller quantity of intergranular pores in the samples stirred at 450 rpm and 560 rpm than in those stirred at 325 rpm - see Figures 26(a), 27(a) and 24(a). In all the macrostructures shown in Figures 24(a), 26(a) and 27(a), no large shrinkage cavities were observed.

The microstructures corresponding to the three marked locations

A, B and C in Figure 24(a) are shown in Figure 24(b). The grain sizes vary from approximately 1000 μm at location A to 120 μm at location C. In the absence of stirring, the material shows a conventional dendritic structure as shown in Figure 20(b). However, at the low stirring speed of 325 rpm, most of the dendritic structure has been replaced by rosettelike and spherical particles. The three different morphologies of the grain structure can be seen in Figure 25; that is, all three morphologies coexist - spherical, rosettelike and dendritic. It will be seen subsequently that as the stirring speed is increased, the dominant particulate morphology will be spherical. Since section C (see Figure 24(b)) was first to solidify, there are more interparticle cracks in sections A and B (Figure 24(b)), which solidified later.

At the higher rotation speeds of 450 rpm or 560 rpm, one can note that the transition from dendritic to spherical particles is more prevalent (see Figures 26(b) and 27(b)). Dendritic particles are not seen in the samples stirred at 450 and 560 rpm. However, in the sample stirred at the intermediate speed of 450 rpm (Figure 26(b)), both rosettelike and spherical particles can be seen in all three locations of the ingot. In contrast, the sample stirred at 560 rpm exhibits predominantly spherical particles, on the order of 120 μm (see Figure 27(b)). As the stirring speed increases, the observed grain size and interparticle voids decrease; in addition, one notes a more homogeneous distribution of grains.

At constant volume fraction solid (35%) and constant isothermal stirring time (15 minutes), the quantity of $\gamma$-$\gamma'$ eutectic islands and carbide particles along the grain boundaries is not affected by the

stirring speed. However, the homogeneity of the γ-γ' island distribution and their size is affected: at 560 rpm one observes a more homogeneous distribution of γ-γ' eutectic islands and smaller size islands than at 325 rpm.

The effect of stirring speed on the segregation ratio is illustrated by comparing the segregation ratio in the ingot that was obtained at the highest stirring speed of 560 rpm (Table V), to that in the ingot that was obtained at the lowest stirring speed of 325 rpm (Table IV). It has to be mentioned that grain boundaries selected for this study of segregation ratio in any of the rheocast ingots were restricted to boundaries that were solute segregated. Certain segregation-free boundaries observed in rheocast ingots were not included in the study, and they will be described later in this section. At constant stirring time and volume fraction solid, the segregation ratio shows no significant difference as the stirring speed increases. However, the segregation ratio shows less scatter (i.e., lower standard deviation) for both Ti and Cr at a high stirring speed than at a low stirring speed (cf. Tables V to IV). The representative segregation profiles for the lowest and highest stirring speeds are shown in Figure 28.

The effect of isothermal stirring time at a constant volume fraction solid (35%) and a fixed stirring speed (325 rpm) on the resultant rheocast structure can be seen by comparing the structures shown in Figures 24 and 29. The macrostructure shows that as the stirring time is increased from 15 minutes (Figure 24) to 45 minutes (Figure 29), coarse particles and shrinkage cavities disappear. In

addition, with increased stirring time, a more homogeneous particle size distribution is obtained.

The majority of the grains shown in both micrographs of Figure 29(b) are spherical. Figure 29(b) shows representative microstructures from the various locations marked in Figure 29(a). The average grain size is approximately 160 μm, which is larger than the dendrite arm spacing of 120 μm for the nonstirred casting shown earlier in Figure 20(b). A comparison of Figure 24(b) to Figure 29(b) reveals that both the grain size and the quantity of the interparticle voids decrease as the isothermal stirring time increases.

Varying the isothermal stirring time does not affect the amount and size of the γ-γ' eutectic islands and carbide particles. However, the distribution of γ-γ' eutectic islands is more uniform in those samples that were isothermally stirred for a long time, i.e., 45 minutes.

Table VI shows the segregation ratio in the rheocast ingot that was obtained by stirring the slurry at a speed of 325 rpm, volume fraction solid of 35% and stirring time of 45 minutes during solidification. Comparing the segregation ratio between rheocast ingots with stirring time of 15 and 45 minutes, Tables IV and VI, it is shown that increasing the stirring time does not significantly change the segregation ratio of both Ti and Cr; however, the solute content of $C_0$ increases as the stirring time increases. The representative composition profile for the rheocast ingot with an isothermal stirring time of 45 minutes is shown in Figure 28.

The effect on the resultant structure of the isothermal treatment at which the sample was held for a given time ($T_{fs}$ in Figure 11 ) during rheocasting is substantial. Samples were held in the mushy zone at volume fractions solid of 35%, 50% and 65%, and the stirring time and the stirring speed were kept constant at 15 minutes and 325 rpm. Figures 24, 30 and 31 show the macro- and microstructures of rheocast ingots at 35%, 50% and 65% $f_s$, respectively. The macrostructures present in Figures 24(a), 30(a) and 31(a) show regions of large particles surrounded by fine ones. However, the quantity of large particles decreases as the volume fraction solid (during the isothermal hold when rheocasting in the mushy zone) increases. In essence, a more uniform particle size distribution is obtained at high volume fraction solid.

Comparing the microstructures shown in Figures 24(b), 30(b) and 31(b), it can be seen that as the volume fraction solid (present during the isothermal hold period) increases, the rosettelike morphology of the primary phase decreases. In other words, at 65% $f_s$ one observes spherical particles, whereas at 35% $f_s$ one observes a substantial quantity of rosettelike particulates. Furthermore, change in volume fraction solid from 35% $f_s$ to 50% $f_s$ results in a decrease in grain size. However, over the volume fraction solid range, 50% $f_s$ to 65% $f_s$, the change of the grain size is not significant.

Some grains in the ingots that were stirred at both 50% $f_s$ and

65% $f_s$ are observed to be joined together as agglomerates, Figures 30(b) and 31(b). The number of agglomerates in Figure 31(b) is greater than that in Figure 30(b). Figure 32 shows the representative optical micrograph of an agglomerate observed at high magnification. This agglomerate exhibits four grain boundaries, which are designated as #1, #2, #3 and #4. The Ti K-ratio profile across all four boundaries is shown in Figure 33. It is noted that grain boundaries #1, #2, #3 and #4 are all Ti enriched, Figure 33.

The size and quantity of the γ-γ' eutectic islands are influenced by the volume fraction solid present during the isothermal hold time in the mushy zone. A comparison of Figures 24(b), 30(b) and 31(b) shows that the size and quantity of the γ-γ' eutectic islands decreases in the order of 35% fs, 50% $f_s$ and 65% $f_s$. However, no variation is observed for the morphology of the carbide particles as the volume fraction solid changes (cf. Figures 24(b), 30(b) and 31(b)).

The segregation ratio of both Ti and Cr in a rheocast ingot thath was obtained by stirring the liquid metal at a speed of 325 rpm, a stirring time of 15 minutes and a volume fraction solid of 65% is presented in Table VII. Comparing the segregation ratio in a rheocast ingot isothermally stirred at a volume fraction solid of 65% (Table VII) to that of a rheocast ingot while isothermally stirred at a volume fraction solid of 35% (Table IV), it can be noted that at constant stirring speed and time, the segregation ratio decreases as the volume fraction solid increases. In addition, both solute contents of $C_0$ and

$C_{mid}$ increase with the increasing volume fraction solid (cf. Tables IV to VII). Representative composition profiles of both Ti and Cr solute elements are shown in Figure 28 for the rheocast ingot isothermally stirred at a volume fraction solid of 65%.

A representative microstructure of a rheocast ingot that was stirred isothermally at a speed of 450 rpm, at a volume fraction solid of 35% and for 15 minutes duration is shown in Figure 34. Grains within this micrograph were indented by the microhardness tester simply to indicate the areas of interest for SEM and WDS analyses. Figure 35 shows a representative SEM micrograph of secondary precipitated γ' at the centers of the rheocast grains. The morphology of γ', shown in Figure 35, is mainly mixed cuboid and facet dendritic shapes of particle size approximately 0.2 to 0.7 μm.

Fifteen grain boundaries chosen in Figure 34 were examined by WDS analysis to determine whether Ti segregation exists near grain boundaries. However, because of the complexity of precipitated phases present along grain boundaries, the actual level of segregation near grain boundaries was difficult to obtain. Therefore, a distance of approximately 5-10 μm from the grain boundaries or grain boundary phases was used as the point nearest to the boundaries for the WDS analysis on the level of Ti segregation. Grains on both sides of selected grain boundaries were WDS analyzed. The results of these studies are indicated in Figure 34, where boundaries with no Ti enrichment are marked "NE" and boundaries with Ti enrichment are marked "E". One can note that 7 out of the 15 boundaries are not Ti

segregated. It must be emphasized here that these nonsegregated boundaries were not involved in the previous study of the segregation ratio.

SEM micrographs of the secondary precipitated γ' along three different grain boundaries, which were marked as L, M and N in Figure 34, are shown in Figure 36. Grain boundary L, present in Figure 36(a), is not a Ti-enriched boundary, where as both grain boundaries of M and N, shown in Figures 36(b) and 36(c), respectively, are Ti-enriched boundaries. The γ' particles precipitated near the boundary that is not Ti-enriched (Figure 36(a)), exhibit coarser particle size than those precipitated at the center of the grain (Figure 35); however, the observed γ' particle shape in Figure 36(a) is similar to that in Figure 35. When the γ' particles precipitated near the Ti-enriched boundaries where γ-γ' eutectic islands, carbides or grain boundaries γ' exist, the particle shape becomes irregular; in addition, the particles are much coarser than any of the γ' particles precipitated at the center of grain and near the boundary where Ti is not segregated (cf. Figures 36(b), 36(c), 34 and 36(a)). Similar behaviors with respect to the size and morphology of secondary precipitated γ' are observed for all the other rheocast ingots.

The representative nominal composition of the rheocast IN-100 ingot is shown in Table VIII. It is noted that the content of each alloying element within the rheocast ingot is similar to that within the as-received ingot (cf. Tables I and VIII). This is clear evidence that the rheocast ingot is not contaminated by the alumina paddle or crucible.

In summary, the effects of stirring speed, isothermal stirring time and volume fraction solid on the resultant macro- and microstructural features are listed in Tables IX, X and XI, respectively.

A-3 Vacuum Arc Double Electrode Remelting (VADER)

Figure 37 is a representative macrostructure of a 6" diameter VADER IN-100 ingot. The macrostructure is characterized by a uniform distribution of fine and equiaxed grains. Neither center cavities nor intergranular cracks are present in the VADER ingot.

The microstructure of VADER samples lacks identifiable spines and can be categorized as consisting of a group of equiaxed nondendritic grains, Figure 38. A grain size of approximately 100 μm in VADER structures is less than the dendritic arm spacing found in the nonstirred structures, which were shown in Figure 18.

The size and distribution of the phases that are present in the VADER IN-100 ingot are also shown in Figure 38. The $\gamma$-$\gamma'$ eutectic islands are uniformly distributed and vary in size and shape. Most of carbide particles found in the VADER structure are scriptlike and only a few were found to be blocky. The SEM micrographs of secondary precipitated $\gamma'$, which are surrounded by a $\gamma$ matrix at the center and adjacent to the boundary of a VADER grain, are illustrated in Figures 39(a) and 39(b), respectively. Secondary $\gamma'$ particles at the center of the grain contain both cuboid and dendritic shapes, with sizes ranging

from less than 0.2 μm to 0.7 μm, Figure 39(a). In contrast, the secondary γ' particles become large and irregular in shape at locations adjacent to the grain boundary, Figure 39(b).

The representative solute profiles and segregation ratios in the VADER ingot are shown in Figure 40 and Table XII, respectively. The trend of solute profiles and segregation ratios in the VADER ingot is similar to those in the nonstirred ingot (cf. Figure 40 and Table XII to Figure 22 and Table III). A typical SEM micrograph of the grain boundary phases, including γ-γ' eutectic islands, MC carbides, and voids, which are surrounded by the secondary precipitated γ' in a matrix of γ, is illustrated in Figure 41(a). This combination of phases is frequently observed in all the nonstirred, rheocast and VADER microstructures. Figure 41(b) shows a typical γ-γ' network in the γ-γ' eutectic island.

## B. Structural Response to Post Solidification Thermal Treatments

### B-1 Hot Isostatic Pressing (HIP)

The representative optical micrographs of hot isostatically pressed rheocast and VADER microstructures are shown in Figures 42 to 44. The structure shown in Figure 42 was obtained by HIP an ingot that was solidified during stirring of the liquid metal at a speed of 325 rpm, at a volume fraction solid of 35% and for a 15-minute duration. The HIP structures present in both Figures 43(a) and 43(b) were obtained from an ingot that was stirred at the same volume fraction solid, for the same stirring time as that in Figure 42, but with a high stirring speed of 560 rpm. The number of grains does not significantly

change after HIP (compare Figure 42 and 24(b); 43(a) with 27(b)). Further, the size and quantity of the γ-γ' eutectic islands are smaller; that is, HIP results in an ingot that is more homogeneous than as-cast ingots. The quantity of intergranular voids is reduced by HIP (compare Figures 42 and 24(b); 43 with 27(b)); however, a few voids are observed in HIP ingots as shown in Figure 43(b). Similar observations are noted for all the rheocast and non-stirred ingots before and after HIP.

Figure 44 shows the representative microstructures of the VADER ingot after HIP. The grain size range observed varied between 200 μm and 2000 μm, which is much coarser than the grain size observed prior to HIP, Figure 38. The γ-γ' eutectic islands are barely observed in this HIP VADER structure.

B-2 Heat Treatment

The heat treatment cycle for IN-100 superalloy includes a solution treatment followed by a three-stage aging treatment. Before heat treating, all the ingots are subjected to HIP using the same thermal cycle. The micrographs of the nonstirred, rheocast and VADER ingots after HIP and heat treatment are shown in Figures 45, 46-49 and 50, respectively.

The grains in the nonstirred material after HIP and heat treatment exhibit a size range similar to that observed before HIP (cf. Figures 45 and 20(b)). The size and amount of the γ-γ' eutectic islands decrease after postsolidification thermal treatment.

Figure 46 represents the heat treated microstructure of the rheocast sample that was stirred for 15 minutes at a speed of 325 rpm

and at a volume fraction solid of 35%; Figure 47 corresponds to the highest stirring speed of 560 rpm and the same volume fraction solid and stirring time as in Figure 46; Figure 48 corresponds to the highest isothermal stirring time of 45 minutes and the same speed and volume fraction solid as in Figure 46; and Figure 49 corresponds to the highest volume fraction solid of 65% and the same stirring speed and time as in Figure 46. The grains have coarsened and have become spherical in shape after thermal treatment (compare Figures 46 and 24(b); 47 and 27(b); 48 and 29(b); 49 and 31(b)). Each of the three microstructures shown in Figures 47, 48 and 49 exhibits a smaller grain size and a more uniform distribution of $\gamma$-$\gamma'$ eutectic islands than the microstructure shown in Figure 46. However, the structure of the sample that had been rheocast at the highest stirring speed (shown in Figure 47) has the finest grain size.

The microstructure of the VADER ingot after heat treatment is shown in Figure 50, where large but fairly homogeneous grains can be seen. A comparison of the grain size of the heat treated microstructures shown in Figures 45 to 50 reveals that the rheocast material contains the smallest grain size; however, the VADER material has the most homogeneous structure. The size of the $\gamma$-$\gamma'$ eutectic islands in the heat treated, nonstirred material is not significantly different from those in the heat treated, rheocast material (cf. Figures 45 and 46-49). A representative SEM micrograph of the secondary precipitated $\gamma'$ particles at the grain center after HIP and heat treatment is shown in Figure 51. These $\gamma'$ particles exhibit cuboidal shape with particle size varying from <0.1 μm to 0.5 μm.

These γ' particles have a nondendritic morphology (see Figure 51). Similar morphology of the secondary precipitated γ' particles are seen at the center of the grains for all the heat treated nonstirred, rheocast and VADER ingots. A comparison of the γ' particles' morphology at the center of the heat-treated grains (shown in Figure 51) with those particles of the as-cast grains (shown in Figures 22(a), 35 and 39) reveals that the particle size decreases slightly and the particle shape becomes regular after heat treatment. Figure 52(a) shows a representative SEM micrograph of the secondary precipitated γ' particles adjacent to a γ-γ' eutectic island as well as carbide particles along the boundaries of the heat treated grains. The size of the γ' particles increases and the particle size becomes irregular when the γ' particles precipitate near the boundary rather than at the center of the grain (cf. Figures 51 and 52(a)). A denuded zone, i.e., a precipitate-free zone, surrounding the grain boundary γ-γ' eutectic islands is clearly observed in Figure 52(a). Similar observations for the morphology of the grain boundary phases are observed in all the non-stirred and rheocast ingots. For the heat treated VADER material, the γ-γ' eutectic islands disappear, and are replaced by coarse γ' particles, which are distributed along the grain boundary, Figure 52(b). These coarse γ' particles also are surrounded by a precipitate-free zone, i.e., a denuded zone.

The nominal compositions of the heat treated IN-100 samples that were processed by rheocasting and VADER are listed in Table XIII. A comparison of these compositions for the heat treated conditions (Table XIII) to those of as-cast conditions (Table VIII) confirms that

the amount of the alloying element did not change after HIP and heat treatment.

C. Mechanical Properties

C-1 Microhardness

Hardness at the centers and near the boundaries of the grains or dendrite arms was evaluated in both the as-cast and heat treated materials. The results are summarized in Tables XIV and XV. Ranges of hardness, evaluated from 25 arbitrarily selected grains, at either grain centers or near grain boundaries, are given for each condition.

In each grain or dendrite arm, without exception, the center exhibits a lower hardness than the areas adjacent to the grain boundary. For the as-cast condition, the mean hardness at the center or near the boundary of the VADER grain is similar to that of the dendrite arm in the nonstirred cases. Table XIV also shows the effect of the stirring speed, volume fraction solid and stirring time on the mean hardness value at the grain center or adjacent to the grain boundaries. No significant difference in the mean hardness is observed for either a changing stirring speed or isothermal stirring time. However, the mean hardness increases at the grain center as the volume fraction solid during stirring increases (Table XIV).

For the heat-treated condition, the mean hardness at the grain center and adjacent to the grain boundary is similar for nonstirred and rheocast materials (Table XV). In contrast, the VADER casting shows higher mean hardness values at the grain center and lower mean hardness values near the grain boundary in comparison to all of the

nonstirred and rheocast cases (Table XIV).

C-2 Tensile Properties

Heat treated specimens which were obtained from nonstirred, rheocast and VADER ingots were tensile tested at 650°C (1200°F) in air. The values for each tensile property-i.e., yield strength, ultimate tensile strength and ductility-were calculated as the average of 2 specimens from each of the ingots. These resultant average tensile properties are listed in Table XVI. Because the rheocast structure is reproducible from batch to batch under the same processing conditions (i.e., same stirring speed, same volume fraction solid and same stirring time), the corresponding tensile properties are believed to be consistent with the rheocast structure. For purposes of comparison, tensile properties from commercially cast samples were included in the evaluation. The effects of stirring speed, isothermal stirring time and the volume fraction solid on the tensile properties of rheocast materials are shown in Figures 53, 54 and 55, respectively, while the comparison of the tensile properties between various processing techniques is shown in Figure 56. At constant stirring time and volume fraction solid, the yield strength and ultimate tensile strength increases as the stirring speed increases, Figure 53. However, the amount by which the strength increases is more pronounced as the stirring speed increases from 325 rpm to 450 rpm than when it is increased from 450 rpm to 560 rpm. The ductility does not change for the various stirring speeds used during rheocasting. In Figure 54, it is seen that the ingot with a long stirring time exhibits a higher yield

strength and ultimate tensile strength than the ingot with a short stirring time for identical stirring speed and volume fraction solid values. No variation in ductility values is observed as a result of varying the isothermal stirring time during rheocasting.

At constant stirring speed and stirring time, the yield strength and ultimate tensile strength increases significantly as the volume fraction solid increases from 35% to 50%; however, the level of strength does not vary as volume fraction solid increases from 50% to 65% (Figure 55). Furthermore, the ductility remains constant as the volume fraction solid present during rheocasting changes.

The tensile properties as a function of processing technique are shown in Figure 56. Both the highest and lowest levels of tensile properties, selected from all the data for the rheocast materials, are used here for comparison. The commercially cast, nonstirred and VADER specimens have a similar level of yield strength; however, these levels of yield strength are lower than the yield strength of the rheocast specimens seen in Figure 56. The ultimate tensile strength of the commercially cast specimen is slightly higher than that of both the rheocast and VADER specimens. The nonstirred specimen exhibits a much lower ultimate tensile strength than the specimens made from any of the other processing methods. In Figure 56, it is clear that the commercially cast specimen shows the highest ductility, followed by the VADER, rheocast, and nonstirred samples.

## C-3 Fatigue Crack Propagation (FCP) Rate

### C-3-1 da/dn versus ΔK

FCP rates (da/dn) were determined at 650°C (1200°F) in air as a function of the stress intensity range (ΔK) for each of the processing methods evaluated. A P/M processed IN-100 specimen was also evaluated for purposes of comparison. The da/dn versus ΔK data are summarized in Figures 57 to 61. Excellent reproducibility was obtained, as shown in Figures 57, 58 and 59.

Figure 60 shows the comparison of crack propagation rates between the specimens obtained from the heat treated rheocast ingot with the highest stirring speed and the specimens obtained from the heat treated rheocast ingot with the highest volume fraction solid. No variation in FCP rates between these two rheocasting cases are observed.

The effect of the processing mode-i.e., P/M, rheocasting and VADER on the FCP rate is shown in Figure 61. It is noted that at $\Delta K < 50$ ksi $\sqrt{\text{inches}}$ the FCP rate is greater for the P/M material than for the rheocast and VADER materials, Figure 61. The resistance to crack propagation in rheocast material is similar to that in the VADER material evaluated.

### C-3-2 Fracture Morphology

The macroscopic fracture appearance of the CT specimens is shown in Figure 62 for the P/M, rheocast and VADER materials. The rheocast sample used here was obtained from the ingot that was stirred at the highest volume fraction solid. For each processing mode,

the fatigue crack propagates normal to the stress axis. At low magnification, the fracture surface morphology of all specimens can be divided into three regions, which correspond to room temperature precracking, stable crack growth at 650°C (1200°F) and final fast fracture. The three regions are clearly seen in Figure 63 for each of the specimens. The fracture surface is flatter in the P/M material than in the VADER and rheocast materials.

The optical and SEM micrographs of the stable crack growth for the P/M, VADER and rheocast materials are shown in Figures 64 through 69. The P/M specimen, for which the grain size is approximately 5 μm, exhibits an intergranular fracture mode. In contrast, the rheocast and VADER specimens which possessed coarse grain sizes, show a mixed mode and a transgranular fracture mode, respectively, as seen in Figures 66, 67, 68 and 69. Figure 70 shows the optical micrograph of the fracture in the fine grains of the rheocast sample. The crack has clearly propagated through areas near the grain boundary but not through the denuded zone. A similar fracture morphology for the rheocast material is observed in the specimens that were obtained from material processed using the highest stirring speed.

# V. DISCUSSION

## A. Processing of Rheocast and VADER IN-100 Alloy

### A-1 Nonstirred Casting

The IN-100 charge was simply induction melted to a temperature of maximum 30°C (86°F) superheat and subsequently furnace cooled in the same alumina crucible under vacuum. There was no agitation within the mushy zone during solidification. However, the superheat was not kept uniform throughout the bulk of the liquid melt; for example, heat loss from the bottom of the apparatus would give rise to a lower superheat of the liquid metal near the bottom than at the center, Figure 9. During cooling when the power of the unit was turned off, the solid particles started to nucleate from the top and bottom surfaces of the melt, due to radiative heat loss and conduction through the crucible, respectively. Solid particles formed early during solidification have a lower solute content and a higher density than the surrounding liquid; therefore, they will tend to sink due to gravity. The number of solid particles at the bottom of the liquid melt then increases, resulting in a fine equiaxed dendritic structure. In contrast, only a few solid particles surviving at the top section of the melt take part in the formation of the columnar structure where the grain growth direction is parallel to the heat transfer direction. Regions between the top section of the columnar structure and the bottom section of the fine equiaxed structure exhibit a coarse equiaxed dendritic structure,

Figure 20(a).

The IN-100 nickel-base superalloy has a high amount of multiple solute content (totally ≈ 44 wt%) and thus has a wide freezing range. The dendrites that form during the early stages of solidification in the bottom portion of the casting are freely floating, and both liquid and solid can flow to compensate for solidification shrinkage. In other words, mass feeding is taking place (60). As solidificaton proceeds, the dendrites are no longer free to move and tend to form a rigid network. It is difficult for the surrounding liquid to feed the solidification shrinkage, and thus micropores result in the region of the equiaxed dendrites. The level of macro- and microporosity is obviously higher in the locations near the center of the ingot or the last-to-freeze region.

Due to nonequilibrium solidification, the resultant nonstirred structure exhibits microsegregation, Figure 23 and Table III. Solutes such as Cr and Ti lower the melting point of the alloy and therefore segregate to the interdendrite regions. However, the semiquantitative measurement of the degree of segregation is difficult to obtain in the cast structure of IN-100. For example, the composition ratio (see Table III) for Ti varies widely, from 1.10 to 1.42; this variation was carried out at 20 arbitrarily chosen dendrite arms of the nonstirred castings. This variation of the composition ratio is attributed to the variation in the sectioning plane. In order to accurately determine the segregation ratio between primaries, the sectioning must be done normal to the growth direction; to observe segregation between secondaries, a plane parallel to the growth direction must be examined (36). For the

equiaxed dendritic structure, the growing orientations of dendritic grains are random in all three dimensions. Therefore, it is difficult to judge from a two-dimensional structure whether the chosen dendrite arm is observed in the proper plane.

Segregation at grain boundaries also produces many sites for complex precipitation phenomena; this segregation depends on the solid-liquid interface morphology and on the macrostructure (whether columnar or equiaxed) (36). Since grooves where the grain boundaries intersect as solid-liquid interface are deeper than interdendritic grooves, more lateral solute flow takes place at these areas, leading to segregates even more complex than found interdendritically. The size of the $\gamma$-$\gamma'$ eutectic islands is therefore much larger in the grain boundaries than in the interdendritic regions (cf. Figure 21(a) and 21(b)).

A-2 Rheocasting

Previous work on structure characterization of rheocasting structures has been on structures that were obtained by stirring in the mushy zone and subsequently water quenching the casting. None of the rheocast structures that have been examined were furnace cooled subsequent to stirring. Laxmanan (57) has successfully rheocast both Udimet-700 and IN-100 alloys in an argon atmosphere. Subsequently, Oblak et al. (105) characterized the thermal processing response of rheocast alloys. However, the sample examined was that of Laxmanan, and unfortunately, Laxmanan did not process the melt in a vacuum, which contaminated the product.

The introduction of mechanical stirring during solidification changes the dendritic morphology, as observed in the nonstirred structure (Figure 20), to a rosettelike or spherical morphology. This gives rise to improved grain refinement, soundness and homogeneity of the final cast structure. However, the degree of structural improvement varies with stirring speed, isothermal stirring time and the volume fraction solid present during rheocasting. Increasing the stirring speed, isothermal stirring time or volume fraction solid increases grain sphericity and reduces grain size, porosity and segregation - see Tables IX, X and XI.

The primary solid particles that existed in the bulk when the alloy was partially solid coarsened and changed morphology during the subsequent solidification stage in the furnace. Therefore, in order to delineate the size and morphology of these primary solid particles, samples sectioned from the rheocast ingot were reheated to the temperature corresponding to the fraction of solid at which the ingot was stirred, were held for 5 minutes and then were immediately water quenched. In this manner, the imposed high solidification rate clearly distinguishes between the primary solid phase and the liquid phase, which now possesses a finer dendrite arm spacing. The resultant microstructure is termed a "duplex structure" (57).

A-2-1 Observation of Primary Solid Particles

Duplex structures of reheated specimens from nonstirred and rheocast ingots are shown in Figures 71-76. It can be noted that the

primary solid particles contain small pockets of entrapped liquid, which appear as black dots. Laxmanan (57) suggests that these pockets may be formed by spheroidization of interparticle veins, which are actually regions of entrapped liquid, during the reheating cycle. However, there is no experimental evidence supporting the hypothesis.

Figure 71 illustrates the duplex structure of the reheated nonstirred sample. In the absence of stirring, the observed primary solid particles are typical of those found in conventional dendritic structures. However, the dendritic particles shown in Figure 71 may exhibit different morphologies than the actual primary solid particles that were obtained during solidification of the nonstirred castings. This difference is due to the substantial coarsening and homogenization that takes place during processing - i.e., during

(i) slow furnace cooling of the nonstirred casting (56)

(ii) reheating of the sample from room temperature to a specific temperature in the mushy zone (30)

(iii) isothermal holding at a specific temperature in the mushy zone

Figure 72 shows the duplex structure of a reheated nonstirred IN-100 sample that was held in the furnace for 20 minutes instead of 5 minutes. The size and spheroidicity of the primary solid particles increases as the isothermal holding time increases (cf. 71 and 72). There is clear evidence of coarsening during condition (iii) described above. Therefore, it is suggested that in order to characterize the morphology of primary solid particles, the isothermal holding time should be as short as possible; however, a minimum holding time has to

be maintained to ensure melting of the liquid phase surrounding the dendrites or the solid particles.

The effect of stirring speed at constant stirring time (15 minutes) and constant volume fraction solid (35%) on the primary solid particles is seen in Figures 73 (325 rpm) and 74 (560 rpm). In Figure 73, the primary solid particles exhibit combinations of dendritic, rosettelike and spherical morphologies; while in Figure 74 only spherical-shape primary solid particles are observed. Therefore, it is quite clear that the higher the stirring speed, the finer and more spherical the primary solid particles (cf. Figures 73 and 74).

Vogel et al. (65) observed in-situ quenched structures after stirring and have shown that in Al-20% Cu alloy, the small primary solid particles seen as a result of high stirring speeds are fully suspended in the liquid. However, this is not observed in the reheated rheocast structure of Figure 74, where the fine and spherical primary solid particles are shown not to be uniformly distributed, and only very few of them are isolated. This is because the primary solid particles have been "rearranged" during the reheating experiments. Isothermal holding of a reheated rheocast sample at the temperature corresponding to that of 65% volume fraction liquid results in sample shape changes caused by liquid flow and subsequent formation of clusters due to the primary solid particle movement. However, the tendency of the primary solid particles to rearrange will be less pronounced when the volume fraction solid increases.

In summary, the reheating technique is an excellent tool for delineating between the solid primary particles and the surrounding

liquid phase subsequent to processing and solidification. It is, however, more qualitative tool than an accurate quantitative technique for estimating volume fractions, because of the coarsening and homogenization of the solid particles during the reheating and isothermal holding cycle.

Figures 73 and 75 show the effect of isothermal stirring times of 15 minutes and 45 minutes on the morphology of the primary solid particles at constant stirring rate (325 rpm) and volume fraction solid (35%). It can be noted that the sphericity and number of the primary solid particles increases as the stirring time increases. However, when the reheated structure resulting from a prolonged stirring action (Figure 75) is compared with that resulting from a high stirring speed at a constant volume fraction solid (Figure 74), it is clear that the former exhibits coarser primary solid particles than the latter. The evidence indicates that coarsening will be accelerated more by a prolonged stirring action than by a high stirring speed.

The effect of volume fraction solid at constant stirring speed and constant isothermal stirring time on the morphology of the primary solid particles is illustrated in Figures 73 (35% fs) and 76 (65% fs). The primary solid particles at high volume fraction solid tend to sinter together and form agglomerates. As mentioned previously, this agglomeration of rounded or spherical primary solid particles at a high volume fraction solid of 65% is unlikely to take place simply through the movement of particles during reheating experiment. Moreover, lots of partially wetted particle boundaries are observed in each agglomerate in Figure 76, while the particle boundaries shown in

Figures 73 and 74 are completely wetted. It is clear, then, that some of the agglomerates observed in Figure 76 have resulted from the influence of stirring at a high volume fraction solid. It is also noted that increasing the volume fraction solid increases the number of primary solid particles at a given constant stirring speed and stirring time. However, the size of the primary solid particles at high volume fraction solid is larger than that of the dendrite arm spacing (or isolated spherical particles) at a low volume fraction solid (cf. Figures 71 and 76). Therefore, it is clear that coarsening and dendrite fragmentation increases as the volume fraction solid increase while the slurry is isothermally held and stirred in the mushy zone.

### A-2-2 Mechanism of Particle Morphology Change by Stirring During Solidification

From the observation of various reheated structures, it is clear that the conventional dendritic morphology of the primary solid particles is transformed to one consisting of rosettelike or spherical particles by the introduction of mechanical stirring during solidification. The mechanism of this dendrite-nondendrite transformation has been reviewed by Doherty et al. (63), and the details have been summarized and discussed in Section D-3 of Chapter II. It has been concluded that the change from a dendritic to the rounded globular morphology is due to dendrite bending, fragmentation and subsequent coarsening during the vigorous stirring and isothermal holding of the slurry. Two alternative mechanisms, grain boundary recrystallization, i.e., Vogel-Doherty-Cantor's model, and grain

boundary sliding, explain the phenomenon of dendrite fragmentation which occurs during rheocasting.

In the reheating experiments, segregation-free low-angle boundaries could not be observed. It has been mentioned in Section 4-2-i of this chapter that the primary solid particles coarsen and homogenize during the reheating and subsequent isothermal holding cycle in the mushy zone, which causes the nonsegregated low-angle boundaries to migrate or disappear, making the observation of such low-energy boundaries extremely difficult. The best way to determine the presence of low-angle boundaries inside or between primary solid particles is by in-situ water quenching of the liquid metal while stirring and isothermally holding in the mushy zone. This in-situ quenching process is complicated to set up and operate inside the high-vacuum induction furnace and was not pursued in this study.

Lee (52) has shown that low-angle (low-energy) grain boundaries were observed inside the rheocast grains of the in-situ water-quenched rheocast structures of Al-15 w/o Cu alloy obtained after continuously stirring the liquid metal from above liquidus temperature to the desired temperature in the mushy zone and then isothermally stirring for 3 hours. However, the primary particles will coarsen and homogenize during an isothermal 3-hour hold. No explanation has been given by Lee (52) as to how these "recrystallization" low-angle boundaries respond to the grain coarsening effect.

Grain coarsening and grain growth occur simultaneously, and the process is accompanied by a decrease in the surface free energy. This decrease in free energy comes from the decrease in the total grain

boundary area. The migration velocity v of a grain boundary during grain growth in pure metal can be expresed as

$$v = M \Delta \mu \quad (2)$$

and

$$M = bv/KT \exp(-Q_G/KT) \quad (3)$$

$$\Delta\mu = -2\gamma_b \Omega/r \text{ (Gibbs-Thomson's equation for a spherical grain)} \quad (4)$$

where M: mobility of the boundary

$\Delta\mu$: chemical potential drop across a grain boundary

b: distance that boundary migrates when each net atom is transferred from one grain to the neighboring grain

v: vibrational frequency of atoms

K: Boltzmann's constant

T: absolute temperature

$Q_G$: activated energy for grain boundary

$\gamma_b$: grain boundary energy

$\Omega$: atomic volume

r: radius of the spherical grain

According to the above equations, Eqs. 2-4, the migration velocity of the grain boundary is influenced by the activation energy $Q_G$ and grain boundary energy, $\gamma_b$, at a fixed temperature and grain radius. Viswanathan and Bauer (106) have examined the grain boundary

migration in high-purity copper bicrystals and have shown that the activated energy for grain boundary migration, $Q_G$, decreases as the grain boundary misorientation angle increases. This confirms that low-angle boundaries are less mobile than the randomly distributed high-angle boundaries. In addition, it has been shown by Viswanathan et al. (106) that the activation energy for grain boundary migration did not vary much at these low-angle boundaries (misorientation angles were less than 9°). Moreover, the grain boundary energy $\gamma_b$ increases as the grain boundary misorientation angle increases (106). As a consequence, it can be concluded that the lower the grain boundary misorientation angle is, the slower the grain boundary migration rate is. It should be noted that the drag effect caused by impurity or solute atoms has been ignored in this analysis.

More than 75% ~ 80% of the grain boundaries observed by Lee (52) in the rheocast microstructures that were quenched from the mushy zone without isothermal holding are nonsegregated low-angle boundaries. Accordingly, these low-angle boundaries have a low mobility of migration and grain boundary energy and thus have low migration velocities during grain growth. Consequently, after 3 hours of isothermal stirring, grain boundaries with a low misorientation angle will survive and will exist because of their low velocity of migration. The remaining 20% ~ 25% of the grain boundaries observed by Lee (52) in the rheocast microstructures that were quenched from the mushy zone without isothermal stirring are solute-enriched

high-angle boundaries, and many of them are of low energy as a result of sintering effects. Primary solid particles may continuously undergo sintering (to form clusters) and fragmentation of clusters by deformation, or grain boundary sliding during a 3-hour isothermal stirring cycle. Therefore, the response of these high-angle but low-energy boundaries to grain growth (during isothermal stirring) is more complicated than the relationship given by equation 2 for the grain boundary migration.

In this study, the IN-100 liquid metal was mechanically and continuously stirred from 30°C (86°F) above the liquidus temperature to a desired temperature in the mushy zone and then isothermally stirred for an additional 15 or 45 minutes and subsequently furnace cooled without stirring. The history of grain boundary migration in the rheocast structure after furnace cooling is more complicated than that after in-situ quenching because grain growth in the former is occuring not only during isothermal stirring but also during the furnace cooling period. The grain boundaries that survived after isothermal stirring in the mushy zone will again move, or disappear, during the subsequent furnace cooling period. However, the migration velocity of high- or low-angle grain boundaries is much slower during furnace cooling than during isothermal stirring. This slower grain boundary movement during furnace cooling can be attributed to lower temperatures; the drag exerted by grain boundary precipitates, i.e., carbides, $\gamma$-$\gamma'$ eutectic islands and incoherent $\gamma'$ particles; and the drag exerted by coherent $\gamma'$ particles inside grains. Therefore, most of the low-energy

boundaries that have survived after isothermal stirring in the mushy zone will be retained after the furnace cooling of the sample.

All rheocast furnace-cooled ingots that were processed under different processing conditions - different stirring speed, time, $f_s$ - have a microstructure that shows a certain amount of nonsegregated grain boundaries that were not observed in the dendritic grains of the nonstirred structures. For example, a representative SEM micrograph of a rheocast structure, Figure 34, shows that 7 out of the 15 grain boundaries examined by WDS analysis are not Ti- and Cr-enriched. However, these 7 nonsegregated grain boundaries cannot categorically be characterized as low-angle boundaries since twin boundaries, which are high-angle boundaries, are also known not to be solute-enriched boundaries. Therefore, it is necessary to carry out grain misorientation studies to quantitatively evaluate the misorientation angles between grains and establish without doubt the nature of the boundary; i.e. low-angle boundaries or twin high angle-boundaries. Unfortunately, the Kossel camera was not available during this study to measure the misorientation angles of the grain boundary. Even though a quantitative analysis regarding the origin of grain boundaries was not carried out, the existence of nonsegregated grain boundaries in all the rheocast ingots, and their absence in the nonstirred ingots, is indirect evidence of the Vogel-Doherty-Cantor model, which suggests that the breakup of dendrites during rheocasting is preceded by the formation of grain boundaries.

A-2-3 Rheocast Microstructure

The introduction of mechanical stirring during solidification results in a change in the structure of the ingot. A combination of columnar and varied-size equiaxed dendritic grains is observed in the nonstirred ingots; these are replaced by rounded or globular nondendritic grains in the rheocast ingots. In some of the rheocast ingots, small regions of coarse equiaxed grains are observed. The degree of structural change noted during rheocasting is a consequence of the processing variables imposed - i.e., the degree of stirring speed, isothermal stirring time and volume fraction solid. The influence of the processing variables on the resultant rheocast structures can be explained in terms of the change in morphology of the primary solid particles, described earlier in Section A-2-1, and the mechanism of the transition from dendritic to nondendritic, Section A-2-2.

(a) Effect of Stirring Speed

When the IN-100 melt is continuously stirred by a rectangular paddle from 30°C (86°F) above the liquidus temperature, the bulk bath temperature is uniform everywhere inside the crucible except for a thin laminar region near the crucible wall because of the induced convective flow or mixing by vigorous agitation. The observed temperature gradients for the case of the nonstirred castings (Figure 9) is not observed in the stirred rheocastings.

When the melt temperature is lowered slightly below the liquidus, the primary solid particles begin to nucleate, and subsequently growth occurs. These nuclei, which are not uniformly distributed in the

nonstirred case, due to gravity segregation, are fully and uniformly suspended in the melt when mechanically stirred: the gravity effect resulting from density differences between the solid and liquid phases is overcome by the induced turbulent fluid flow.

The primary dendrite particles formed during the early stages of solidification exhibit a low solute content. These high-purity particles are believed to be easily bent and are plastically deformable under shear at a temperature near their melting point (64). With mechanical stirring, the dendrite arms of the primary solid particles in the IN-100 alloy system are expected to be bent by the stirring-induced shear stresses and thus to form grain boundaries. As a consequence, nondendritic particles will be formed since the dendrites will break apart along the prior boundaries. During the early stages of solidification, these solid particles, which resulted from either nucleation or fragmentation, are spaced widely apart since there is a low volume fraction solid, and they are expected to grow as small dendrites, because the growing solid-liquid interface is predicted to become more unstable by the stirring action. The formation of the more unstable solid-liquid interface occurred because the thickness of the solute-enriched layer is reduced from a value close to the particle radius to that of the boundary layer thickness, and the solute gradient becomes steeper with stirring. Therefore, the solid particles produced during stirring can be attributed to continuous formation and fragmentation of dendrites until the density of the fine solid particles is high enough that a stable nondendritic growth may be expected when the

overlapping diffusion fields from adjacent growing particles interact to reduce concentration gradients and thus cause shape instability (28). These solid particles will then spheroidize mostly during isothermal holding in the mushy zone.

The effect of stirring speed on the resultant rheocast structure is shown in Figures 24 to 27, where structures are compared at a constant volume fraction solid of 35% and an isothermal stirring time of 15 minutes. Increasing the stirring speed, i.e., shear rate, in the liquid metal increases the turbulent fluid flow and therefore results in an increase in the induced shear stress on the dendrite particles. Accordingly, the quantity of solid particles detached from the dendrites by fragmentation can be expected to increase as the speed of mechanical stirring increases. Therefore, with a high stirring speed of 560 rpm, most of the primary solid particles present after isothermal holding are spherical in shape (Figure 74) while with a low stirring speed of 325 rpm, the primary solid particles show a combination of dendritic, rosettelike and spherical morphologies (Figure 73).

The macrosegregation of the resultant rheocast structure has been reduced or eliminated by increasing the stirring speed in the mushy zone (compare Figures 24(a) and 27(a)). This effect of stirring speed on the macroscale chemical homogeneity can be attributed to the degree of mass feeding, i.e., movement of solid and liquid, when the paddle was removed from the melt. It has been mentioned in Section B-1 of Chapter III that for all the ingots stirred at a volume fraction solid of 35%, the stirring was discontinued after isothermal holding,

and subsequently the rectangular paddle was lifted out and the slurry was allowed to cool. The primary solid particles suspended fully in the liquid metal during stirring tend to cluster together when the stirring is terminated. The strength (or number) of bonds between particles increases with time and so does the viscosity of the slurry. Moreover, it has been shown that the clustering reaction is faster in a slurry with a large amount of solid-liquid interfacial area, e.g., dendritic or rosettelike solid particles, than in a slurry having a smaller solid-liquid interfacial area, e.g. spherical solid particles (63). Consequently, at the same volume fraction solid, the movement of liquid and solid, i.e., mass feeding of the mushy network, will be higher for the case when spherical solid particles exist than the case when a dendritic/rosette like structure exists. Therefore, for a liquid metal stirred at a high speed of 560 rpm, the resultant primary solid particles are mostly spherical, as seen in Figure 74. These particles can easily rearrange their positioning, i.e., mass feeding occurs. During the furnace cooling period, these primary solid particles are continuously growing without any further interfacial instability until they contact and impinge with each other. As a consequence, the resultant rheocast structure of the ingot that was stirred at a high speed of 560 rpm clearly shows a uniform distribution of fine nonequiaxed grains (Figure 27).

In contrast, as the stirring speed decreases from 560 rpm to 325 rpm, the number of rosettelike solid particles increases; this gives rise to an increase in the bonds between particles, and thus

the viscosity is increased. Accordingly, when the paddle is lifted without stirring, the mass feeding of the mushy alloy in the low stirring speed case will be difficult or insufficient, and as a consequence, this will result in a V-shaped region where only a few primary solid particles or nuclei exist. The formation of this V-shaped macrosegregation region is due to the fluid flow pattern induced by lifting paddle, shown in Figure 77. After the slurry is furnace cooled, coarse dendritic grains are expected to be formed in this V-shaped region, since only a few nuclei are present and it is the area that solidified last, Figure 24(a). This phenomenon of macrosegregation is further confirmed by the results obtained from WDS analyses, which is resulted that Ti and Cr contents in the V-shaped region are higher than those in any other locations in the ingot (Figure 78).

Increasing the stirring speed in the mushy zone does not significantly change the level of microsegregation (cf. Tables IV and V). This similarity in the level of microsegregation is because the total solidification time, including the isothermal holding in the mushy zone, does not vary with stirring speed. This is confirmed by the measured Ti and Cr contents for the 20 arbitrarily selected grain samples that were stirred at high and low stirring speeds; see Tables IV and V. It is believed that the scatter in the measured compositions is due to variations in the plane of section from one grain to the other.

Murty et al. (56) have shown that a flat elemental composition profile with abrupt changes at boundaries was evident in the primary solid particles of the water-quenched slurries in the X-40 cobalt base superalloy. However, such a flat segregation profile is not observed in

any of the representative rheocast IN-100 composition profiles shown in Figure 28, where the solute content (such as Ti and Cr) increases gradually from the grain center to the grain boundary. The nature of the composition profile in the rheocast IN-100 alloy can be attributed to the difference in the total solidification time. The rheocast ingots of IN-100, which were solidified slowly in the furnace will experience more solute diffusion than the rheocast sample of X-40, which was simply water quenched from the mushy zone. During furnace cooling, after the stirring action has been stopped, the rate of solute diffusion will decrease as the temperature drops. In addition, the amount of solute diffused can be expected to decrease as the distance from the grain boundary to the grain center increases. Consequently, a gradient of solute content will be expected in the rheocast grain after the ingot has been furnace cooled.

At constant isothermal stirring time and volume fraction solid, the quantity of $\gamma$-$\gamma'$ eutectic islands present in the resultant rheocast structure is not expected to change as the stirring speed varies. However, changing the stirring speed while in the mushy zone has been shown to affect the size and morphology of the grains in the rheocast ingot and therefore could give rise to a change in the size and distribution of the $\gamma$-$\gamma'$ eutectic islands. For the ingot stirred at a low speed of 325 rpm during solidification, a significant quantity of the existing rosettelike or dendritic grains exhibit fine $\gamma$-$\gamma'$ eutectic particles between the bent dendrites and coarse $\gamma$-$\gamma'$ particles between grains (Figure 24(b)). The $\gamma$-$\gamma'$ particles are non-uniformly distributed. In contrast, as the stirring speed increases, the quantity of the

rosettelike grains decreases in favor of spherical grains; thus the number of grain boundaries increases. As a consequence, the γ-γ' eutectic islands can be expected to precipitate uniformly between the grains during the final stages of solidification. For example, the γ-γ' eutectic islands are more uniformly distributed within the "spherical grain" structure obtained by stirring at a high stirring speed (560 rpm) than in the structure containing a combination of dendritic, rosettelike and spherical grains, which results from stirring at a low stirring speed (325 rpm), cf. Figures 24(b) to 27(b). The last regions to solidify within the casting are where the γ-γ' eutectic islands precipitate. The micropores that mostly originated from solidification shrinkage are frequently formed near the γ-γ' islands. As a consequence, the distribution of the microporosity is expected to be more uniform in the ingot that was stirred at a higher speed than in the ingot processed at a low stirring speed.

(b) Effect of Isothermal Stirring Time

The effect of the isothermal stirring time on the resultant rheocast structure is compared at a constant stirring speed of 325 rpm and a volume fraction solid of 35%; and with varying isothermal stirring times of 15 and 45 minutes. Increasing the isothermal stirring time improves the macro- and microsegregation, grain refinement and morphology of the rheocast ingot (cf. Figures 24 to 29). This improvement in the resultant rheocast structure can be attributed to the enhanced dendrite fragmentation and coarsening that takes place in the primary solid particles as the isothermal stirring time in the mushy zone increases.

Most of the bent dendritic or rosettelike primary solid particles found at a short isothermal stirring time of 15 minutes (Figure 73), are replaced by spherical primary solid particles as the stirring time increases to 45 minutes (Figure 75). With longer isothermal stirring times, the resultant increase in the number of spherical primary particles implies that the amount of dendrite arm fragmentation increases as the stirring time increases. Similar results regarding the effect of the stirring time on the size and shape of the primary solid particles have been obtained by Taha and Mahallawy (107) in characterizing the microstructure of rheocast stainless steel. The longer the paddle is stirred in the liquid melt, the more the dendrite arms are plastically deformed or bent by the stirring-induced shear stress.

The number of primary solid particles has been seen to increase as the isothermal stirring time increases; however, the primary particle size in the ingots stirred for longer times (Figure 75), is larger than the bent dendrite arms or particles in the ingots stirred for shorter times (Figure 73). This increase in the size of the primary particles can be attributed to the enhanced coarsening resulting from both isothermal holding and stirring. In fact, by comparing the morphology of the primary dendrite arms in nonstirred samples observed after 5 minutes of isothermal holding (Figure 71), with that observed after 20 minutes of isothermal holding (Figure 72), during the reheating experiment, it is clear that a coarsening process has taken place during isothermal holding without stirring. The radius of curvature of the solid-liquid interface, especially at the dendrite tip,

has increased as expected with the isothermal holding time, because the coarsening is driven by interfacial energy reduction. As stirring is introduced during isothermal holding, the primary solid particles will be coarsened not only by the reducation in the interfacial energy, as expected, but also by the faster solute transport that results from stirring. This was also suggested by Vogel et al. (65); that is, with stirring of the slurry, solute transport by diffusion need only occur across a thin boundary layer around a growing or dissolving particle. Transport across the remaining interparticle distances can be achieved by fluid flow, giving a higher rate of solute transport and thus faster coarsening rates. Therefore, a very long isothermal stirring time is not desirable, because the grain refinement achieved by increasing stirring time can be eventually counteracted by the excessive coarsening. Incidentally, the surface energy-driven changes inside an individual particle, i.e. the change from a rosette shape to a sphere, should not be accelerated by fluid flow, since the fluid flow is unlikely to penetrate between the rosette arms (65).

The macrosegregation of the resultant rheocast ingot is reduced by increasing the isothermal stirring time during solidification. This improvement in the chemical homogeneity of the macrostructure can be explained by the fact that increasing the stirring time increased the quantity of spherical primary solid particles at the same volume fraction solid and therefore could give rise to an easier mass feeding as the stirring paddle was pulled from the liquid melt after completely terminating stirring.

Increasing the isothermal stirring time in the mushy zone clearly

increases the time available for solute diffusion to occur in the primary solid particles. Therefore, the solute content can be expected to be more homogeneous and closer to the equilibrium composition in the primary solid particles isothermally stirred for 45 minutes of than in those stirred for 15 minutes. The higher chemical homogeneity in the primary solid particles with a longer stirring time would thus lead to a higher solute content at the grain center and a reduced microsegregation, i.e., more homogeneous grains, in the resultant rheocast ingot (cf. Tables IV to VI). In addition, the distribution of the $\gamma$-$\gamma'$ eutectic islands in the rheocast ingot becomes more uniform as the isothermal stirring time increases, Figures 24 (b) to 29(b). The increasing uniformity in the distribution of the eutectic islands is due to the fact that most of the primary solid particles observed after 45 minutes of isothermal stirring are spherical.

(c). Effect of Volume Fraction Solid

At a constant isothermal hold time and stirring speed, the degree of macro- and microsegregation in the resultant rheocast ingot decreases as the volume fraction solid increases (cf. Figures 24, 30 and 31, and Tables IV and VII). In addition, increasing the volume fraction solid reduces the grain size and improves the sphericity of the grains. These improvements in the rheocast structure can be attributed to (i) increasing stirring time; (ii) increasing the fluid-induced shear stress on the dendrite arms; and (iii) increasing the solute concentration gradient.

The effect of volume fraction solid on the rheocast structure is

studied at a constant isothermal stirring speed. However, in order to keep a constant cooling rate of 4°C/minute, the time spent on cooling from the liquidus temperature, $T_L$, to the desired temperature, $T_{fs}$, increases as the $T_{fs}$ decreases, i.e., at the volume fraction solid increases. Therefore, the total stirring time is the longest in the ingot isother- mally stirred at 65% fs and then decreases in the order of 50% fs and 35% fs. Furthermore, the apparent viscosity of the slurry clearly increases as the volume fraction solid increases (6). Accordingly, in order to keep the paddle at a constant stirring speed, the amount of power or shearing needed to agitate the slurry of a higher viscosity (a higher volume fraction solid) is higher than that needed to agitate the slurry of a lower viscosity (a lower volume fraction solid). Therefore, the dendrite arms can be expected to be subjected to an increasing shear stress as the volume fraction solid increases. Consequently, at a constant stirring speed and a constant isothermal stirring time, dendrite arm fragmentation occurs more readily (due to a higher shear stress), and the spherical morphology of the particles is more stable (because of a larger total stirring time) in the primary solid particles stirred at a higher volume fraction solid of 65% (Figure 76) than in those stirred at a low volume fraction solid of 35% (Figure 73).

Most spherical primary solid particles observed in the specimen of a high volume fraction solid of 65% (Figure 76) are not isolated; instead they tend to coalesce and form agglomerates. However, in the rheocast structure, the number of agglomerates observed increases as the volume fraction solid increases (cf. Figures 24(b), 30(b) and 31(b)).

This agglomeration of the spherical or rounded particles is believed to result from particle collision during stirring. Increasing the volume fraction solid in the mushy zone shortens the interparticle distance and thus can enhance the possibility of interparticle collisions. The representative composition profile obtained from the WDS analysis inside an agglomerate of the rheocast structure is shown in Figure 33. Without exception, all the boundaries observed inside this agglomerate are solute-enriched; this confirms that they are not "recrystallized" boundaries. It is suggested that during stirring at a high volume fraction solid, sintering of particles may be occurring after particle collision.

For both ingots stirred at high volume fraction solids of 50% and 65%, the stirring paddle was left in the slurry during furnace cooling, because the viscosity or stiffness of the slurry was too high to remove the paddle after stirring was stopped. Therefore, the V-shaped region having coarse equiaxed dendrite grains (observed in the ingot stirred at a low volume fraction solid of 35% shown in Figure 24(a)) is not observed in the ingots stirred at volume fraction solids of 50% and 65%. Instead, the primary solid particles, which were uniformly distributed during stirring, tend to sink due to gravity. This gives rise to a region of coarse equiaxed dendritic grains at the top of the ingots (Figures 30(a) and 31(a)). However, the area of the coarse equiaxed-dendritic grains is smaller in the ingot stirred at a higher volume fraction solid of 65% (Figure 31(a)), than in the ingot stirred at a lower volume fraction solid of 50% (Figure 30(a)). The reduced macrosegregation obtained by stirring at an inc. ased volume fraction

solid can be attributed to (i) a reduced volume fraction of liquid; and (ii) an increased viscosity.

The microsegregation of the rheocast ingot is reduced by increasing the volume fraction solid stirred isothermally during the mushy zone (cf. TablesVII and I During solidification, as the temperature drops (i.e., the volume fraction solid increases), it is clear that the difference in the solute content between the center and boundary of a solid particle increases (neglecting solute diffusion in the solid), and therefore results in an increasing solute concentration gradient in the solid particles. It is assumed here that the particle size does not significantly change with varying volume fraction solid. On subsequent isothermal stirring, the solute content gained at the particle center would increase because an increasing solute concentration gradient in a particle at a constant diffusion coefficient and time would give rise to an increasing net flux of solute atoms transported from particle boundary to center. Consequently, the resultant rheocast grains in the ingot stirred at a higher volume fraction solid (Table VII), show a more homogeneous solute distribution, i.e., a higher solute content in the grain center and a lower segregation ratio, than those in the ingot stirred at a lower volume fraction solid (Table IV).

A-3 VADER

The micro- and macrostructures obtained from the VADER process, Figures 38 and 37, are significantly different from those produced by the conventional VIM process, see the example of the

nonstirred casting shown in Figures 20(b) and 20(a). In the VADER process, two horizontal electrodes are consumed (melted) by striking an arc between them, and the molten droplets fall towards the mold. Droplets have been thought to contain solid particles or nuclei as they fall into the mold. It has been pointed out earlier that the solid particles or nuclei formed during the early stages of solidificaton will tend to sink because of their lower solute content than the surrounding liquid. However, this gravity effect, resulting from density differences between the solid and the liquid phases, is unlikely to happen in the VADER process, because the semi-liquid mass is continually being fed by the falling metal droplets. The numerous solid particles or nuclei will then be uniformly distributed throughout the semiliquid mass where no distinct liquid pool or liquidus isotherms exist. As a consequence, a uniform nondendritic grain size and reduced macro-segregation in the resultant ingot are produced by the VADER process.

The grain size obtained by the VADER process, Figure 38, is smaller than the secondary dendrite arm spacing obtained from the nonstirred casting, Figure 20(b). This difference in the grain size or dendrite arm spacing can be attributed to the difference in the cooling rate between the VADER and the nonstirred casting. In VADER, the metal droplets were dripped into a slowly rotated steel mold. It is known that the steel mold has a higher thermal conductivity than ceramic molds, specifically, the alumina crucible used in the nonstirred series of experiments. Consequently, the grain size in the VADER ingot is smaller than that in the rheocasting ingots.

It is interesting to note that the microsegregation, i.e.,

segregation ratio, in the grain or dendrite arm is similar in the VADER process (Table XII) and in the nonstirred castings (Table III). This can be explained by the fact that in the VADER process, the solid particles or nuclei survived in the metal droplets, which had a temperature slightly lower than the liquidus temperature of the IN-100 alloy, exhibit a solute content close to that of the primary nuclei formed during solidification when the temperature of the liquid melt is that of the liquidus temperature. However, the nonuniform size distribution of the $\gamma$-$\gamma'$ eutectic islands observed in the interdendritic and intergranular regions of the nonstirred casting, Figure 21, is not observed in the structure of the VADER ingot, Figure 38. A specimen sectioned from the VADER ingot was reheated to a temperature corresponding to a volume fraction solid of 65%, isothermally held for 5 minutes and subsequently water quenched. The primary solid particles are fine, spherical and uniformly distributed in the reheated structure, as shown in Figure 79. It is clear that no dendritic particles are observed in this reheated VADER sample. As a consequence, these fine and spherical particles will result in a uniform distribution of $\gamma$-$\gamma'$ eutectic islands in the resultant VADER ingot.

B. Structural Response to Post Solidification Thermal Treatment

B-1 Hot Isostatic Processing (HIP)

HIP causes solute redistribution and increases homogeneity of the component (see Figure 80). This is to be expected since the 3-hour isothermal hold and subsequent slow cooled inherent in the HIP cycle promote solid-state diffusion and therefore decrease the level of

microsegregation.

The grain size does not significantly change after HIP in the rheocast ingots (cf. Figures 42 to 24(b), 43 to 27(b)), nor in the nonstirred ingot. However, that is not the case for the VADER ingot. A much larger grain size is observed in the VADER ingot after HIP (Figure 43) than before (Figure 38). Moreover, after HIP, the quantity of $\gamma$-$\gamma'$ eutectic islands precipitated at grain boundaries is reduced in the rheocast ingots and the nonstirred ingot (compare Figures 42 and 24(b); 43 and 27(b)); however, the $\gamma$-$\gamma'$ eutectic islands have almost disappeared in the VADER ingot (cf. Figures 44 to 38). These structural differences as a result of HIP in all three cases - nonstirred, rheocast and VADER - can be attributed to variations in the chemical homogeneity of the microstructure.

A homogenization experiment was carried out in order to evaluate the degree of chemical homogeneity in each of the three solidification processes. Specimens sectioned from nonstirred, rheocast and VADER ingots were heated in the tube furnace under argon to a temperature of 1180°C (2160°F) or 1200°C (2190°F); then the samples were isothermally held for 3 hours and subsequently air cooled to room temperature. The reason these two temperatures were chosen was that they are higher than the $\gamma'$ solvus temperature of 1104°C (2020°F) (Figure 18) and were expected to be just above or below the critical melting point of the $\gamma$-$\gamma'$ eutectic phase in the IN-100 alloy, which had 0.06 w/o of carbon content. Burton (33) has shown by DTA analysis that the melting point of the $\gamma$-$\gamma'$ eutectic phase in the IN-100 alloy with a 0.18 w/o of carbon content is 1175°C (2147°F). It is believed

that a decrease in the carbon content may increase the solution temperature of the γ-γ' eutectic phase. A Chromel-Alumel type (K-type) thermocouple was inserted into each sample to make sure the temperature of the sample was accurately monitored, within ±0.6°C (1°F). The rheocasting specimens used in this experiment were obtained from the rheocast ingot stirred at a stirring speed of 325 rpm, an isothermal stirring time of 15 minutes and a volume fraction solid of 65%. The microstructures observed after 3 hours of isothermal holding at temperatures of 1180°C (2160°F) and 1200°C (2190°F) are shown in Figures 81 and 82, respectively, for the nonstirred casting, rheocasting and VADER. It should be noted that none of the three structures are completely homogenized at the low holding temperature of 1180°C (2160°F ) as shown in Figure 81. Interestingly, a clear distinction of black and white areas is observed in all three samples shown in Figure 81. The amount of the black area observed is the least in the VADER sample, followed, respectively, by the rheocast and non-stirred samples. Figure 83 shows a representative SEM micrograph of a semigrain or dendritic arm including a γ-γ' eutectic island, a coarse grain boundary γ' particle and MC carbides. It is noted that the dark area shown in Figure 81 is due to mixing of coarse and fine irregularly shaped γ' precipitates (Figure 84(b)), while the white area is obviously a region of very fine blocky shaped γ' precipitates (Figure 84(a)). Moreover, each of the γ-γ' eutectic islands, the coarse grain boundary γ' and MC carbides is also surrounded by the very fine blocky shaped γ' precipitates, i.e., white area, Figure 81. The formation of these size distribution of γ' precipitates in the matrix (see Figures 83 to 84), can

be attributed to the original-size γ' precipitates and to the kinetics of the γ' dissolution in the matrix during the homogenization. It has been shown by Aaron and Kotler (108) that increasing the original size of a second-phase precipitate raised the time required to dissolve the precipitate at the same temperature. Accordingly, the fine γ' particles precipitated in the matrix at the center of the dendrite arms or grains can be expected to dissolve completely after the homogenization treatment at 1180°C (2160°F ) and reprecipiate with a much finer size in the subsequent air cooling, Figure 84(b). In contrast, some of the very coarse γ' particles precipitated in the matrix near the grain boundaries or interdendritic regions may need a time longer than 3 hours at 1180°C (2160°F) to dissolve. Therefore, these coarse γ' particles will have survived (or partially dissolved) after the homogenization treatment and can be expected to be surrounded by very fine γ' precipitates on subsequent air cooling. The presence of a region of very fine γ' precipitates surrounding the γ-γ' eutectic island, grain boundary γ' or MC carbides can be attributed to the mechanism of particle coarsening termed "Ostwald Ripening". These grain boundary particles, such as γ-γ' eutectic islands, are much larger than the surround- ing γ' particles precipitated in the matrix. Therefore, at a temperature of 1180°C (2160°F), there will be a diffusive flux of solute atoms from the γ' precipitates to the grain boundary particles, which will finally result in the disappearance of these γ' particles.

As the homogenization temperature is raised to 1200°C (2190°F), the region that is dark in color (mixing coarse and fine γ' particles) decreases, as expected, because larger areas of precipitated γ'

particles are dissolved in the matrix at this temperature than at a lower temperature of 1180°C (2160°F) (compare Figures 82 and 81). The decrease in the amount of the dark area, i.e. increase in the chemical homogeneity, is more pronounced in the rheocast sample (Figure 82(b)) than in the nonstirred sample (Figure 82(a)). This is further evidence in support of the conclusion discussed earlier that a rheocast structure is more homogeneous than a nonstirred structure.

The $\gamma$-$\gamma'$ eutectic islands, observed in both the rheocast and nonstirred samples in Figures 82(b) and 82(a), respectively, almost disappear in the VADER sample shown in Figure 82(c) after the homogenization treatment at 1200°C (2190°F); coarsening of the VADER grains is seen. Clearly, among the three different solidification processing techniques, the VADER structure is shown to be the most homogeneous, followed by the rheocast structure and then the nonstirred structure. The higher chemical homogeneity in the VADER process is attributed to (i) the finer grain size, (ii) smaller $\gamma$-$\gamma'$ eutectic islands, and (iii) more uniform distribution of the grain boundary phases, e.g., coarse $\gamma'$ particles and $\gamma$-$\gamma'$ eutectic islands.

According to the results obtained from the homogenization experiments, the variations of the structural reponses in different ingots after HIP can be explained. The VADER structure with a huge grain size and disappearance of $\gamma$-$\gamma'$ eutectic islands observed after HIP (Figure 44) is clearly similar to the structure of the VADER sample observed after a homogenization treatment at 1200°C (2190°F) (Figure 82(c)). It has been noted that the actual HIP temperature during isothermal hold was controlled at the range 1180 ±20°C (2160 ±35°F).

The VADER ingot in the HIP furnace was believed to be located in an area near the highest temperature of approximately 1200°C (2190°F), which would give rise to grain coarsening, as expected according to the results obtained from the homogenization experiments.

Grains in either nonstirred or rheocast ingots are not significantly coarsened after HIP. This can be expected because the existence of $\gamma$-$\gamma'$ eutectic islands and other grain boundary phases will retard the grain boundary movement during HIP. It should be pointed out that the dark and white regions observed in the structure after the homogenization treatment are not seen in the structure after HIP (Figures 42 to 44). This structural difference can be attributed to the difference in cooling rates between the two processes. The furnace cooling used in HIP exhibits much slower cooling rates than the air cooling used in the homogenization treatment. As a consequence, the $\gamma'$ particles precipitated at the center of the grain would be coarsened during the furnace cooling and would therefore result in a more uniform size distribution of $\gamma'$ particles in the grains of the structure after HIP than after homogenization treatment.

The amount of microporosity shown after solidification processing is reduced after HIP (cf. Figures 42 to 24(b), 43 to 27(b)); however, few micropores still appear, as shown in Figure 43(b). Clearly, structures of the ingots observed after HIP in a given HIP cycle (i.e., 3 hours of isothermal holding at a temperature 1180°C (2160°F) under an argon pressure of 15 ksi (105 MPa)) are not optimized. Therefore, a better HIP cycle (e.g., increases in isothermal holding time or pressure) and better temperature control in the 3°C (±5°F) range in

the HIP furnace are recommended.

B-2 Heat Treatment

After HIP, ingots were heat treated, including a solution treatment and a three-stage aging treatment, to optimize the structural response to loading. The grains are further homogenized, as expected (e.g., see Figure 80), after heat treatment. However, a slight color difference in the microstructure between the center and boundary of the dendrite arm, grain or subgrain is observed in the nonstirred, rheocast and VADER specimens, Figures 45 to 50. The occurrence of this observed color difference is believed to be due to size variations of the $\gamma'$ precipitates shown between the center and boundary of the dendritic arm, grain or subgrain, as discussed in the previous section of this chapter.

The grains of all the ingots do not significantly change their size after heat treatment; for example, compare Figures 46 and 42; 47 and 43. This is expected and can be attributed to the drag force resulting from the grain boundary phases, such as carbides, $\gamma$-$\gamma'$ eutectic islands and coarse grain boundary $\gamma'$ particles, on the movement of the grain boundary. However, most of the grains observed after heat treatment are more spherical than those observed before heat treatment.

The morphology of the $\gamma'$ precipitates at the centers of the dendrite arms, grains or subgrains has varied from a combination of cubic and dendritic shape prior to the heat treatment into a completely cubic shape after heat treatment (compare Figures 51 and 22(a), 35 or 39(a)). The $\gamma'$ precipitates dissolved at the solution temperature are

expected to reprecipitate finely as spheres during the stage of oil quenching and then grow and become cubic under the subsequent age treatment. Clearly, the dendritic γ' precipitates are not observed in the structure after heat treatment, Figure 51.

It is not surprising that the γ' precipitatesobserved near the boundaries exhibit a coarser and more irregular morphology than those observed at the centers of the dendrite arms, grains or subgrains (compare Figures 52 and 51). However, these γ' precipitates located near the grain boundary after heat treatment are finer and more spherical than those before heat treatment (compare Figures 52 and 22(b); 36 and 39(b)). This variation in the γ' morphology can be attributed to the difference in cooling rates between HIP and the solution treatment.

A γ'-denuded zone of the width of 1 μm or less is observed near most of the γ-γ' eutectic islands, carbides and grain boundary coarse γ' particles in the structure after heat treatment, Figure 52. The formation of this denuded zone can be explained by the fact that the γ' precipitates located near the γ-γ' eutectic islands, coarse grain boundary γ' particles or carbides will dissolve according to the "Ostwald Ripening" theory. However, this explanation can be accurate only at the stage of solution treatment. During the subsequent aging treatment, it was expected that more fine γ' particles would gradually reprecipitate between the preexisting γ' particles that were not dissolved during the solution treatment. These latter precipitated γ' particles are too fine to be detected with SEM microscopy. As a consequence, the γ' denuded zone observed under SEM, Figure 52, may

not be a totally precipitation-free zone. It is suggested that the actual width of the γ' denuded zone, if it exists, is probably much smaller than the width observed in Figure 52 and is dependent upon the diffusion distance ahead of the γ-γ' eutectic particles. Similarly, the volume fraction of γ' precipitates obtained at the center of the dendrite arms, grains or subgrains ( Figure 51) is underestimated.

C. Mechanical Properties

C-1 Microhardness

The mean microhardness increases from the center to the boundary of the dendrite arms and grains in the as-cast (Table XiV) and heat treated conditions (Table XV). The wide range of microhardness shown in either the center or the boundary of each sample can be explained by the difficulty of evaluating the microhardness at a consistent section or location for all 25 arbitrarily chosen grains in each sample. Generally speaking, factors that influence the microhardness of the nickel-base superalloy include:

(i) The content of alloying elements in the matrix

(ii) The size distribution and volume fraction of γ' precipitates

In the as-cast condition, the size and volume fraction of γ' precipitates did not significantly vary with different solidification processing. This can be expected because of the slow furnace cooling that is inherent to these processes. Therefore, the variation in the average microhardness, shown in Table XIV, can be attributed to the difference in the alloying contents in the matrix in the as-cast

C-2

condition. The specimen obtained from the ingot with the high volume fraction solid of 65% has been shown to have the highest alloying content, e.g., Ti and Cr, in the grain center and thus exhibit the highest mean microhardness of all the samples.

The level of microhardness in all the specimens increase as expected after the HIP and heat treatment (cf. Tables XIV to XV). However, no variation in the mean microhardness among all the nonstirred and rheocast specimens after the thermal treatment is shown in Table XV. This similarlity can be explained by the fact that the grains in the nonstirred and rheocast specimens have been heat treated to a similar homgeneity level, and in addition, a similar size distribution and volume fraction of $\gamma'$ precipitates has resulted under the same thermal treatment cycle. In contrast, for the VADER structure, the unexpected dissolution of the grain boundary $\gamma$-$\gamma'$ eutectic islands after HIP, Figure 44, has further been homogenized, i.e., increasing the alloying contents in the matrix, and this results in the highest microhardness at the grain center (Table XV). Clearly, the lowest microsegregation inherent in the VADER grains after heat treatment gives rise to the lowest microhardness at the grain boundary.

C-2 Tensile Properties

The absence of a significant difference in microstructure in terms of the volume fraction and size distribution of $\gamma'$ precipitates and the level of microsegregation between the nonstirred ingot and rheocast ingots after the HIP and heat treatment leads to the conclu-

sion that any observed differences in the tensile properties must be due to grain size.

All the rheocast specimens exhibit a higher yield strength and ultimate tensile strength than the nonstirred specimen when tested at 650°C (1200°F) in air (Table XVI). This improvement in strength can be attributed to the grain refinement achieved in the structure by introduction of the mechanical stirring during solidification. It has been shown that decreasing the grain size in nickel-base superalloy increased the yield strength and ultimate tensile strength at 650°C (1200°F) in air (84).

Increasing the stirring speed, isothermal stirring time or volume fraction solid reduces the grain size (Figures 46-49) and therefore results in an increase in the yield strength and the ultimate tensile strength (Figures 53-55). The absence of asignificant difference between varying stirring speed from 450 to 560 rpm (Figure 53) or varying volume fraction solid from 50% to 65% (Figure 55) is believed to be a result of the grain coarsening effect that occurred during thermal treatments. Some fine $\gamma$-$\gamma'$ eutectic islands located between equiaxed grains in the ingot with the stirring speed of 560 rpm may completely dissolve during thermal treatments, and this may subsequently result in a grain growth into grain sizes on an order to those observed in the ingot with the stirring speed of 450 rpm. However, the similarity of grain size observed after thermal treatment does not occur between ingots with the stirring speeds of 450 rpm and 325 rpm. This is because the rate of grain growth decreases as the number of grains decreases, i.e., as grain size increases;

therefore, grains with the stirring speed of 450 rpm won't be able to grow to the size of those observed with the low stirring speed of 325 rpm. Furthermore, it has been shown that the ingot stirred at a volume fraction solid of 65% exhibits a finer grain size and a larger number of agglomerates than that stirred at a volume fraction solid of 50%. During thermal treatment, those agglomerates would tend to be homogenized (i.e., boundaries within each agglomerate would disappear) and become coarse grains. This homogenization of agglomerates together with grain growth results in a similar order of grain size between the ingots stirred at a volume fraction solid of 65% and 35% after thermal treatment.

Ductility of approximately 2-3% does not vary among the nonstirred and rheocast specimens. This brittleness can be attributed to the residual micropores observed after HIP. VADER grains have greatly coarsened during thermal treatment and thus give rise to a low yield strength. However, VADER specimens also exhibit a similar ultimate tensile strength and slightly higher ductility than rheocast specimens.

C-3 Fatigue Crack Propagation (FCP) Behavior

Specimens obtained from the VADER and two selected rheocast ingots exhibit a lower FCP rate than those obtained from P/M processing in air at 650°C (1200°F) and 0.33 Hz (Figure 61). This variation in the FCP rate can be attributed to the large difference in the grain size observed between P/M and VADER or rheocast structures. P/M specimens have a grain size in the range of 3-5 μm and exhibit an

intergranular FCP in air at 650°C (1200°F) (Figures 64 and 65). This intergranular mode of crack propagation has been suggested to have originated from either an environmental or a creep effect. However, Gayda et al. (109) have recently studied the FCP behavior in air at 650°C (1200°F) on fine-grained Rene 95 and Astroloy and found no evidence of the creep damage on the fracture surface. Therefore, it has been concluded that the rapid intergranular crack growth of the fine-grained microstructure is largely caused by environmental damage, i.e., preferential oxidation at grain boundaries. This conclusion has been further supported by Choe et al. (110). Furthermore, it has also been concluded that a change in the mode of crack growth from intergranular to transgranular was exhibited when the fine-grained P/M specimens were treated in vacuum (84).

In contrast to the fine-grained P/M material, specimens obtained from two selected rheocast ingots and one VADER ingot have a coarse grain size, on the order of 200-500 μm (Figures 47,49 and 50). Without exception, all the much larger grained forms of specimens exhibit a mixed or transgranular mode of FCP at lower rates than the finer grained forms, as shown in Figures 66-69 and 61. Clearly, the environmental effect on FCP behavior, discussed above in regard to the fine-grained P/M specimens, is less pronounced in the large-grained specimens because the total grain boundary area is reduced by increasing the grain size. It has been shown by Gayda et al. (84) that in P/M Astroloy the transition from transgranular to intergranular FCP occurred at a grain size of less than 20 μm when tested in air at 650°C (1200°F) and 0.33 Hz. This grain size effect on the FCP behavior can be

attributed to the relative sizes of the grain and of the plastic zone developed at the crack tip under cyclic loading (111).

It has been further shown by Gayda et al. (84) that as the transgranular mode of FCP was operating, both increasing grain size and increasing yield strength raised the FCP resistance in P/M Astroloy. A relationship of the following form was found in the Paris regime (84):

$$da/dn = C(\sigma_y^{-1} d^{-1/2}) \Delta K^m \qquad (5)$$

where: $\sigma_y$: yield strength

d: average grain diameter.

Gayda et al. (109) have recently plotted (da/dn) for the various forms of Rene 95 and IN-100 materials at a given $\Delta K$ against $(\sigma_y^{-1} d^{-1/2})$ and shown that the data fit the above correlation very well where the transgranular FCP mode operated.

No significant variation of the FCP rate has observed between the rheocast specimens obtained from the highest stirring speed and highest volume fraction solid. This can be expected because the grain size and yield strength of these two rheocast ingots are on the same order after HIP and heat treatment. The VADER specimens show a similar FCP rate to the rheocast ones. Even though the VADER samples have a lower $\sigma_y$ than the rheocast ones (see Eq. 5), in the former, the grain size is larger, and thus the two effects counteract each other.

# VI. CONCLUSIONS

## A. Processing of Rheocast and VADER IN-100

### A-1 Rheocasting

1. IN-100 nickel-base superalloy can be successfully rheocast (stircast) in a specially built high-temperature vacuum furnace.

2. The conventional dendritic structure observed in the nonstirred ingot is absent. Instead it is replaced by the rosettelike or spherical structure in the rheocast ingot. The mechanism of the dendrite to nondendrite transformation achieved by the introduction of mechanical stirring during solidification can be explained as due to dendrites having undergone plastic bending, recrystallization and subsequent fragmentation of grain boundaries. However, it is not clear if this fragmentation is caused by the melting of high-energy grain boundaries (i.e., Vogel-Doherty-Cantor model) or simply by grain boundary sliding. Some grain boundaries indentified as nonsegregated boundaries in the rheocast ingot are believed to originate from the low-energy, "recrystallized" boundaries that survived after stirring. During the stage of furnace cooling, the movement of these recrystallized boundaries is slow and is further interfered with the high volume of precipitates located in grains and grain boundaries. Those nonsegregated

boundaries are observed in all rheocast ingots but not in the nonstirred ingot.

3. Ingots processed by rheocasting exhibit the following improvements in the resulting structure as compared to ingots processed by conventional casting (i.e., no stirring):

    - Reduced segregation
    - Reduced shrinkage and therefore a lower probability of ingot cracking
    - Reduced grain size
    - Reduced size and increased uniformity in the distribution of grain boundary phases, i.e., $\gamma$-$\gamma'$ eutectic islands.

4. The degree of structural enhancements inherent in rheocast ingots is influenced by three processing variables: stirring speed, isothermal stirring time and the volume fraction solid. The general trends established, reflecting the effect of processing variables on structure are

    (i) Increasing the stirring speed increases the amount of dendrite arm deformation and fragmentation, resulting in an increasing number of primary solid particles, i.e., a decrease in particle size, at a constant volume fraction solid and isothermal stirring time. This decrease in particle size provides mass feeding during the lifting of the stirring paddle. This gives rise to an increasingly uniform distribution of fine grains and grain boundary phases in the resulting rheocast structure. The

level of microsegregation is not significantly changed by varying the stirring speed.

(ii) Increasing the stirring time refines the primary solid particles and thus improves the quality of the rheocast structure at a constant stirring speed and volume fraction solid. However, coarsening is enhanced by increasing stirring time, and therefore it may adversely affect grain refining if too long a stirring time is used.

(iii) Grain refinement and structural improvement are achieved by increasing volume fraction solid at a constant stirring speed and constant isothermal stirring time. This occurs because of an increase in the shear forces on the dendrites and also an increase in the total stirring time with an increasing volume fraction solid. An increasing volume fraction solid thus greatly reduces the level of microsegregation. However, increasing the volume fraction solid increases the opportunity for interparticle collision and therefore raises the number of agglomerates.

A-2 VADER

1. The VADER process produces superalloy ingots having a uniform fine grain size. This is attributed to the numerous nuclei that exist in the droplets.

2. The steel mold used in the VADER process allows for higher cooling rates than the $Al_2O_3$ crucible used in the rheocast process. Therefore, the grain size in the VADER ingot is smaller than the dendrite arm spacing present in the nonstirred ingot and the grain size in the rheocast ingot.

3. The level of microsegregation is similar for the VADER and nonstirred castings. This is because the droplet temperature is below, but close to, the liquidus temperature.

B. Structural Response During Postsolidification Treatment

1. The observation of porosity in the ingot following HIP clearly indicates that the HIP cycle used in this study was not optimum.

2. The VADER grains coarsened significantly during HIP. This is attributed to the poor tempeature control in the HIP furnace.

3. The grain size is not significantly affected by HIP in the nonstirred and rheocast ingots. The existence of $\gamma$-$\gamma'$ eutectic islands at grain boundaries is mainly responsible for retarding grain coarsening.

4. Though grain size is not significantly affected by heat treatment, grain shape is: grains become more spherical following heat

treatment. Likewise, the morphology of secondary precipitated γ' particles is affected by heat treatment. It becomes more cubic subsequent to heat treatment, as expected.

C. Mechanical Properties

C-1 Microhardness

1. The mean microhardness increases from the center to the boundary of the dendrite arms and grains in the as-cast and heat treated conditions.

2. In the as-cast condition, the ingot stirred at the high volume fraction solid of 65% has the highest alloying content at the grain center, and thus exhibits the highest mean microhardness compared to ingots processed by rheocasting with lower volume fractions of solid, as well as ingots processed by the other methods.

3. The level of microhardness within the grains increases subsequent to thermal treatment. In the heat treated material, microhardness measurements within the grains indicate similar levels of hardness for the nonstirred (conventional casting) and rheocast materials.

C-2 Tensile Properties

1. Grain size is the predominant factor in determining the tensile strength at 650°C (1200°F) in air.

2. All the rheocast ingots are superior in yield strength to both VADER and nonstirred ingots. The nonstirred ingot has the worst ultimate tensile strength among all the differently processed ingots.

3. Increasing the stirring speed from 325 to 450 rpm, increasing the isothermal stirring time or increasing the volume fraction solid from 35% to 50% reduces the grain size and therefore increases the level of strength. However, no significant difference in strength is detected when stirring speed is changed from 450 to 560 rpm or volume fraction solid changes from 50% to 65%.

4. No significant differences in ductility were detected as a function of processing variables, processing techniques or grain size. The presence of microporosity in specimens after HIP and heat treatment, rather than the underlying microstructure, is believed to control the level of ductility.

5. All the rheocast ingots exhibit better yield strength and comparative ultimate tensile strength than the commercially cast IN-100.

C-3 Fatigue Crack Propagation (FCP) Behavior

1. Larger-grained specimens obtained from rheocast and VADER ingots

are more beneficial than the fine-grained specimens obtained from P/M processing in terms of crack propagation resistance in the temperature range in which aircraft gas turbine engine disk rim operate. The fracture mode of FCP in the rheocast and VADER specimens is transgranular; in contrast, the P/M specimens show an intergranular and environmentally influenced fracture mode of FCP.

2. No significant differences in FCP rate and fracture exist between the two chosen rheocast ingots and the VADER ingot.

# VII. SUGGESTIONS FOR FUTURE WORK

In this study, the nickel-base superalloy IN-100 has been successfully rheocast and VADER processed under high-vacuum conditions. From the results of the study, it is clear that an ingot of nondendritic fine grain size, reduced segregation and reduced shrinkage can be achieved via two novel solidification techniques, i.e., rheocasting and VADER. It appears that many ultrahigh-strength superalloys that cannot be conventionally processed using VIM-VAR techniques can now be rheocast or VADER processed. These two processes will give metallurgists alternatives to powder metallurgy for the manufacture of sophisticated high-strength turbine disk alloys.

However, no attempt in this study was made to rheocast the nickel-base superalloy in the continuous rheocasting unit. In addition, even though the study included an investigation to further explain rheocast structures during isothermal stirring and after furnace cooling, a full understanding of rheocasting and VADER mechanisms has not been completed. Therefore, the following recommendations are made for future studies:

1. Processing and structural characterization
   (a). Research into the possible use of rheocasting techniques on a continuous basis to process nickel-base superalloys.

(b). Investigate the effect of cooling rate during solidification on the resultant rheocast structure.

(c). Quantitatively evaluate rheocast structures through optical or SEM image analyses, e.g., evaluate the quantity, size and distribution of $\gamma$-$\gamma'$ eutectic particles, the volume fraction of $\gamma'$ precipitates in the matrix and the amount of the microporosity in each ingot.

(d). Study the rheocasting mechanism through:

(i) direct visual observation of the breakdown of growing solids by use of transparent materials.

(ii) a design of in-situ quench in the high-temperature and high-vacuum rheocasting furnace.

(iii) a simple rheocast unit to rheocast low-temperature alloys, such as Al-base alloys. Samples can be picked up during stirring and then water quenched.

(e). Using the Kossel camera in the SEM, evaluate the misorientation angles between grains in the specimens obtained from rheocast ingots.

(f). Using directionally solidified ingots as initial electrodes in the VADER process, investigate the origin of nuclei formed in the liquid droplets.

2. Postsolidification thermal treatment

(a). Investigate an optimium HIP cycle for rheocast and VADER processed IN-100 ingots.

(b). Do TEM on volume fraction, size and distribution of $\gamma'$ precipitates in the matrix and along the grain boundaries of the ingot after thermal treatment.

## TABLE I

(a) Nominal Composition of As-Received IN-100 (for Rheocasting Studies)

| | wt% | | wt% |
|---|---|---|---|
| Ni | 55.37 | C | 0.06 |
| Co | 18.85 | Si | 0.05 |
| Cr | 12.08 | Cb | 0.05 |
| Al | 4.97 | Zr | 0.04 |
| Ti | 4.56 | B | 0.012 |
| Mo | 2.99 | Mn | 0.01 |
| V | 0.78 | Cu | 0.01 |
| Fe | 0.13 | O | 0.006 |
| Ta | 0.10 | N | 0.001 |
| W | 0.10 | | |

(b) Nominal Composition of VADER IN-100

| | wt% | | wt% |
|---|---|---|---|
| Ni | 55.28 | C | 0.07 |
| Co | 18.78 | Si | 0.05 |
| Cr | 12.38 | Cb | 0.05 |
| Al | 4.90 | Zr | 0.05 |
| Ti | 4.43 | B | 0.01 |
| Mo | 3.17 | Mn | 0.01 |
| V | 0.65 | Cu | 0.01 |
| Fe | 0.12 | O | 0.001 |
| Ta | 0.10 | N | 0.001 |
| W | 0.10 | | |

TABLE II

Summary of Rheocast Runs and the

Corresponding Processing Variables Maintained

| Run # | Volume Fraction Solid fs,% | Stirring Speed γ, rpm | Isothermal Stirring Time ts, minute | |
|---|---|---|---|---|
| #6 | | (non-stirred) | | |
| #9<br>#19 | 35 | 325 | 15 | *N |
| #13<br>#22 | 35 | 450 | 15 | N |
| #18<br>#29 | 35 | 560 | 15 | N |
| #10<br>#25 | 35 | 325 | 45 | N |
| #27 | 50 | 325 | 15 | *P |
| #26 | 65 | 325 | 15 | P |

*N = ingot without paddle left in it.
*P = ingot with paddle left in it.

TABLE III Concentration and Segregation Ratio of Non-Stirred Ingot

| | Ti | | | Cr | | |
|---|---|---|---|---|---|---|
| | K ratio % | | | K ratio % | | |
| Grain # | $C_0$ | $C_{mid}$ | S | $C_0$ | $C_{mid}$ | S |
| 1 | 2.72 | 3.80 | 1.40 | 10.60 | 11.45 | 1.08 |
| 2 | 2.93 | 3.98 | 1.36 | 10.85 | 11.60 | 1.07 |
| 3 | 2.84 | 3.92 | 1.38 | 10.80 | 11.63 | 1.08 |
| 4 | 3.15 | 3.97 | 1.26 | 11.11 | 11.65 | 1.05 |
| 5 | 2.98 | 3.98 | 1.34 | 10.94 | 11.60 | 1.06 |
| 6 | 2.92 | 3.97 | 1.36 | 10.86 | 11.62 | 1.07 |
| 7 | 3.03 | 4.00 | 1.32 | 11.04 | 11.70 | 1.06 |
| 8 | 3.25 | 4.10 | 1.26 | 11.10 | 11.70 | 1.05 |
| 9 | 2.75 | 3.84 | 1.40 | 10.58 | 11.50 | 1.09 |
| 10 | 3.35 | 4.08 | 1.22 | 11.21 | 11.82 | 1.05 |
| 11 | 2.94 | 3.88 | 1.32 | 10.83 | 11.66 | 1.08 |
| 12 | 3.54 | 4.12 | 1.16 | 11.30 | 11.70 | 1.04 |
| 13 | 2.81 | 3.82 | 1.36 | 10.72 | 11.60 | 1.08 |
| 14 | 3.60 | 4.09 | 1.14 | 11.40 | 11.75 | 1.03 |
| 15 | 2.79 | 3.88 | 1.39 | 10.50 | 11.50 | 1.10 |
| 16 | 2.92 | 3.94 | 1.35 | 10.90 | 11.72 | 1.08 |
| 17 | 2.84 | 3.86 | 1.36 | 10.67 | 11.63 | 1.09 |
| 18 | 2.69 | 3.81 | 1.42 | 10.43 | 11.42 | 1.10 |
| 19 | 3.74 | 4.11 | 1.10 | 11.45 | 11.80 | 1.03 |
| 20 | 2.90 | 3.98 | 1.37 | 10.85 | 11.61 | 1.07 |
| Mean and Standard Deviation | 3.03 ±0.30 | 3.96 ±0.11 | 1.31 ±0.09 | 10.91 ±0.28 | 11.63 ±0.11 | 1.07 ±0.02 |

$C_0$ = Concentration at the center of grain.

$C_{mid}$ = Concentration at the midpoint between grain center and boundary

S = Segregation ratio, $C_{mid}/C_0$.

TABLE IV Concentration and Segregation Ratio of Rheocast Ingot (v = 325 rpm, $t_s$ = 15 minutes, fs = 35%)

| | Ti | | | Cr | | |
|---|---|---|---|---|---|---|
| | K ratio % | | | K ratio % | | |
| Grain # | $C_o$ | $C_{mid}$ | S | $C_o$ | $C_{mid}$ | S |
| 1 | 3.44 | 4.02 | 1.17 | 11.14 | 11.78 | 1.06 |
| 2 | 3.61 | 4.22 | 1.17 | 11.68 | 11.92 | 1.02 |
| 3 | 3.23 | 3.90 | 1.21 | 10.84 | 11.70 | 1.08 |
| 4 | 3.02 | 3.94 | 1.30 | 10.83 | 11.59 | 1.07 |
| 5 | 3.19 | 3.91 | 1.23 | 10.74 | 11.59 | 1.08 |
| 6 | 3.22 | 3.93 | 1.22 | 11.05 | 11.62 | 1.05 |
| 7 | 3.60 | 3.93 | 1.09 | 11.33 | 11.80 | 1.04 |
| 8 | 3.38 | 3.95 | 1.17 | 11.12 | 11.64 | 1.05 |
| 9 | 3.16 | 3.89 | 1.23 | 10.95 | 11.67 | 1.06 |
| 10 | 3.63 | 4.01 | 1.10 | 11.43 | 11.75 | 1.03 |
| 11 | 3.34 | 3.94 | 1.18 | 10.99 | 11.72 | 1.07 |
| 12 | 3.24 | 3.97 | 1.23 | 11.01 | 11.65 | 1.06 |
| 13 | 3.28 | 3.93 | 1.20 | 11.05 | 11.57 | 1.05 |
| 14 | 3.16 | 4.06 | 1.28 | 10.84 | 11.70 | 1.08 |
| 15 | 3.34 | 3.98 | 1.19 | 11.15 | 11.64 | 1.04 |
| 16 | 3.25 | 3.99 | 1.23 | 10.94 | 11.61 | 1.06 |
| 17 | 3.16 | 3.92 | 1.24 | 11.03 | 11.54 | 1.05 |
| 18 | 3.18 | 3.94 | 1.24 | 10.97 | 11.66 | 1.06 |
| 19 | 3.25 | 3.88 | 1.19 | 10.99 | 11.78 | 1.07 |
| 20 | 3.27 | 3.99 | 1.22 | 11.10 | 11.67 | 1.05 |
| Mean and Standard Deviation | 3.29 ±0.15 | 3.97 ±0.19 | 1.20 ±0.11 | 11.06 ±0.22 | 11.68 ±0.11 | 1.06 ±0.01 |

$C_o$ = Concentration at the center of grain.

$C_{mid}$ = Concentration at the midpoint between grain center and boundary

S = Segregation ratio, $C_{mid}/C_o$.

TABLE V Concentration and Segregation Ratio of Rheocast Ingot (v = 560 rpm, $t_s$ = 15 minutes, fs = 35%)

| | Ti | | | Cr | | |
|---|---|---|---|---|---|---|
| | K ratio % | | | K ratio % | | |
| Grain # | $C_o$ | $C_{mid}$ | S | $C_o$ | $C_{mid}$ | S |
| 1 | 3.67 | 4.20 | 1.14 | 11.66 | 11.90 | 1.02 |
| 2 | 3.25 | 3.90 | 1.20 | 10.93 | 11.65 | 1.06 |
| 3 | 3.33 | 3.94 | 1.18 | 11.10 | 11.69 | 1.05 |
| 4 | 3.19 | 3.89 | 1.22 | 10.87 | 11.34 | 1.06 |
| 5 | 3.24 | 3.85 | 1.19 | 10.97 | 11.65 | 1.06 |
| 6 | 3.21 | 3.97 | 1.24 | 11.04 | 11.69 | 1.06 |
| 7 | 3.29 | 4.03 | 1.22 | 11.05 | 11.58 | 1.05 |
| 8 | 3.25 | 3.88 | 1.19 | 10.97 | 11.65 | 1.06 |
| 9 | 3.22 | 3.92 | 1.22 | 11.15 | 11.68 | 1.05 |
| 10 | 3.15 | 3.87 | 1.23 | 10.97 | 11.53 | 1.05 |
| 11 | 3.17 | 3.93 | 1.24 | 10.85 | 11.66 | 1.07 |
| 12 | 3.31 | 4.05 | 1.22 | 11.09 | 11.73 | 1.06 |
| 13 | 3.29 | 3.92 | 1.19 | 10.99 | 11.66 | 1.06 |
| 14 | 3.35 | 3.99 | 1.23 | 11.13 | 11.66 | 1.05 |
| 15 | 3.24 | 3.91 | 1.21 | 11.02 | 11.62 | 1.05 |
| 16 | 3.60 | 4.12 | 1.14 | 11.50 | 11.85 | 1.03 |
| 17 | 3.27 | 3.92 | 1.20 | 10.94 | 11.66 | 1.07 |
| 18 | 3.17 | 3.99 | 1.26 | 11.00 | 11.70 | 1.06 |
| 19 | 3.30 | 3.92 | 1.19 | 11.15 | 11.67 | 1.05 |
| 20 | 3.27 | 4.00 | 1.22 | 11.09 | 11.64 | 1.05 |
| Mean and Standard Deviation | 3.29 ±0.13 | 3.97 ±0.09 | 1.20 ±0.03 | 11.07 ±0.20 | 11.67 ±0.09 | 1.05 ±0.01 |

$C_o$ = Concentration at the center of grain.

$C_{mid}$ = Concentration at the midpoint between grain center and boundary

S = Segregation ratio, $C_{mid}/C_o$.

TABLE VI Concentration and Segregation Ratio of Rheocast Ingot (v = 325 rpm, $t_s$ = 45 minutes, fs = 35%)

| | Ti | | | Cr | | |
|---|---|---|---|---|---|---|
| | K ratio % | | | K ratio % | | |
| Grain # | $C_o$ | $C_{mid}$ | S | $C_o$ | $C_{mid}$ | S |
| 1 | 3.30 | 3.92 | 1.19 | 11.07 | 11.69 | 1.06 |
| 2 | 3.29 | 3.93 | 1.19 | 11.05 | 11.55 | 1.05 |
| 3 | 3.35 | 3.95 | 1.18 | 11.01 | 11.64 | 1.06 |
| 4 | 3.34 | 3.99 | 1.19 | 11.13 | 11.70 | 1.05 |
| 5 | 3.98 | 4.53 | 1.14 | 11.65 | 11.89 | 1.02 |
| 6 | 3.25 | 3.90 | 1.20 | 11.04 | 11.65 | 1.05 |
| 7 | 3.27 | 3.91 | 1.19 | 11.10 | 11.63 | 1.06 |
| 8 | 3.22 | 3.90 | 1.21 | 11.01 | 11.59 | 1.05 |
| 9 | 3.99 | 4.25 | 1.07 | 11.32 | 11.87 | 1.05 |
| 10 | 3.36 | 4.02 | 1.19 | 11.09 | 11.70 | 1.05 |
| 11 | 3.40 | 3.91 | 1.15 | 10.98 | 11.60 | 1.06 |
| 12 | 3.35 | 4.02 | 1.20 | 11.17 | 11.72 | 1.05 |
| 13 | 3.34 | 3.99 | 1.19 | 11.09 | 11.59 | 1.05 |
| 14 | 3.29 | 3.97 | 1.20 | 11.10 | 11.67 | 1.05 |
| 15 | 3.38 | 4.00 | 1.18 | 11.07 | 11.62 | 1.05 |
| 16 | 3.29 | 3.94 | 1.20 | 11.13 | 11.65 | 1.05 |
| 17 | 3.27 | 3.93 | 1.20 | 10.99 | 11.59 | 1.05 |
| 18 | 3.36 | 3.93 | 1.17 | 11.03 | 11.61 | 1.05 |
| 19 | 3.85 | 4.22 | 1.10 | 11.49 | 11.93 | 1.04 |
| 20 | 3.34 | 3.95 | 1.18 | 11.00 | 11.65 | 1.06 |
| Mean and Standard Deviation | 3.41 ±0.23 | 4.01 ±0.14 | 1.18 ±0.04 | 11.13 ±0.17 | 11.68 ±0.10 | 1.05 ±0.01 |

$C_o$ = Concentration at the center of grain.

$C_{mid}$ = Concentration at the midpoint between grain center and boundary

S = Segregation ratio, $C_{mid}/C_o$.

TABLE VII Concentration and Segregation Ratio of Rheocast Ingot (v = 325 rpm, $t_s$ = 15 minutes, fs = 65%)

| | Ti | | | Cr | | |
|---|---|---|---|---|---|---|
| | K ratio % | | | K ratio % | | |
| Grain # | $C_o$ | $C_{mid}$ | S | $C_o$ | $C_{mid}$ | S |
| 1 | 3.47 | 4.01 | 1.16 | 11.23 | 11.60 | 1.03 |
| 2 | 3.63 | 4.03 | 1.11 | 11.36 | 11.69 | 1.03 |
| 3 | 3.55 | 4.09 | 1.15 | 11.27 | 11.64 | 1.03 |
| 4 | 3.51 | 4.04 | 1.15 | 11.29 | 11.52 | 1.02 |
| 5 | 3.48 | 3.99 | 1.15 | 11.35 | 11.63 | 1.03 |
| 6 | 3.40 | 3.95 | 1.16 | 11.27 | 11.70 | 1.04 |
| 7 | 3.54 | 4.12 | 1.16 | 11.31 | 11.64 | 1.03 |
| 8 | 3.61 | 4.04 | 1.12 | 11.32 | 11.67 | 1.03 |
| 9 | 3.79 | 4.08 | 1.08 | 11.32 | 11.66 | 1.03 |
| 10 | 3.50 | 4.03 | 1.15 | 11.21 | 11.62 | 1.04 |
| 11 | 3.56 | 4.13 | 1.20 | 11.23 | 11.63 | 1.04 |
| 12 | 3.47 | 4.02 | 1.16 | 11.21 | 11.57 | 1.03 |
| 13 | 3.50 | 4.02 | 1.15 | 11.37 | 11.72 | 1.03 |
| 14 | 3.52 | 4.11 | 1.17 | 11.34 | 11.59 | 1.02 |
| 15 | 3.55 | 4.07 | 1.15 | 11.29 | 11.60 | 1.03 |
| 16 | 3.67 | 4.09 | 1.11 | 11.37 | 11.67 | 1.03 |
| 17 | 3.58 | 4.07 | 1.14 | 11.26 | 11.65 | 1.03 |
| 18 | 3.54 | 4.04 | 1.14 | 11.23 | 11.63 | 1.04 |
| 19 | 3.48 | 4.10 | 1.18 | 11.23 | 11.70 | 1.04 |
| 20 | 3.50 | 3.98 | 1.14 | 11.38 | 11.59 | 1.02 |
| Mean and Standard Deviation | 3.54 ±0.09 | 4.05 ±0.05 | 1.15 ±0.03 | 11.29 ±0.02 | 11.63 ±0.05 | 1.03 ±0.01 |

$C_o$ = Concentration at the center of grain.

$C_{mid}$ = Concentration at the midpoint between grain center and boundary

S = Segregation ratio, Cmid/Co.

## TABLE VIII

## Nominal Composition of Rheocast IN-100

| | wt% | | wt% |
|---|---|---|---|
| Ni | 55.53 | C | 0.06 |
| Co | 18.67 | Si | 0.05 |
| Cr | 11.99 | Cb | 0.05 |
| Al | 4.95 | Zr | 0.04 |
| Ti | 4.63 | B | 0.013 |
| Mo | 3.01 | Mn | 0.01 |
| V | 0.79 | Cu | 0.01 |
| Fe | 0.14 | O | 0.005 |
| Ta | 0.10 | N | 0.001 |
| W | 0.10 | | |

TABLE IX. Effect of Stirring Speed on Resultant Rheocast Structure

| Processing Variables | | | Primary Solid Particles | | Segregations | | Grains | | γ-γ' Eutectic Phase | |
|---|---|---|---|---|---|---|---|---|---|---|
| γ | $t_s$ | fs | Size | Spheri-city | Macro | Micro | Size | Spheri-city | Amount | Uniformity of Distribution |
| ↑ | — | — | ↓ | ↑ | ↓ | — | ↓ | ↑ | ↓ | ↑ |

↑ = Increase

↓ = Decrease

TABLE X. Effect of Isothermal Stirring Time on Resultant Rheocast Structure

| Processing Variables | | | Primary Solid Particles | | Segregations | | Grains | | γ-γ' Eutectic Phase | | |
|---|---|---|---|---|---|---|---|---|---|---|---|
| γ | $t_s$ | fs | Size | Spheri-city | Macro | Micro | Size | Spheri-city | Size | Amount | Uniformity of Distribution |
| – | ↑ | – | ↓ | ↑ | ↓ | ↓ | ↓ | ↑ | – | * ↓ | ↑ |

↑ = Increase

↓ = Decrease

* = Expected due to low level of microsegregation

TABLE XI. Effect of Volume Fraction Solid on Resultant Rheocast Structure

| Processing Variables | | | Primary Solid Particles | | Segregations | | Grains | | γ-γ' Eutectic Phase | | |
|---|---|---|---|---|---|---|---|---|---|---|---|
| γ | $t_s$ | fs | Size | Spheri-city | Macro | Micro | Size | Spheri-city | Size | Amount | Uniformity of Distribution |
| – | – | ↑ | ↓ | ↑ | ↓ | ↓ | ↓ | ↑ | – | ↓* | – |

↑ = Increase

↓ = Decrease

* = Expected due to low level of microsegregation

TABLE XII Concentration and Segregation Ratio of VADER Ingot

| | Ti | | | Cr | | |
|---|---|---|---|---|---|---|
| | K ratio % | | | K ratio % | | |
| Grain # | $C_0$ | $C_{mid}$ | S | $C_0$ | $C_{mid}$ | S |
| 1 | 2.95 | 3.98 | 1.35 | 10.86 | 11.42 | 1.05 |
| 2 | 3.10 | 4.01 | 1.29 | 10.75 | 11.60 | 1.08 |
| 3 | 3.03 | 3.99 | 1.32 | 10.85 | 11.65 | 1.07 |
| 4 | 2.98 | 3.88 | 1.30 | 10.93 | 11.80 | 1.08 |
| 5 | 2.85 | 3.93 | 1.38 | 10.85 | 11.57 | 1.07 |
| 6 | 3.01 | 4.21 | 1.40 | 11.00 | 11.75 | 1.07 |
| 7 | 2.89 | 3.95 | 1.37 | 10.87 | 11.63 | 1.07 |
| 8 | 2.90 | 3.97 | 1.37 | 10.93 | 11.69 | 1.07 |
| 9 | 3.43 | 4.35 | 1.27 | 11.21 | 11.86 | 1.06 |
| 10 | 2.84 | 3.89 | 1.37 | 10.72 | 11.75 | 1.10 |
| 11 | 3.01 | 3.95 | 1.31 | 10.82 | 11.60 | 1.07 |
| 12 | 3.35 | 4.03 | 1.20 | 11.07 | 11.61 | 1.05 |
| 13 | 3.00 | 4.10 | 1.37 | 10.93 | 11.65 | 1.07 |
| 14 | 2.87 | 3.88 | 1.35 | 10.95 | 11.73 | 1.07 |
| 15 | 2.89 | 3.88 | 1.35 | 11.00 | 11.69 | 1.06 |
| 16 | 3.03 | 4.01 | 1.33 | 10.84 | 11.62 | 1.07 |
| 17 | 2.94 | 4.10 | 1.39 | 10.79 | 11.65 | 1.08 |
| 18 | 2.89 | 3.95 | 1.37 | 10.83 | 11.73 | 1.08 |
| 19 | 3.10 | 4.20 | 1.35 | 11.09 | 11.80 | 1.06 |
| 20 | 2.80 | 3.85 | 1.37 | 10.70 | 11.47 | 1.07 |
| Mean and | 2.99 | 4.01 | 1.34 | 10.90 | 11.67 | 1.07 |
| Standard Deviation | ±0.05 | ±0.13 | ±0.05 | ±0.13 | ±0.11 | ±0.01 |

$C_0$ = Concentration at the center of grain.

$C_{mid}$ = Concentration at the midpoint between grain center and boundary

S = Segregation ratio, $C_{mid}/C_0$.

## TABLE XIII

### Nominal Compositions of Rheocast and VADER IN-100

### After HIP and Heat Treated

| Rheocast | wt% | VADER | wt% |
|---|---|---|---|
| Ni | 55.37 | Ni | 55.25 |
| Co | 18.95 | Co | 18.74 |
| Cr | 11.95 | Cr | 12.37 |
| Al | 5.04 | Al | 4.93 |
| Ti | 4.77 | Ti | 4.49 |
| Mo | 3.03 | Mo | 3.16 |
| V | 0.77 | V | 0.65 |
| Fe | 0.15 | Fe | 0.12 |
| Ta | 0.10 | Ta | 0.10 |
| W | 0.10 | W | 0.10 |
| C | 0.06 | C | 0.07 |
| Si | 0.06 | Si | 0.05 |
| Cb | 0.05 | Cb | 0.05 |
| Zr | 0.05 | Zr | 0.05 |
| B | 0.016 | B | 0.019 |
| Mn | 0.01 | Mn | 0.01 |
| Cu | 0.01 | Cu | 0.01 |
| O | 0.005 | O | 0.005 |
| N | 0.001 | N | 0.001 |

TABLE XIV

Microhardness at the Grain Center and Near Grain Boundary in As Cast Condition, VHN

| | | Center | | Boundary | |
|---|---|---|---|---|---|
| | Sample # | Range | Mean & Standard Deviation | Range | Mean & Standard Deviation |
| 1 | Non-stirred | 318-380 | 350 ± 20 | 385-420 | 394 ± 7 |
| 2 | VADER | 326-378 | 354 ± 7 | 378-415 | 396 ± 5 |
| 3 | #19 | 330-377 | 354 ± 13 | 378-417 | 395 ± 7 |
| 4 | #29 | 335-380 | 355 ± 7 | 379-417 | 394 ± 5 |
| 5 | #10 | 343-384 | 358 ± 9 | 378-420 | 396 ± 7 |
| 6 | #26 | 330-373 | 365 ± 7 | 384-420 | 393 ± 7 |

TABLE XV

Microhardness at the Grain Center and Near Grain Boundary After Heat Treatment, VHN

| | | Center | | Boundary | |
|---|---|---|---|---|---|
| | Sample # | Range | Mean & Standard Deviation | Range | Mean & Standard Deviation |
| 1 | Non-stirred | 420-438 | 429 ± 6 | 453-470 | 458 ± 5 |
| 2 | VADER | 430-445 | 440 ± 5 | 439-455 | 446 ± 4 |
| 3 | #19 | 420-435 | 428 ± 5 | 454-468 | 460 ± 5 |
| 4 | #29 | 424-438 | 430 ± 5 | 453-467 | 460 ± 3 |
| 5 | #10 | 423-437 | 431 ± 6 | 452-468 | 459 ± 5 |
| 6 | #26 | 425-438 | 430 ± 6 | 453-468 | 459 ± 5 |

TABLE XVI. Experimental Results Showing Tensile Properties of IN-100

| | Sample # | Volume Fraction Solid fs,% | Stirring Speed $\dot{\gamma}$, RPM | Isothermal Stirring Time $t_s$,min. | Yield Strength Ksi | Yield Strength Average Ksi | Yield Strength Average MPa | Ultimate Tensile Strength Ksi | Ultimate Tensile Strength Average Ksi | Ultimate Tensile Strength Average MPa | Elongation % |
|---|---|---|---|---|---|---|---|---|---|---|---|
| 1 | Commercial Cast | | | | - | 129 | 890 | - | 161 | 1110 | 6 |
| 2 | Non-Stirred | | | | 122<br>128 | 126 | 869 | 124<br>130 | 127 | 874 | 2-2.5 |
| 3 | VADER | | | | 128<br>130 | 129 | 890 | 153<br>155 | 154 | 1062 | 4 |
| 4 | #19 | 35 | 325 | 15 | 136<br>138 | 137 | 944 | 143<br>145 | 144 | 993 | 2-2.5 |
| 5 | #22 | 35 | 450 | 15 | 147<br>146 | 146 | 1010 | 155<br>155 | 155 | 1069 | 3 |
| 6 | #29 | 35 | 560 | 15 | 147<br>147 | 147 | 1014 | 155<br>155 | 155 | 1069 | 2-3 |
| 7 | #10 | 35 | 325 | 45 | 146<br>- | 146 | 1007 | 153<br>- | 153 | 1055 | 2-3 |
| 8 | #20 | 50 | 325 | 15 | 144<br>- | 144 | 993 | 151<br>- | 151 | 1041 | 2-3 |
| 9 | #26 | 65 | 325 | 15 | 144<br>146 | 145 | 1000 | 151<br>151 | 151 | 1041 | 2-3 |

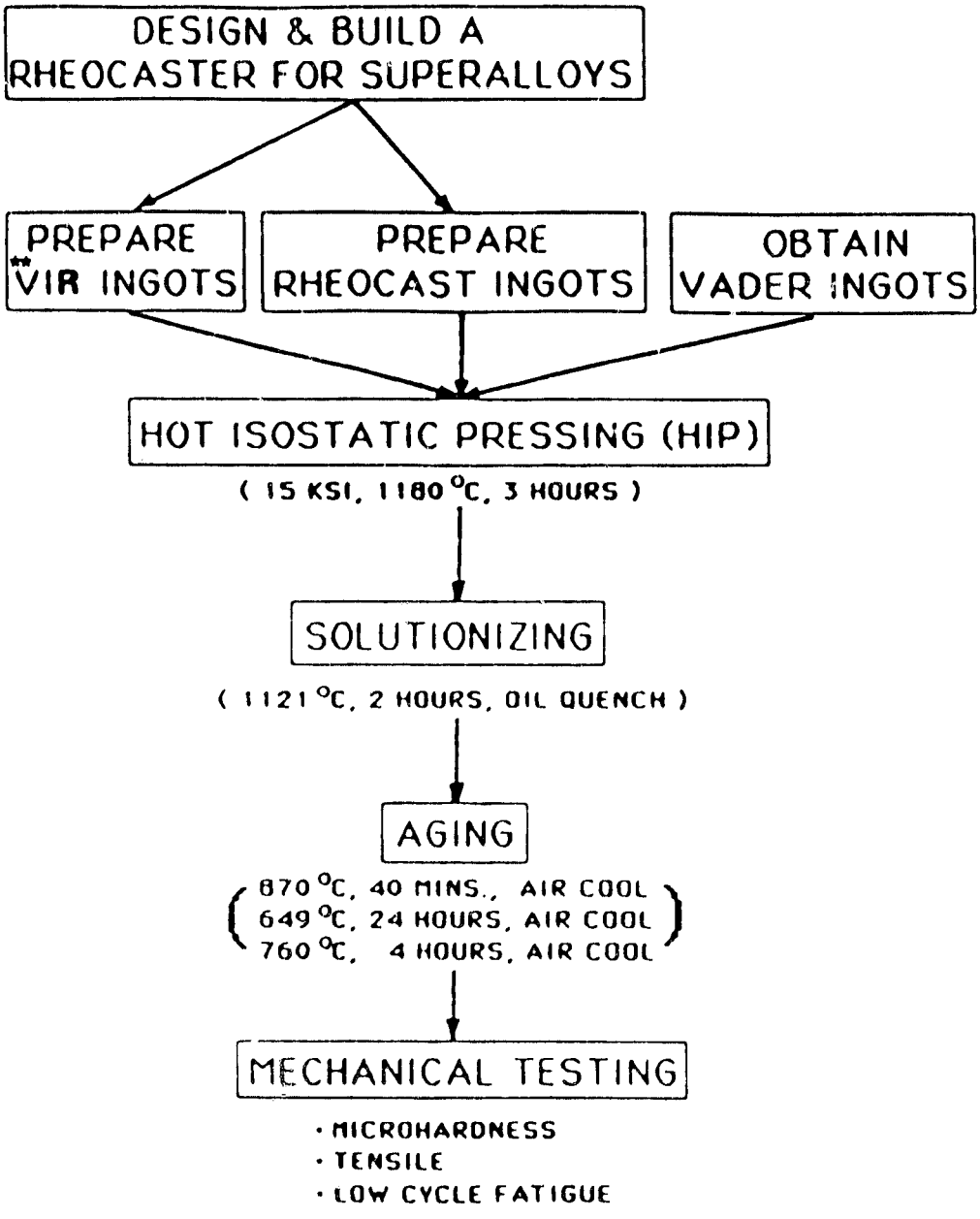


**VIR : Vacuum Induction Remelting (non-stirred)

Figure 1. A schematic of the overall program.

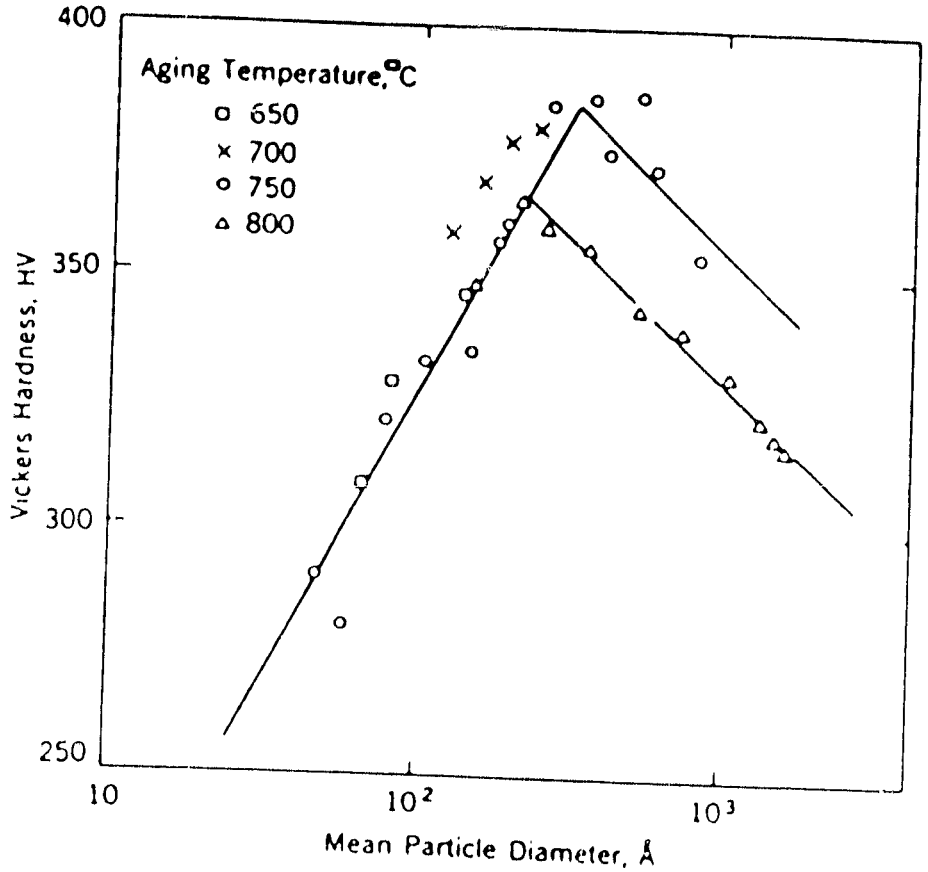


Figure 2. Relation between particle diameter of γ' and hardness for a nickel-base alloy with 22% Cr, 2.8% Ti, 3.1% Al. (42).

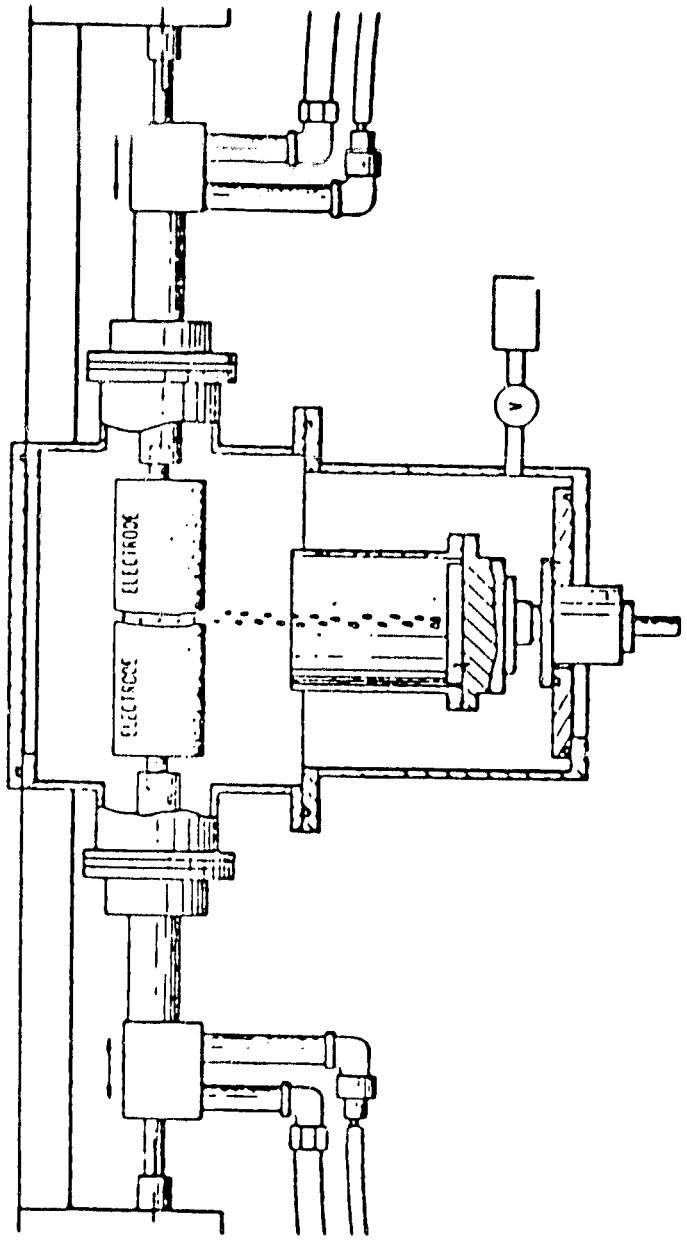


Figure 3. Schematic diagram of the VADER melting process (5).

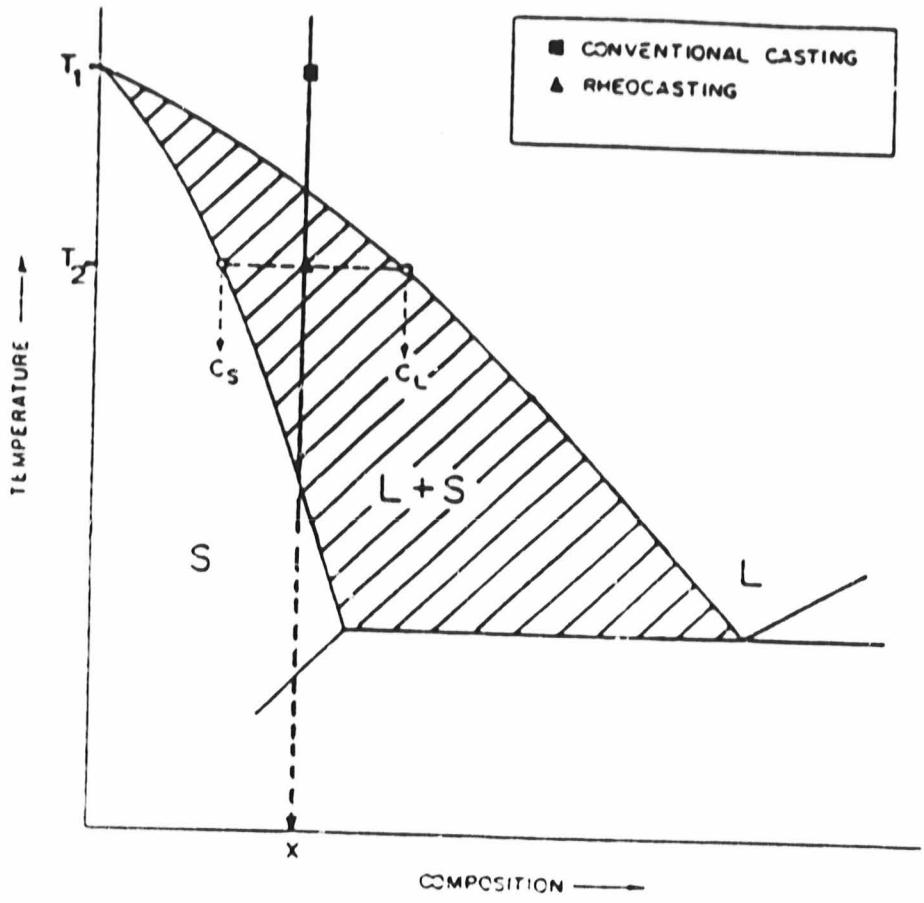


Figure 4. Phase diagram showing conventional casting at $T_1$ and rheocasting at $T_2$.

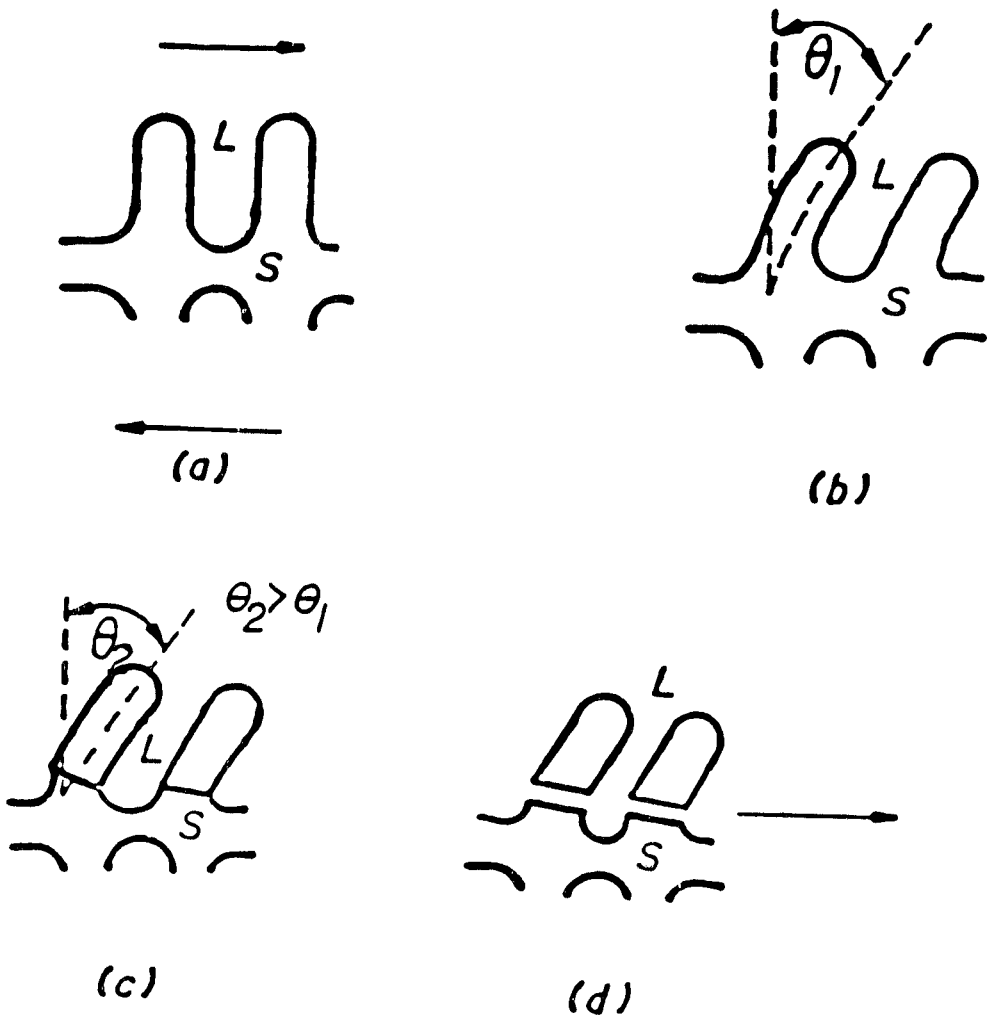


Figure 5. Schematic model of the grain boundary fragmentation mechanism. ( 63).

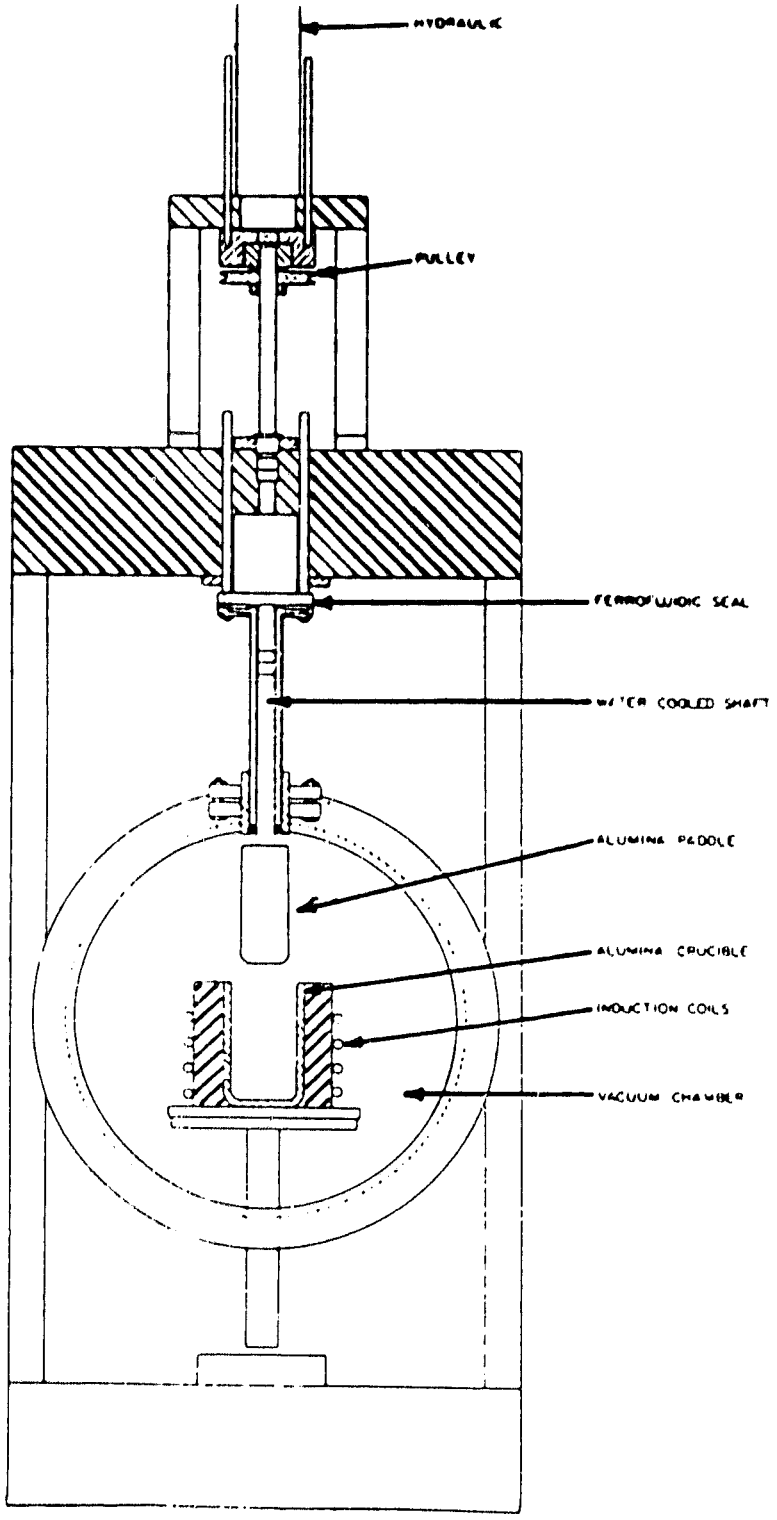


Figure 6. Schematic diagram of rheocasting apparatus.

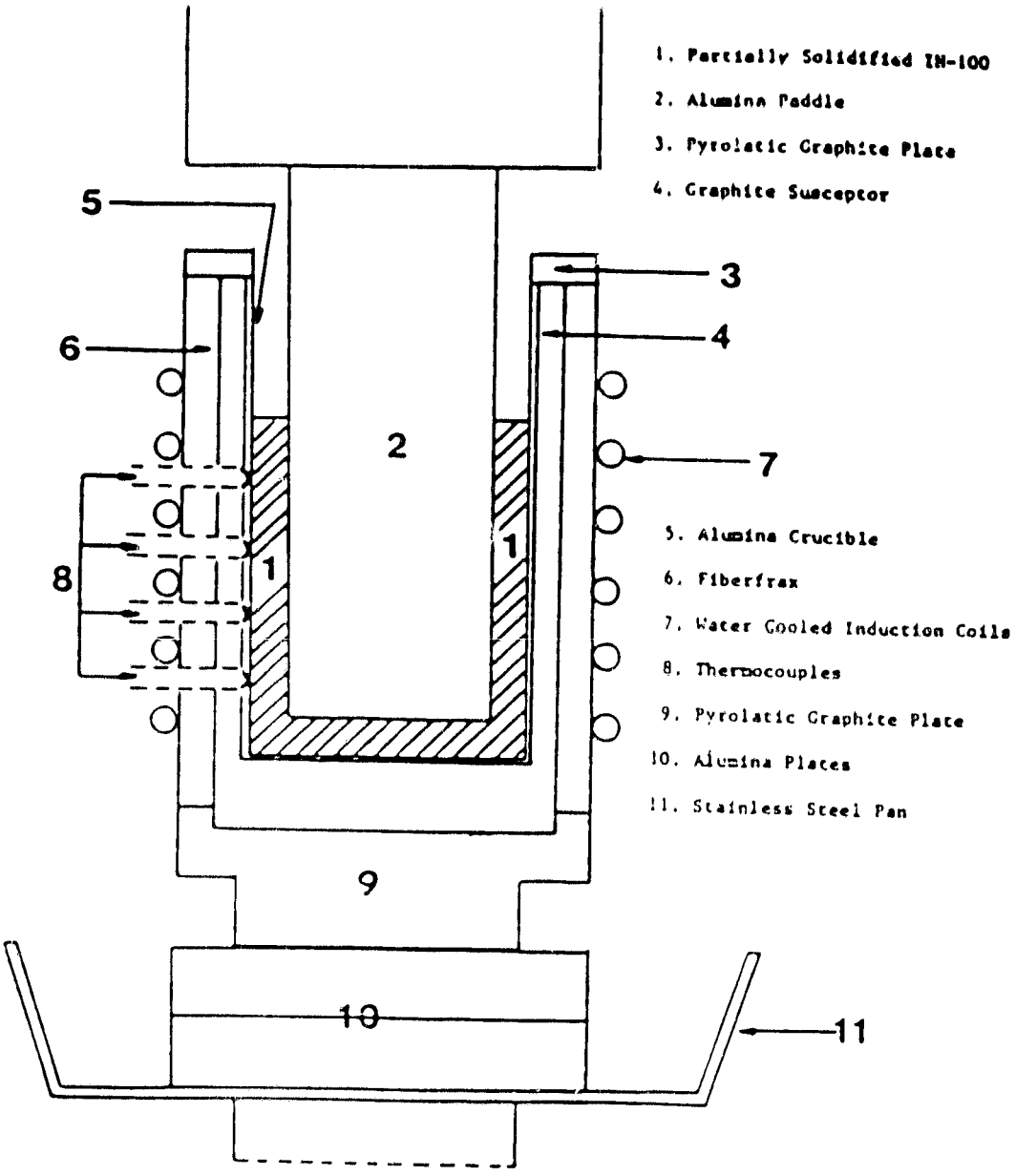


Figure 7. Details of the crucible assembly in rheocasting furnace.

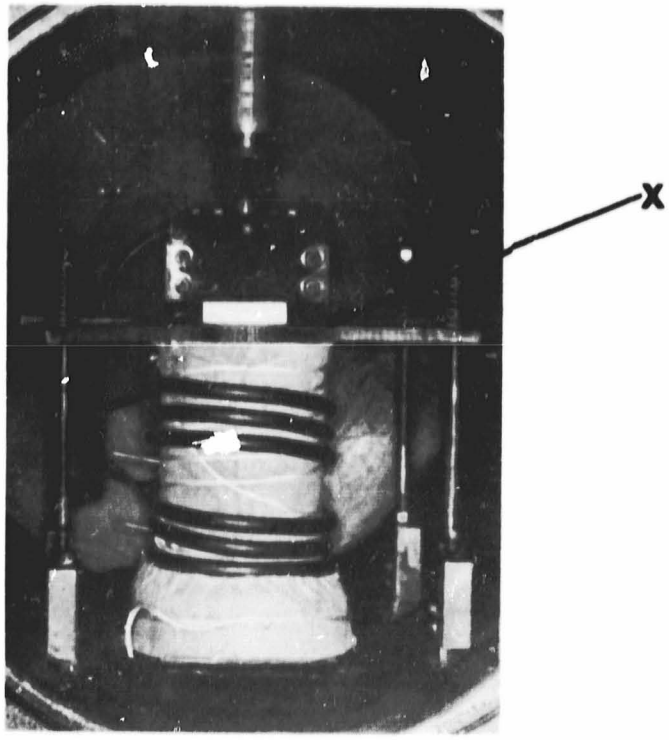


Figure 8. Photograph of the total assembly in rheocasting furnace.

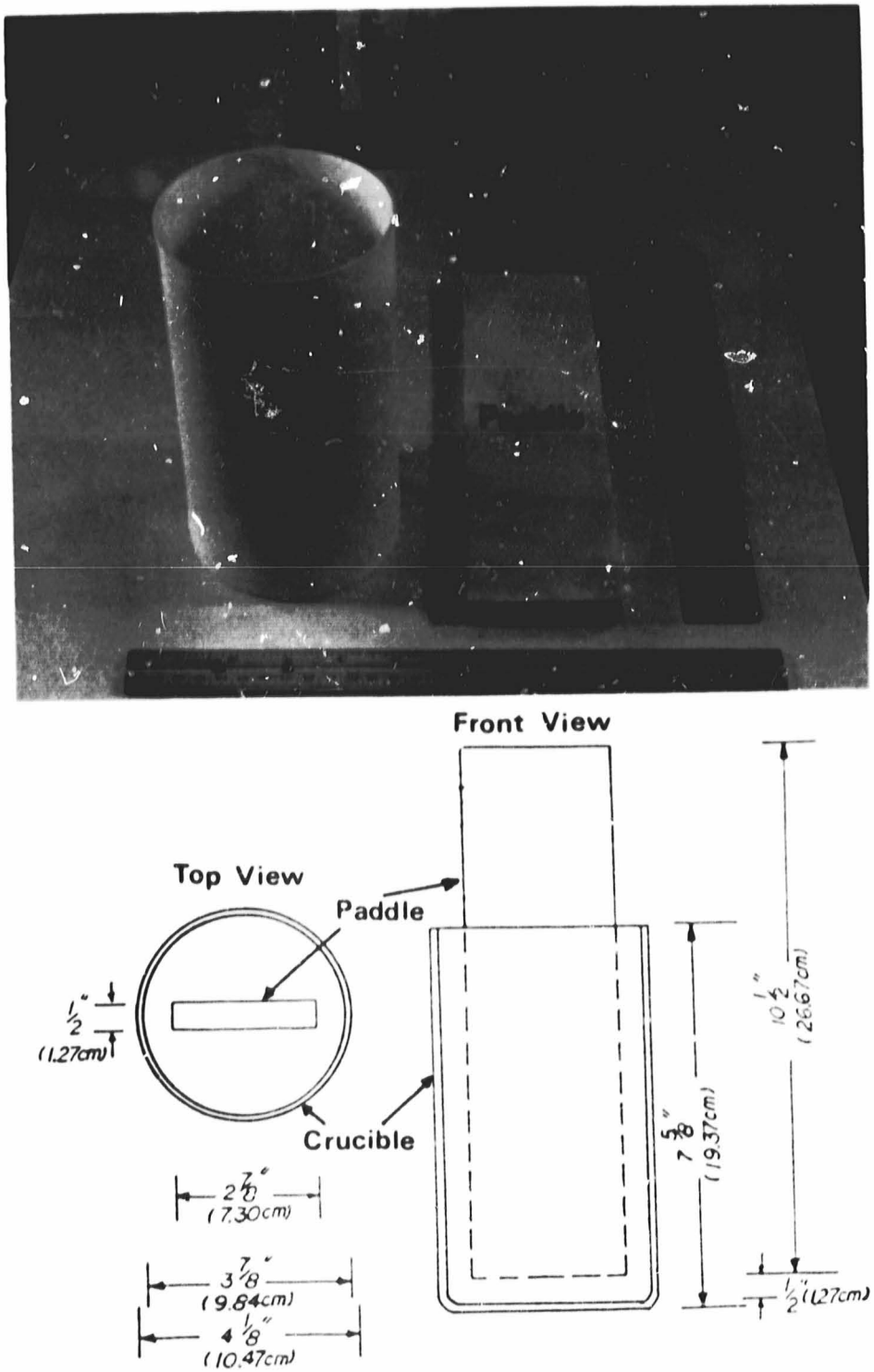


Figure 9. Photograph and schematic of the crucible and paddle.

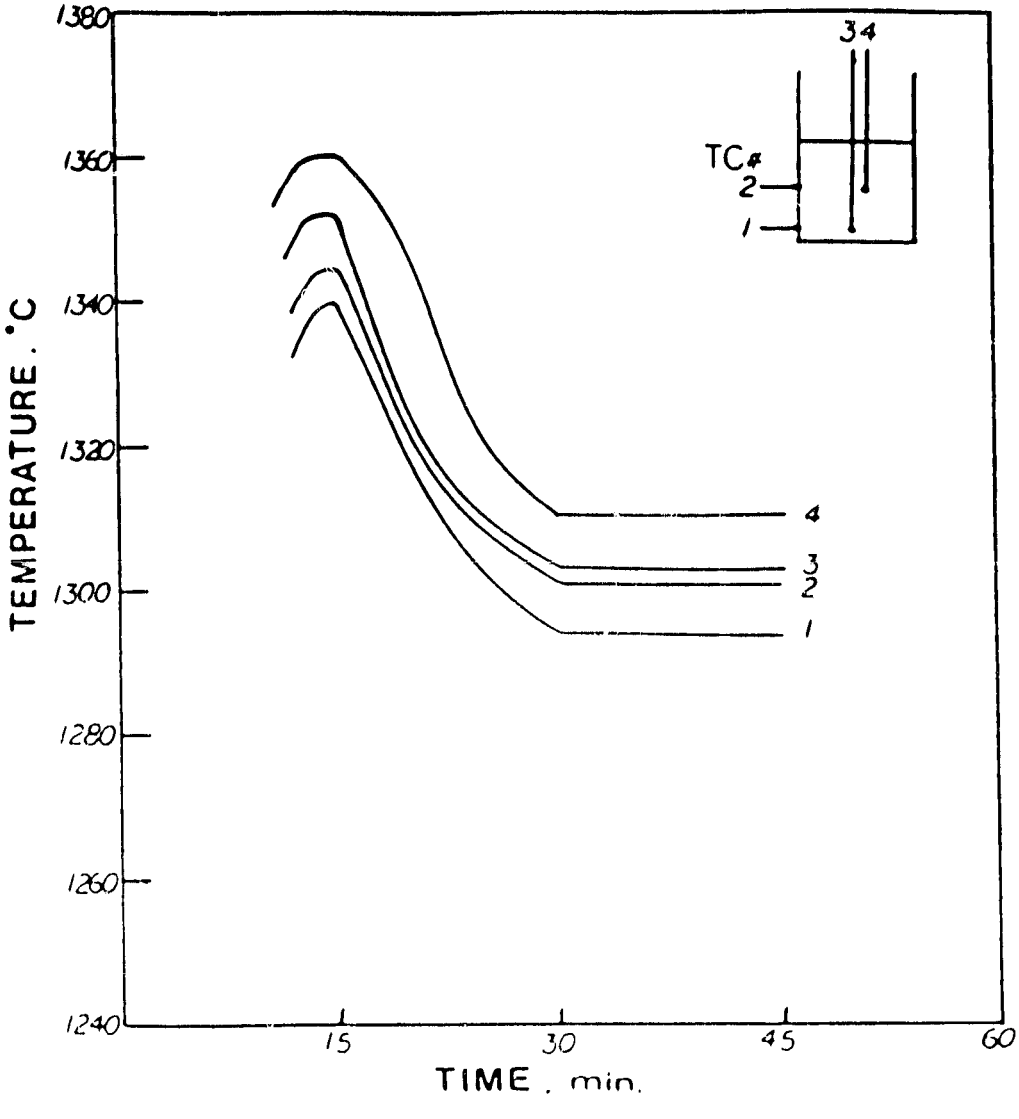


Figure 10. Thermal profile during solidification for thermocouples at different locations.

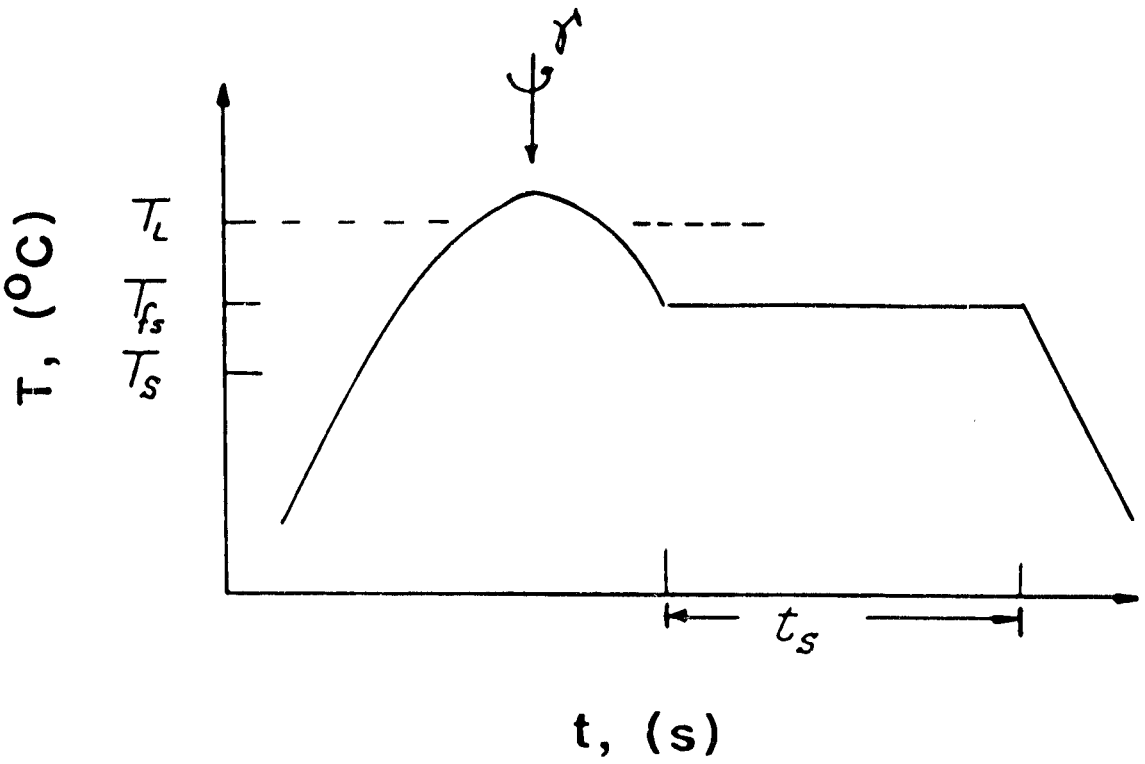


$T$ is temperature

$T_L$ is liquidus temperature

$T_{fs}$ is temperature at which sample was rheocasted

$T_S$ is solidus temperature

$t$ is time

$t_s$ is time of stirring (isothermal)

$\dot{\gamma}$ is applied shear rate, and shows start of rheocasting

Figure 11. Graphical presentation of the process approach and the variables.

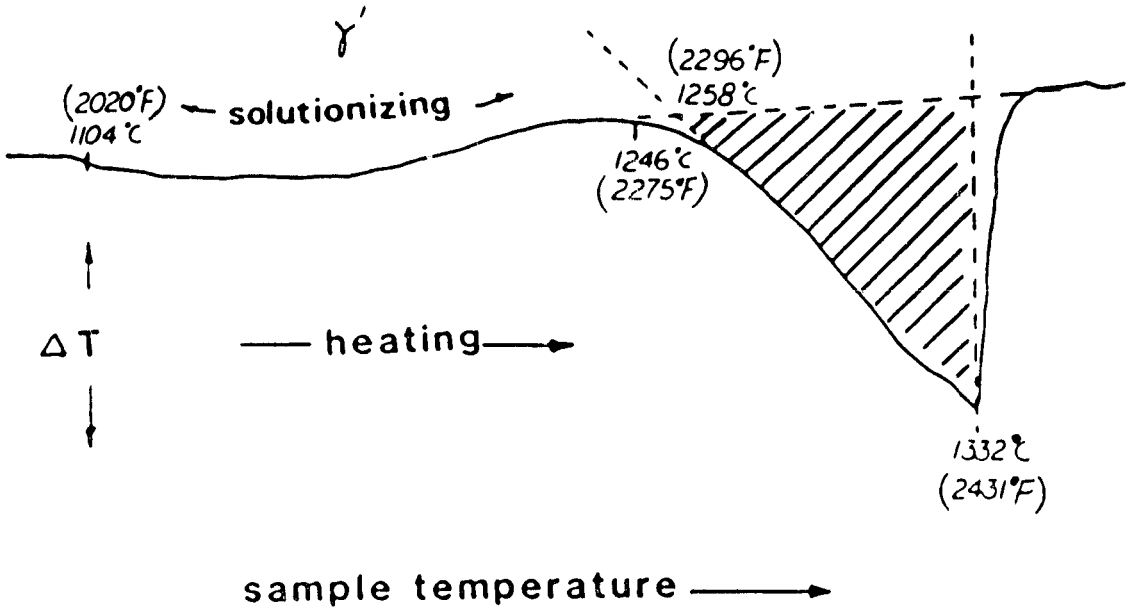


Figure 12. On-heating DTA thermogram of the as-received IN-100 alloy.

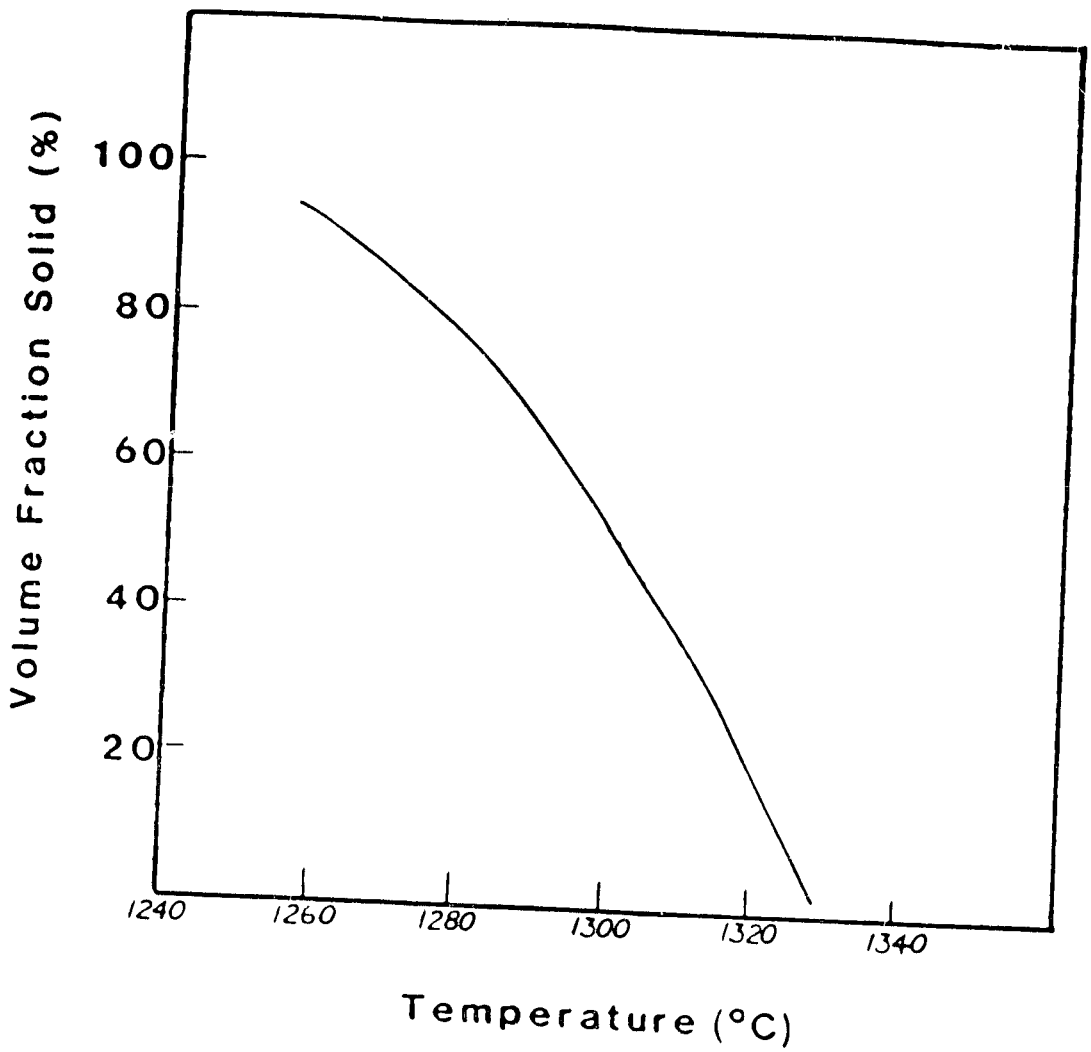


Figure 13. Measured volume fraction solid versus temperature for IN-100.

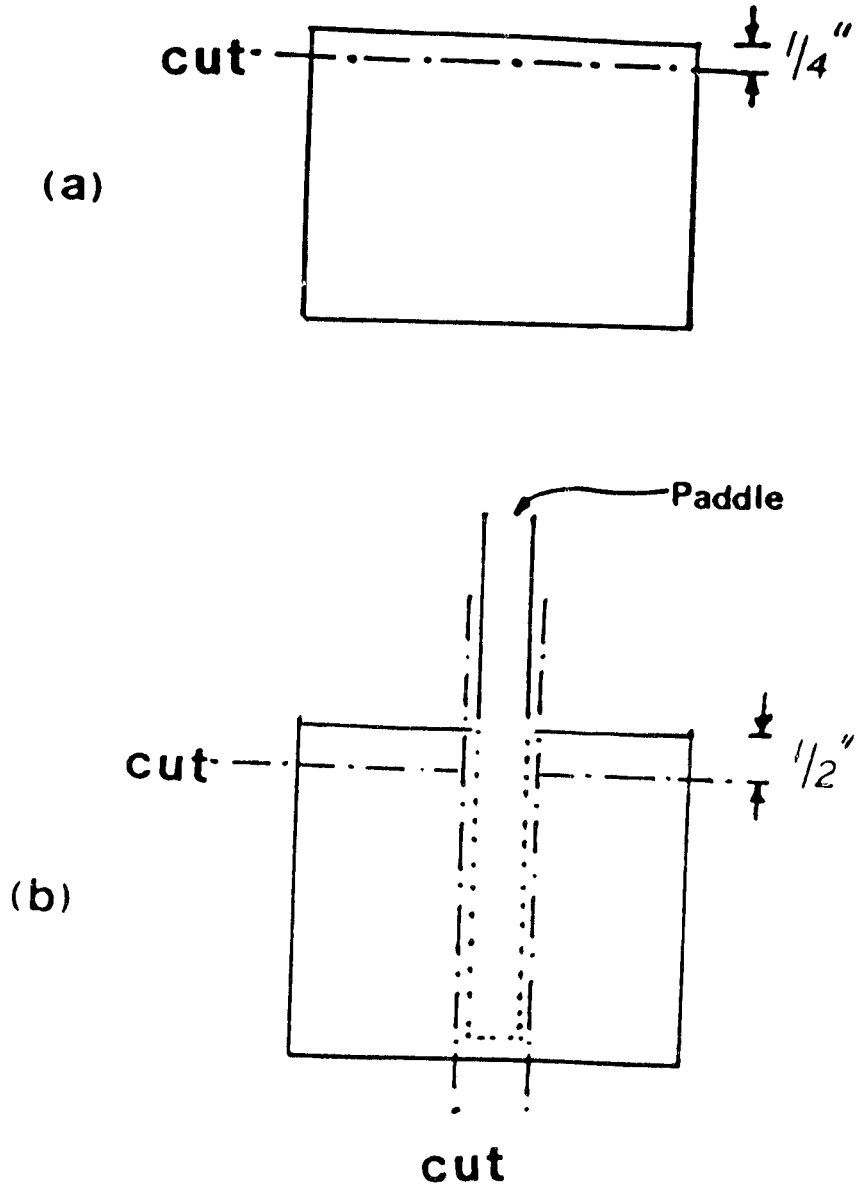


Figure 14. Schematic diagrams illustrating the sectioning mode of the rheocast IN-100 ingot: (a) without paddle; (b) with paddle.

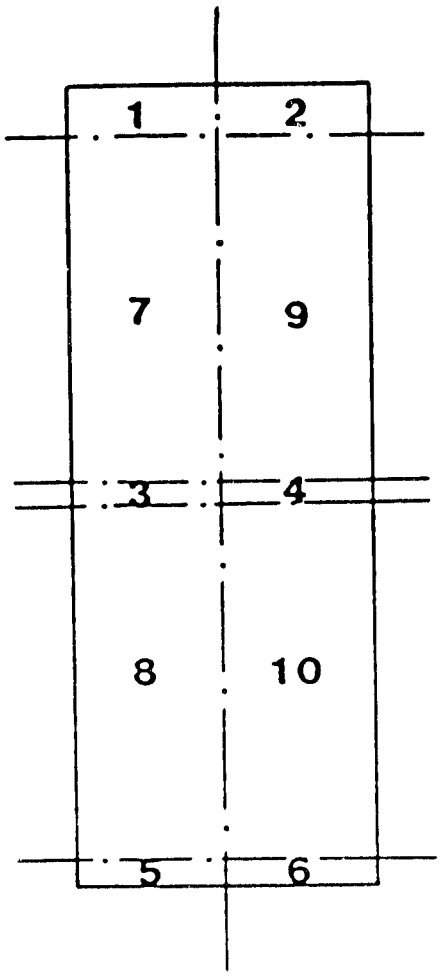


- Sections 1, 2, 5 and 6 are sectioned and used for chemical analysis.
- Section 3 is macroetched for structural analysis without HIPing.
- Section 4 is HIPed and subsequently macroetched.
- Sections 7 and 8 are HIPed and subsequently evaluated for crack propagation rate.
- Sections 9 and 10 are sectioned to about 4-5" long by 1-1.5" thick specimens for Electron Beam Melting to assess the level and the nature of the non-metallics present in the ingot.

Figure 15. Schematic diagram illustrating the sectioning mode of the VADER IN-100 ingot.

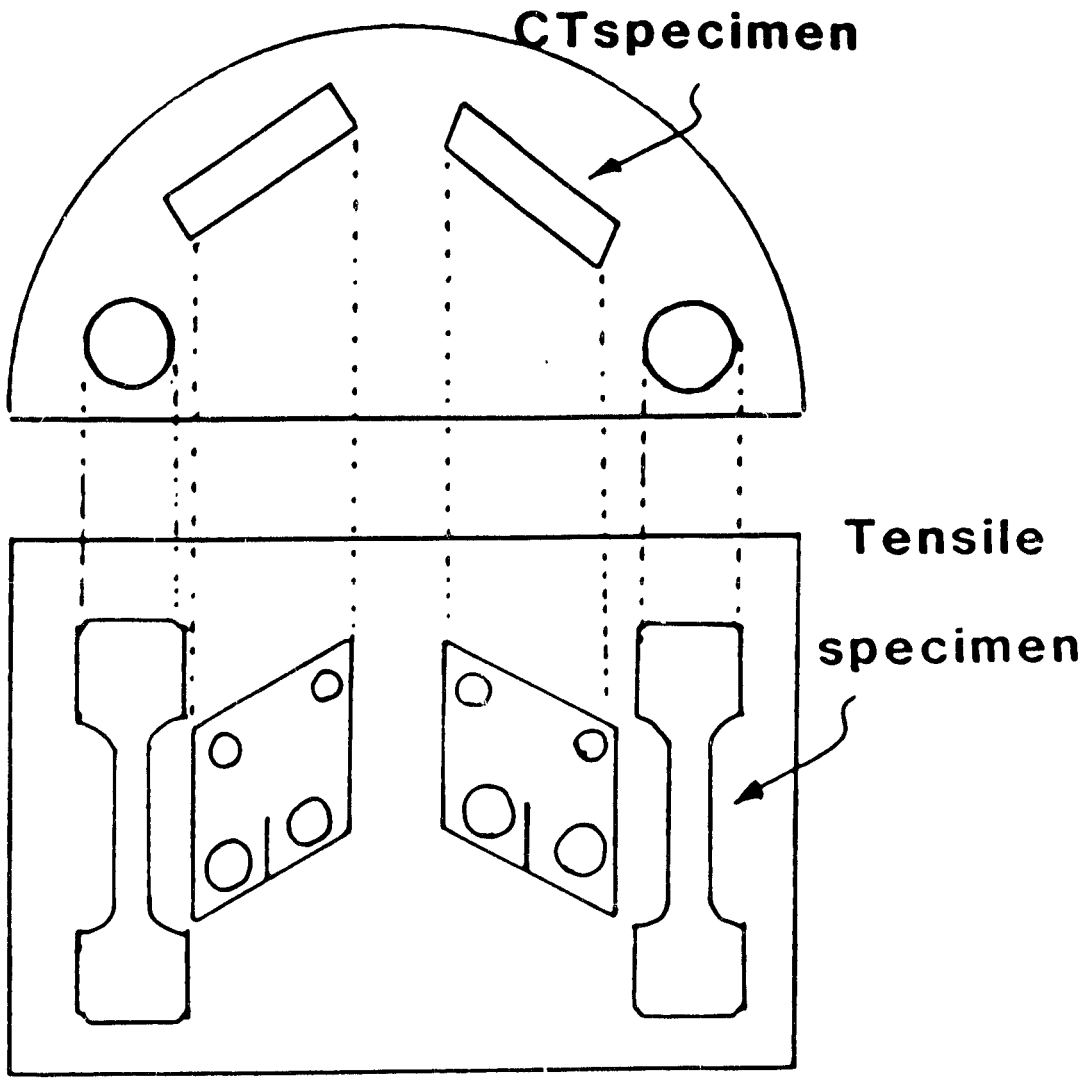


Figure 16. Specimen location for tensile properties and crack propagation studies: rheocast ingot

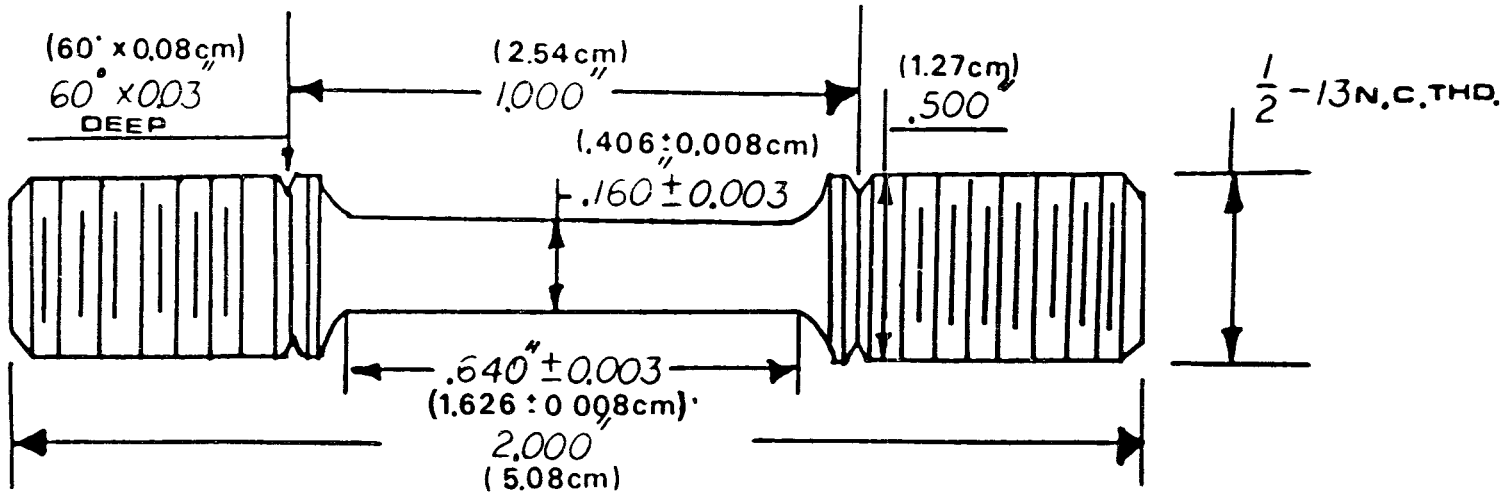


Figure 17. Schematic diagram of the tensile test specimen.

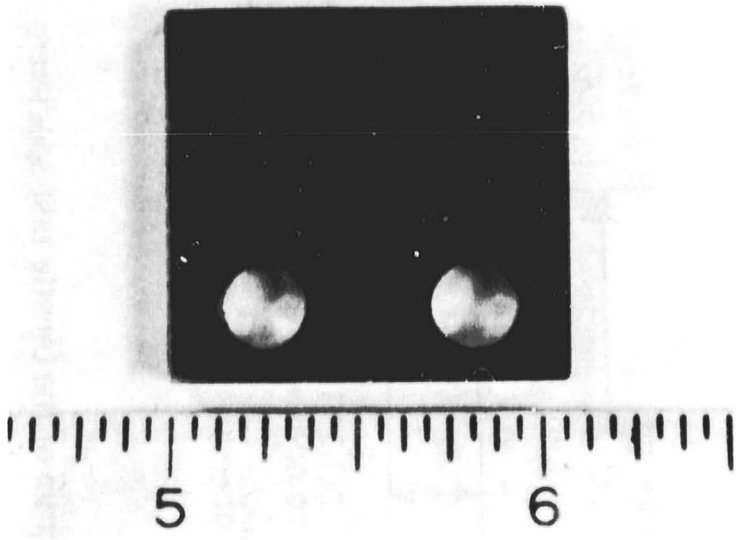


Figure 18. CT specimen for crack propagation studies.

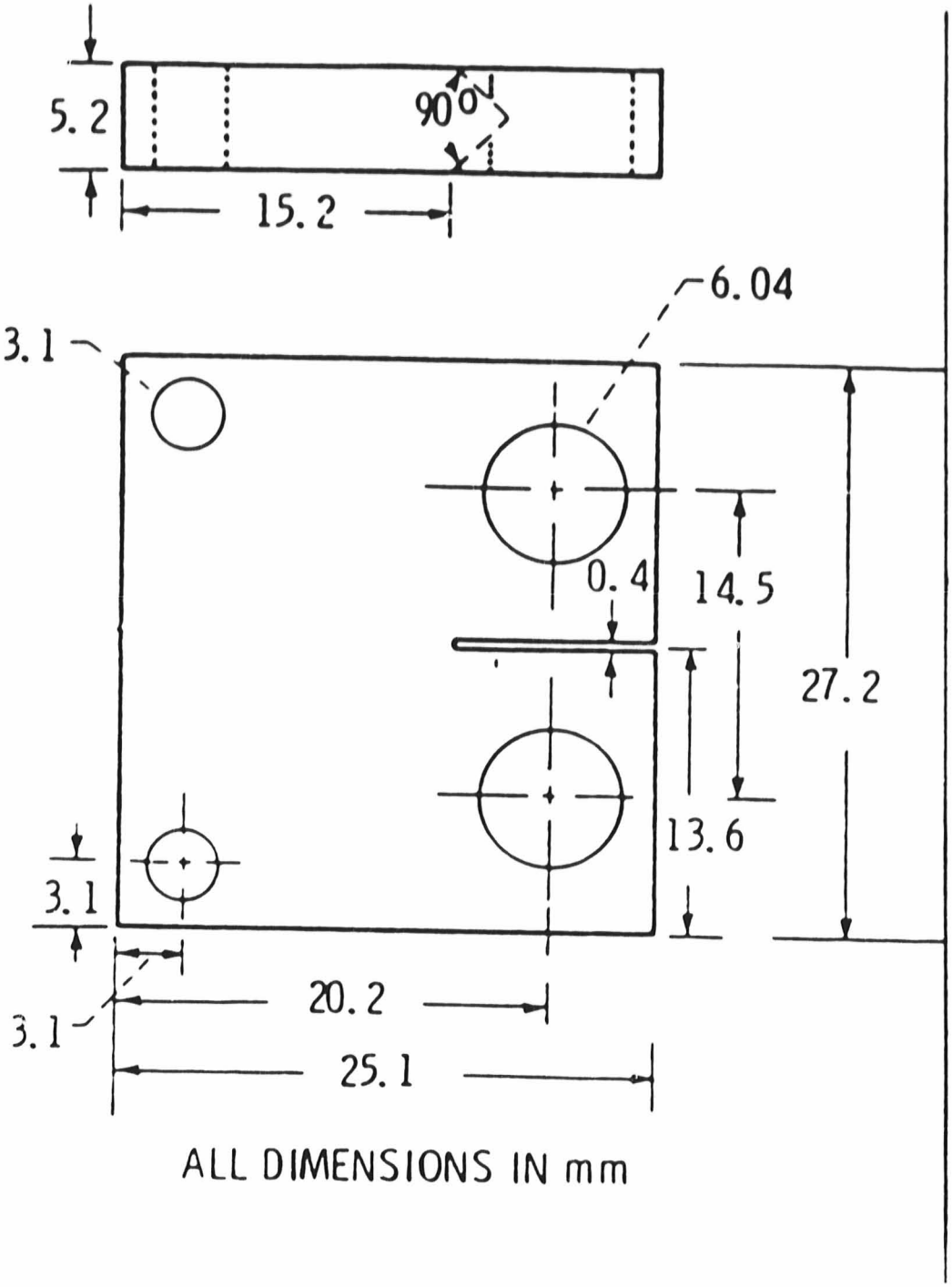


Figure 19. Design of modified CT specimen.

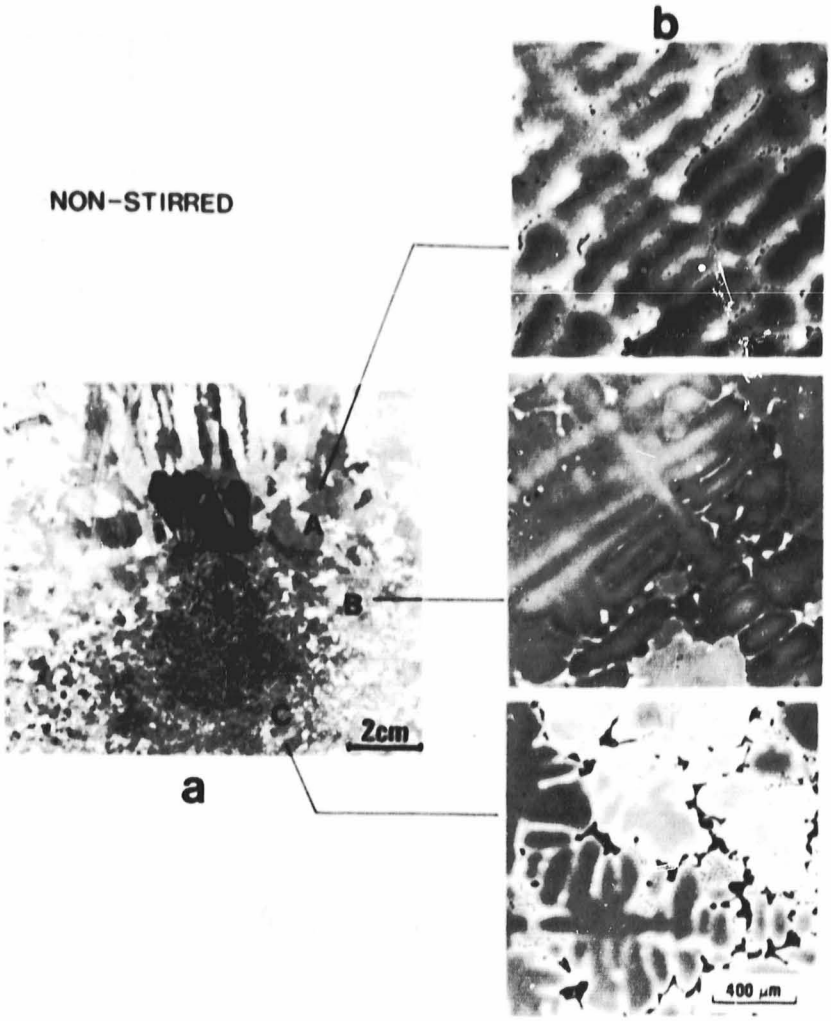


Figure 20. Photograph of non-stirred ingot: (a) macrostructure; (b) microstructures at locations A, B and C indicated in (a).

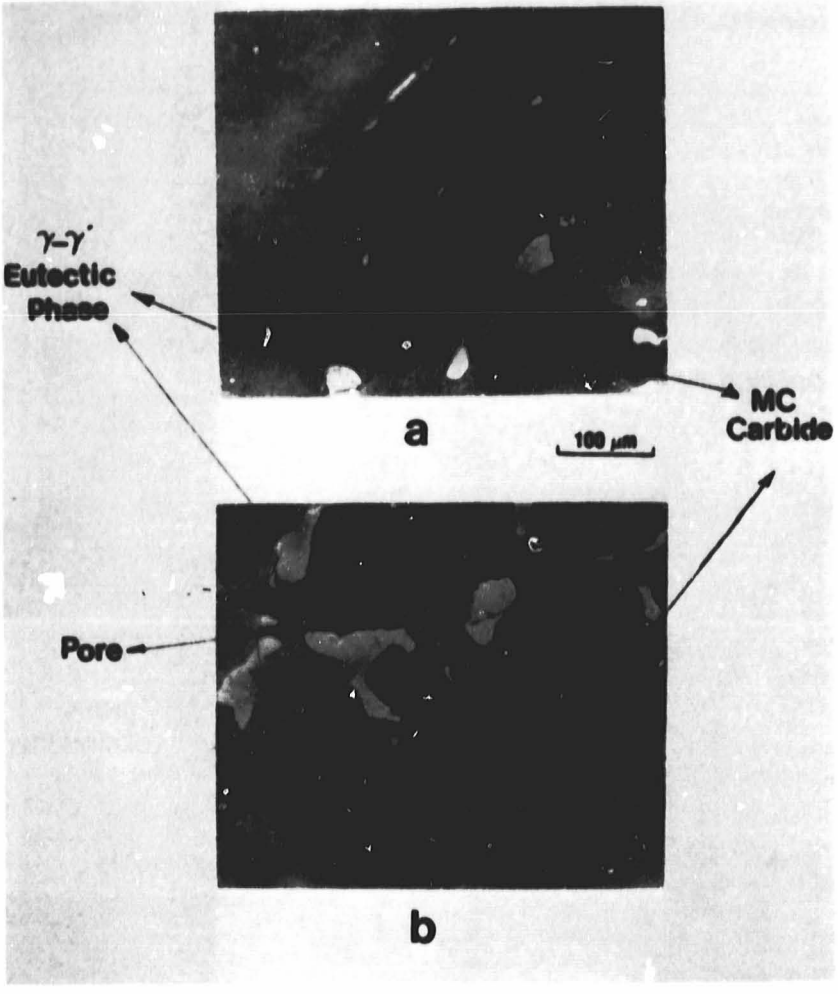


Figure 21. Representative micrographs of phases located at (a) interdendritic, (b) grain boundary in the non-stirred ingot.

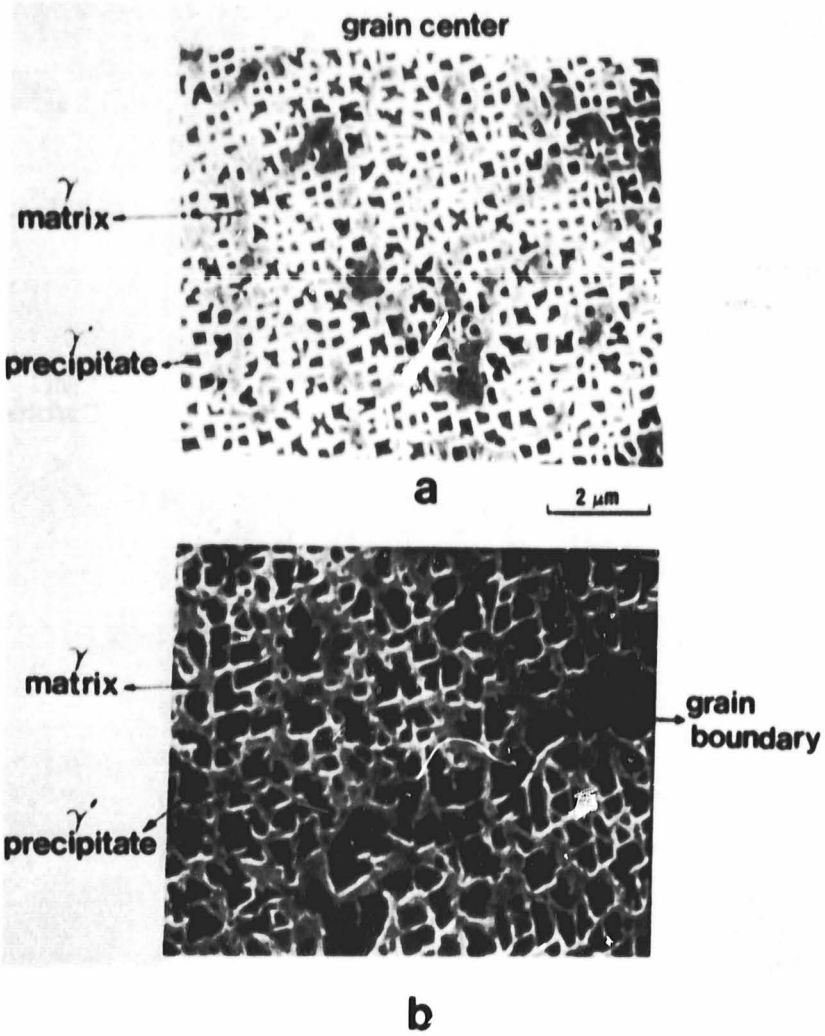


Figure 22. Representative SEM micrographs of secondary γ' precipitates in the non-stirred ingot. (a) at the center of the dendrite arm; (b) near the inter-dendritic region.

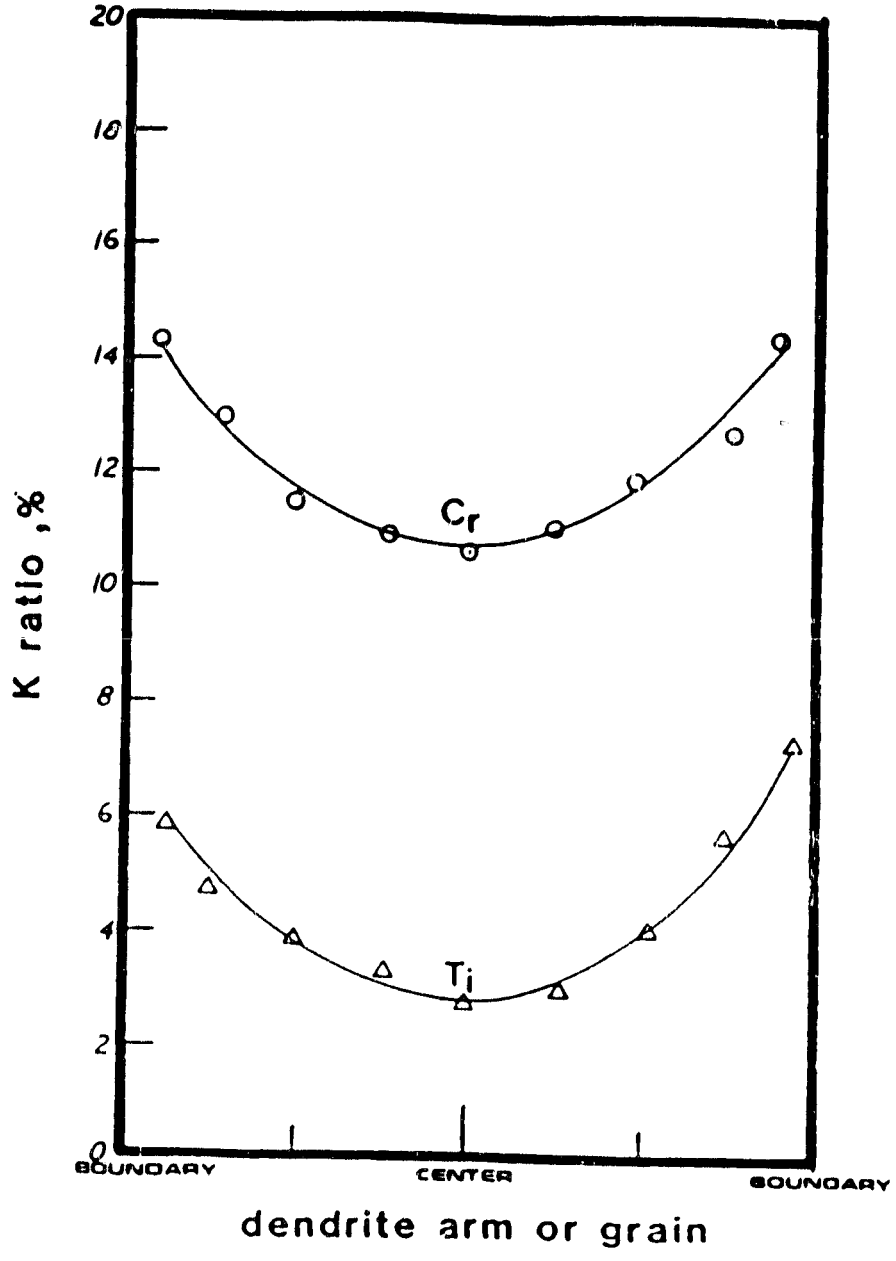


Figure 23. Ti and Cr concentration profiles in the dendrite arm of non-stirred ingot.

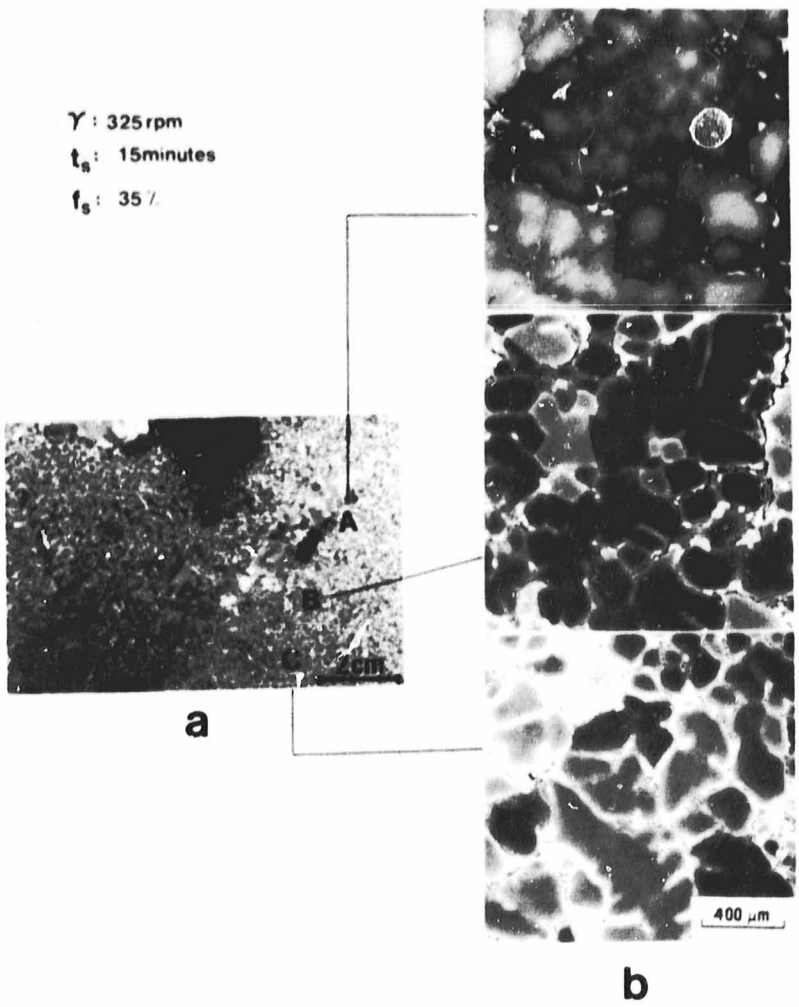


Figure 24. Photographs of rheocast ingot stirred at $\gamma$ = 325 rpm, $t_s$ = 15 minutes and fs = 35%. (a) macrostructure; (b) microstructures at locations A, B and C indicated in (a).

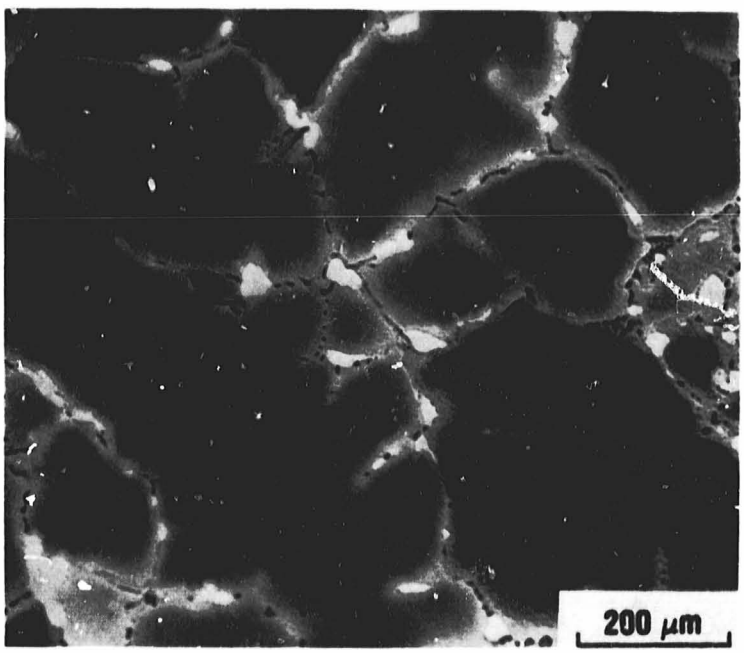


Figure 25. Microstructure in region C of Figure 24 (b) at a high magnification.

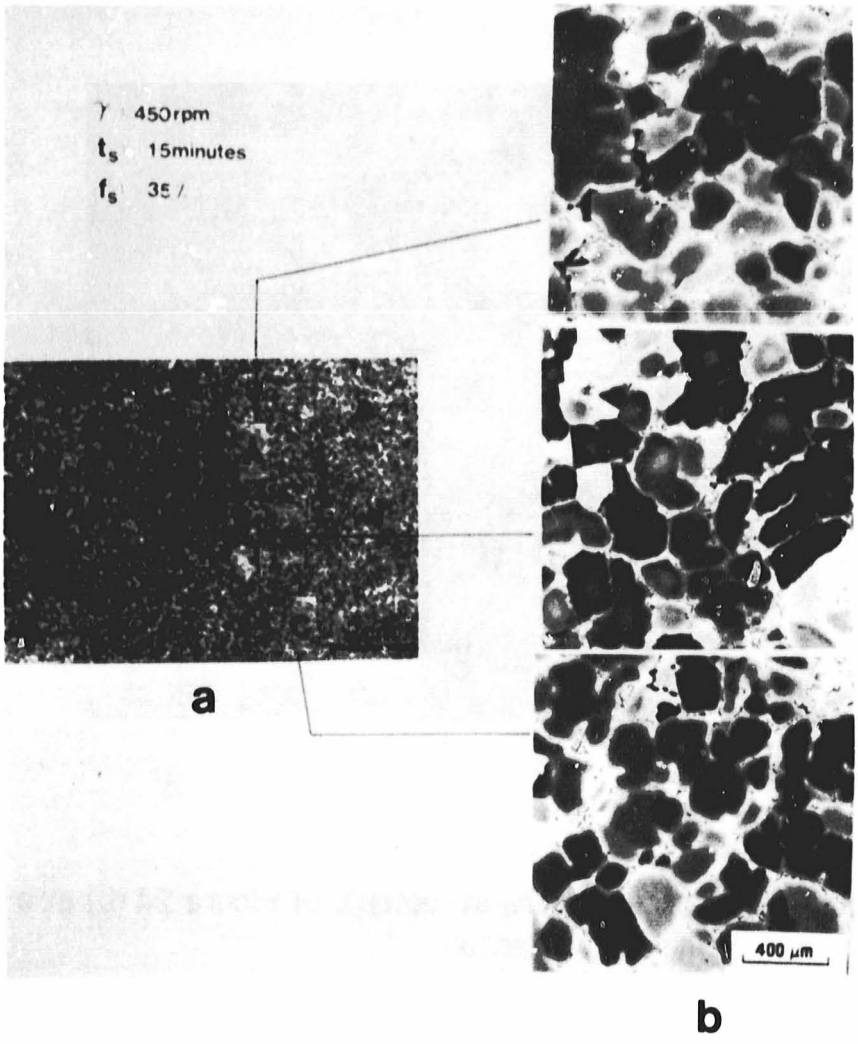


Figure 26. Photographs of rheocast ingot stirred at $\gamma$ = 450 rpm, $t_s$ = 15 minutes and fs = 35%. (a) macrostructure; (b) microstructures at locations A, B and C indicated in (a).

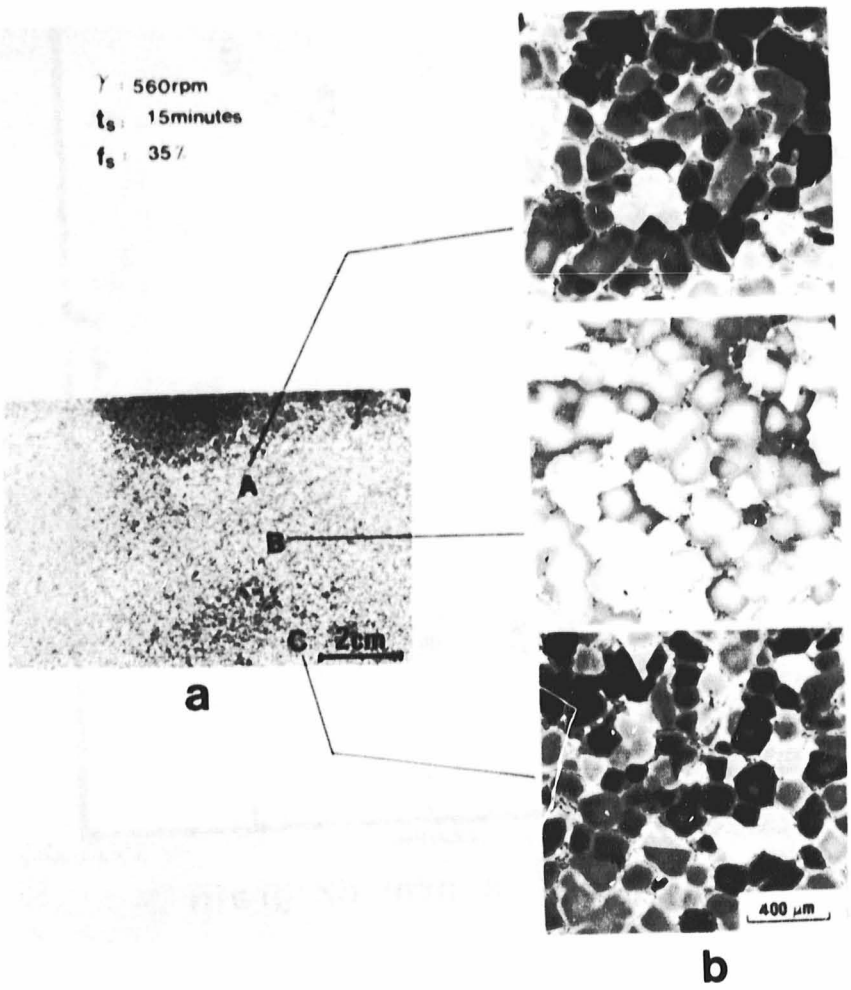


Figure 27. Photographs of rheocast ingot stirred at $\gamma$ = 560 rpm, $t_s$ = 15 minutes and fs = 35%. (a) macrostructures; (b) microstructures at locations A, B and C indicated in (a).

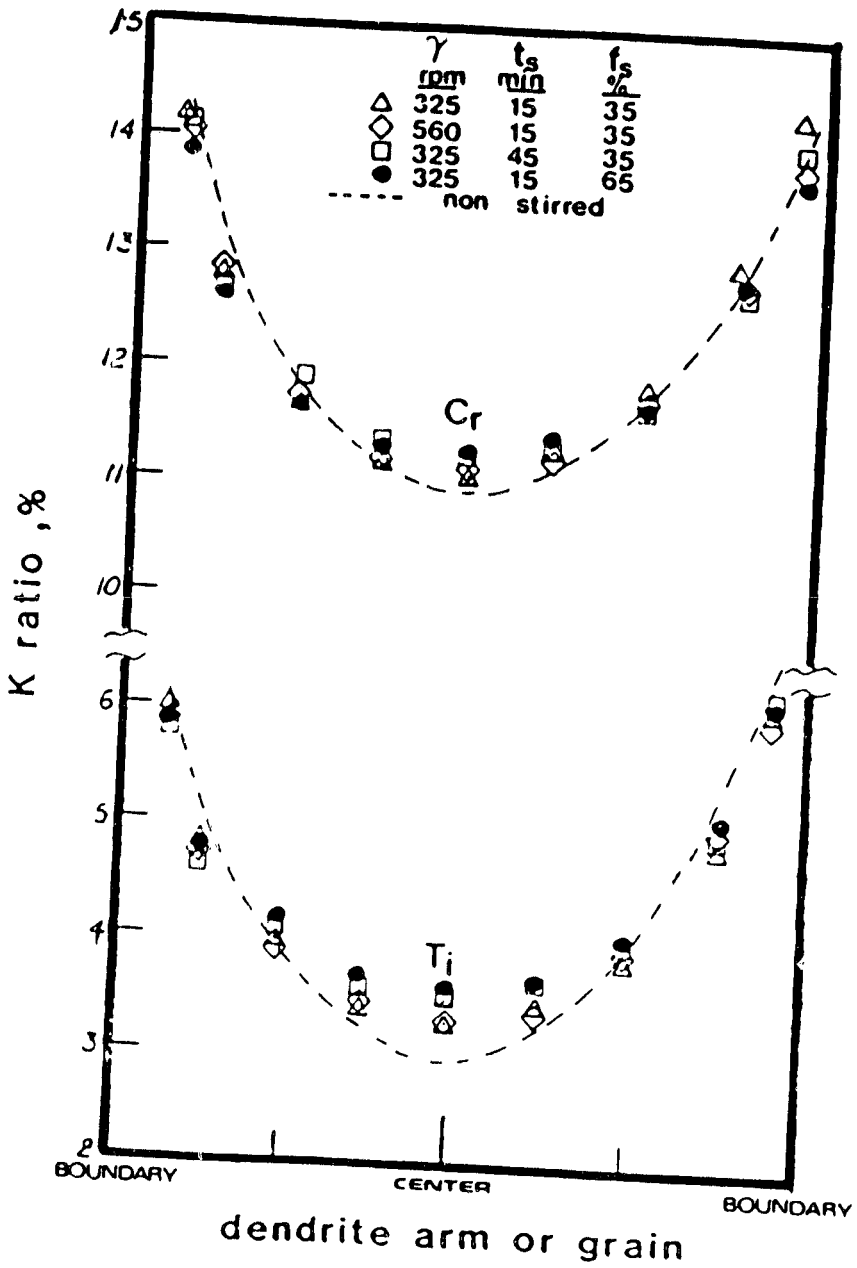


Figure 28. Ti and Cr concentration profiles as a function of processing variables in rheocast microstructures.

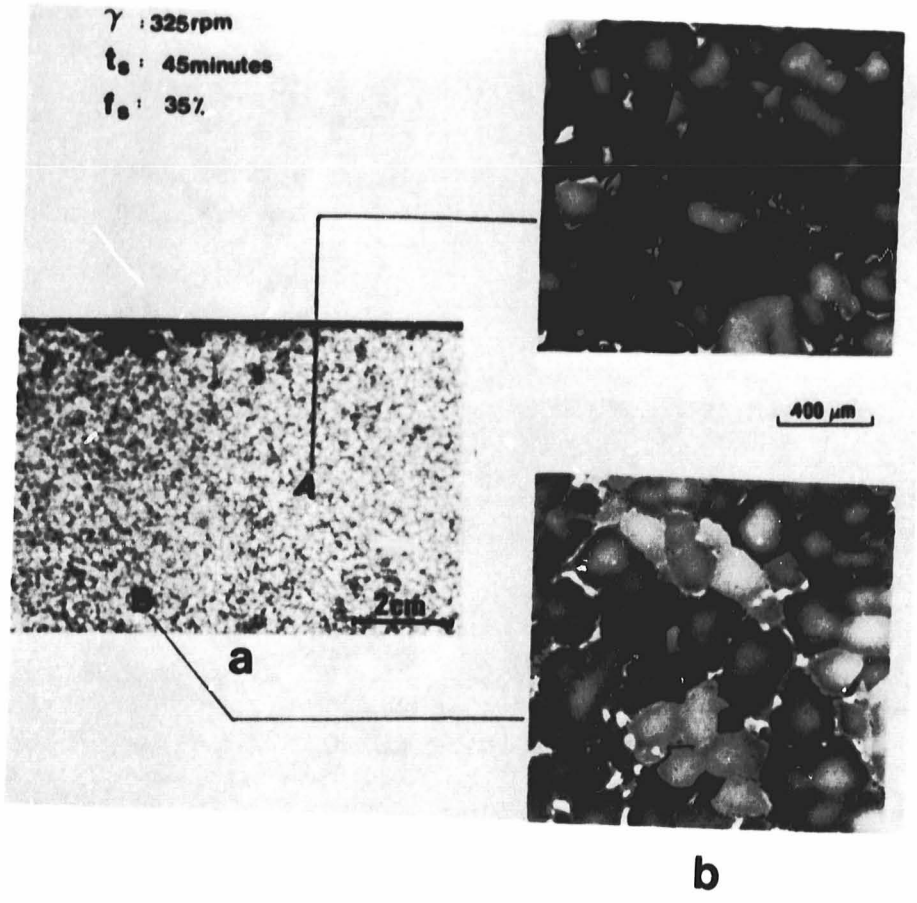


Figure 29. Photographs of rheocast ingot stirred at $\gamma$ = 325 rpm, $t_s$ = 45 minutes and fs = 35%. (a) macrostructure; (b) microstructures at locations A and B indicated in (a).

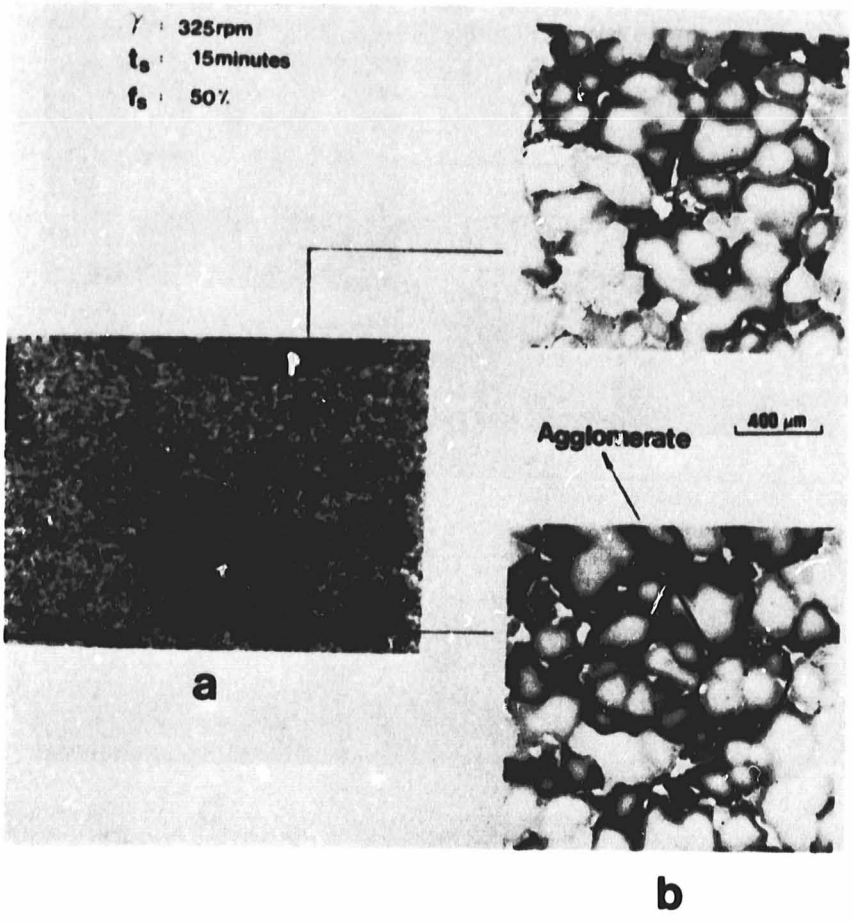


Figure 30. Photographs of rheocast ingot stirred at $\gamma$ = 325 rpm, $t_s$ = 15 minutes and fs = 50%. (a) macro-strucutre; (b) microstructures at locations A and B indicated in (a).

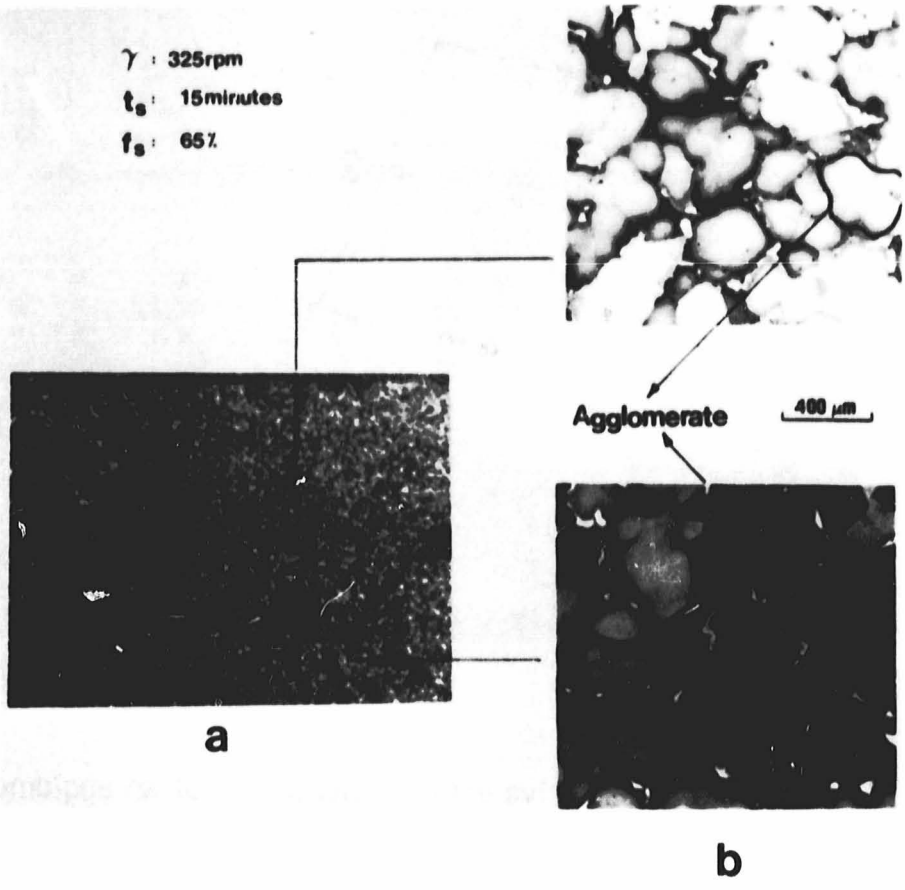


Figure 31. Photographs of rheocast ingot stirred at $\gamma$ = 325 rpm, $t_s$ = 15 minutes and fs = 65%. (a) macro-structure; (b) microstructures at locations A and B indicated in (a).

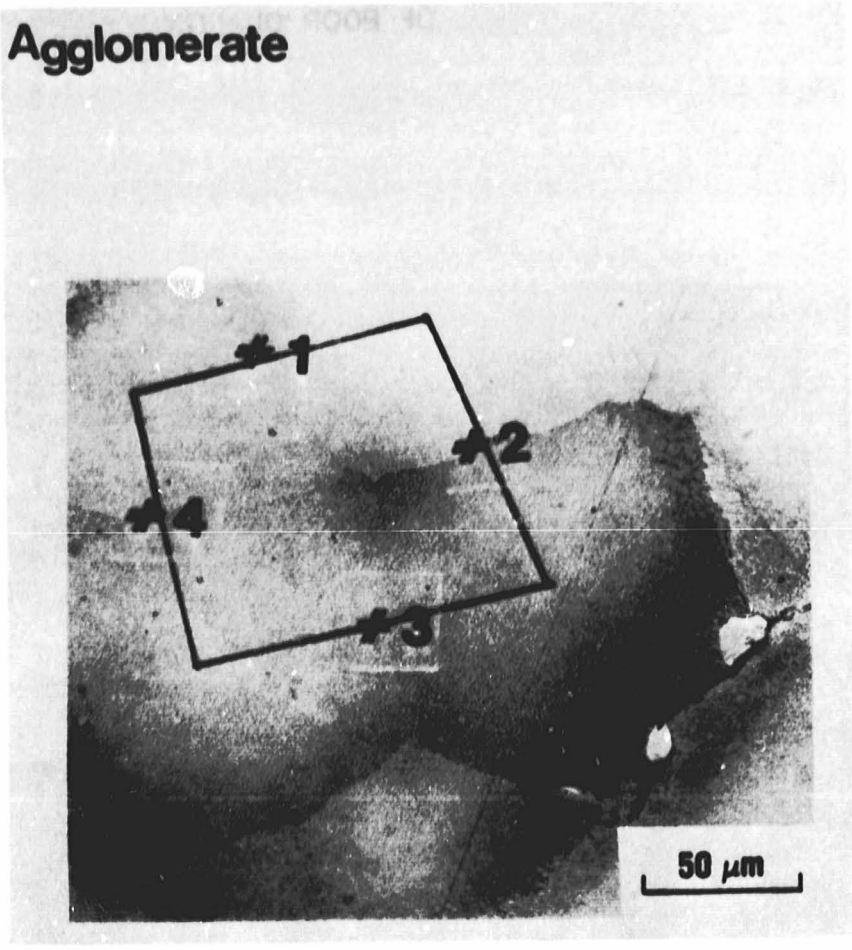


Figure 32. Representative optical micrograph of an agglomerate at high magnification.

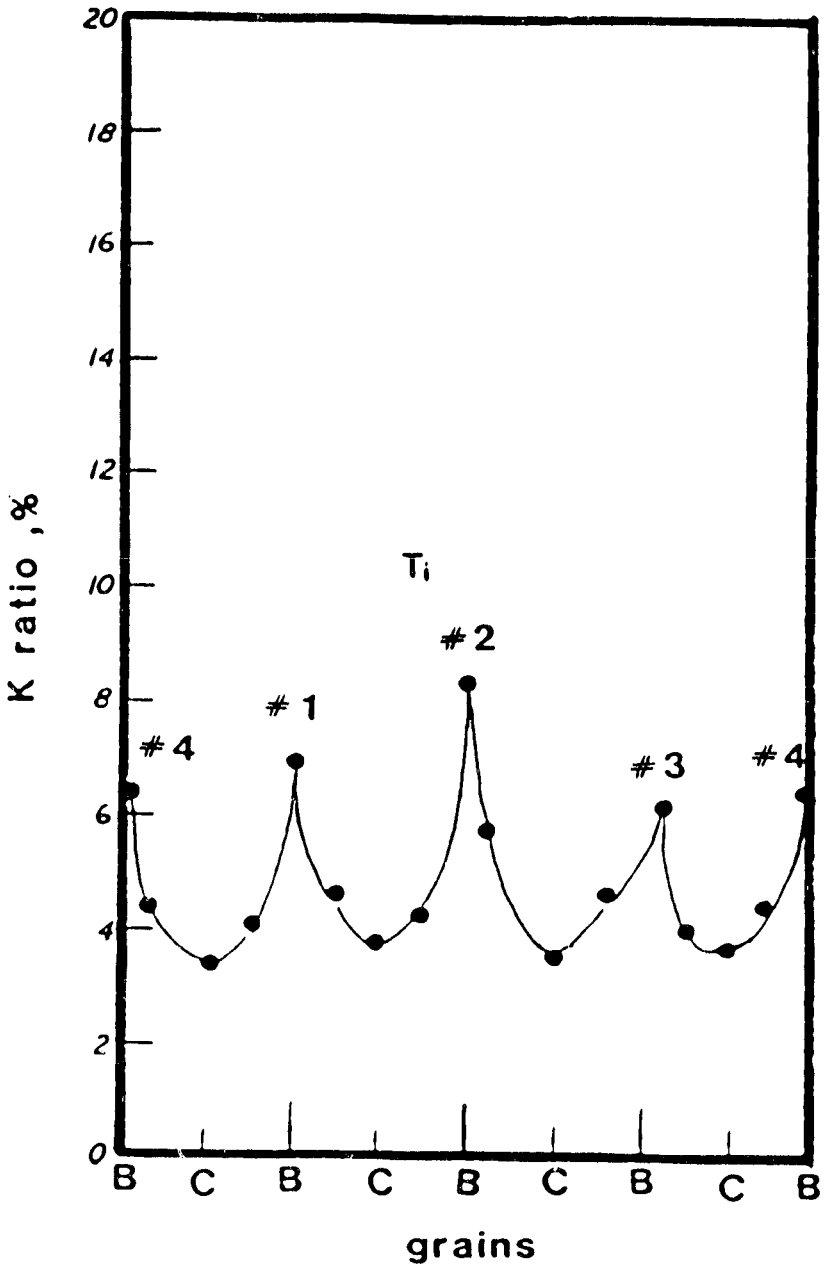


Figure 33. Ti concentration profile across grain boundaries #1, #2, #3 and #4 indicated in Figure 32.

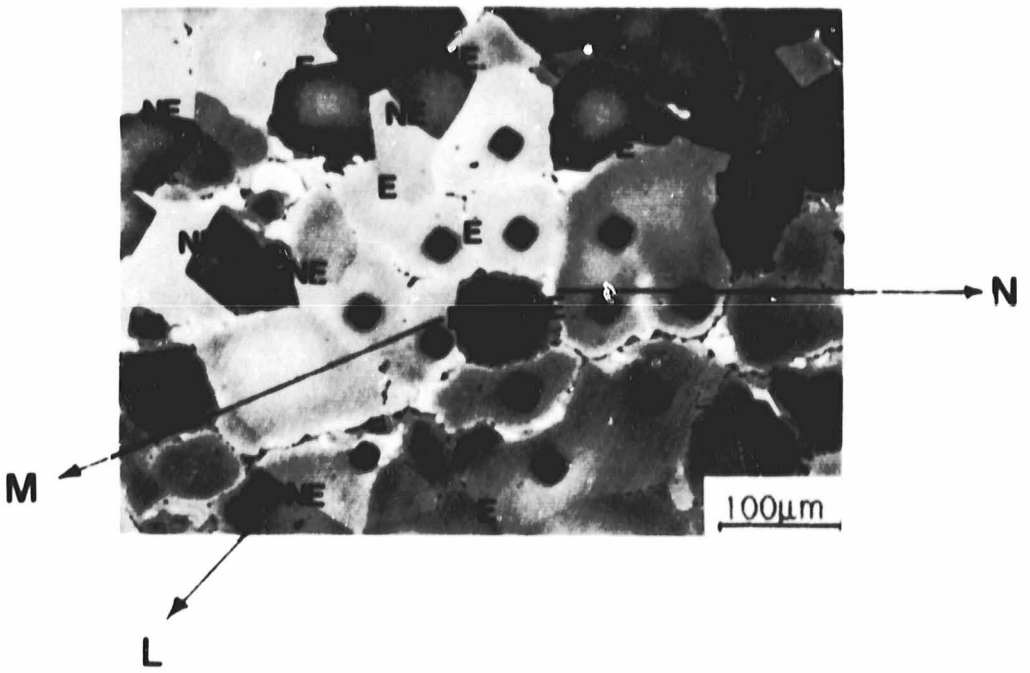


Figure 34. Representative microstructure of rheocast ingots.
E: Ti enriched; NE: not Ti enriched.

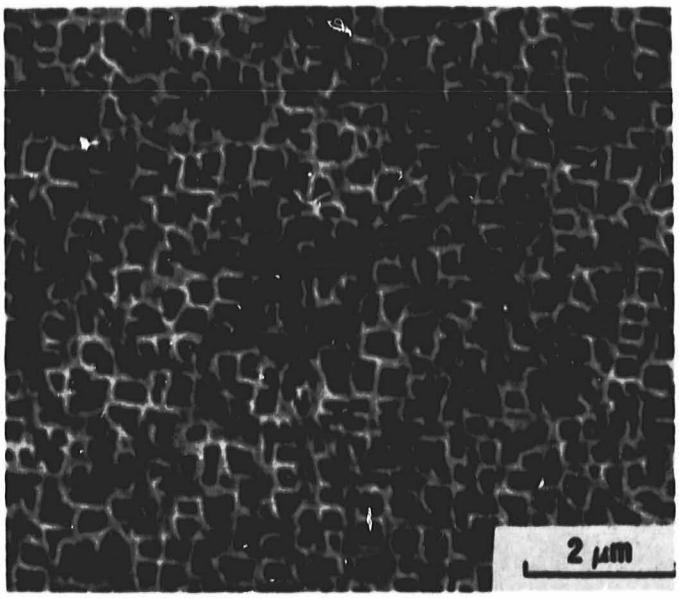


Figure 35. Representative SEM micrograph of the secondary precipitated γ' at the grain center.

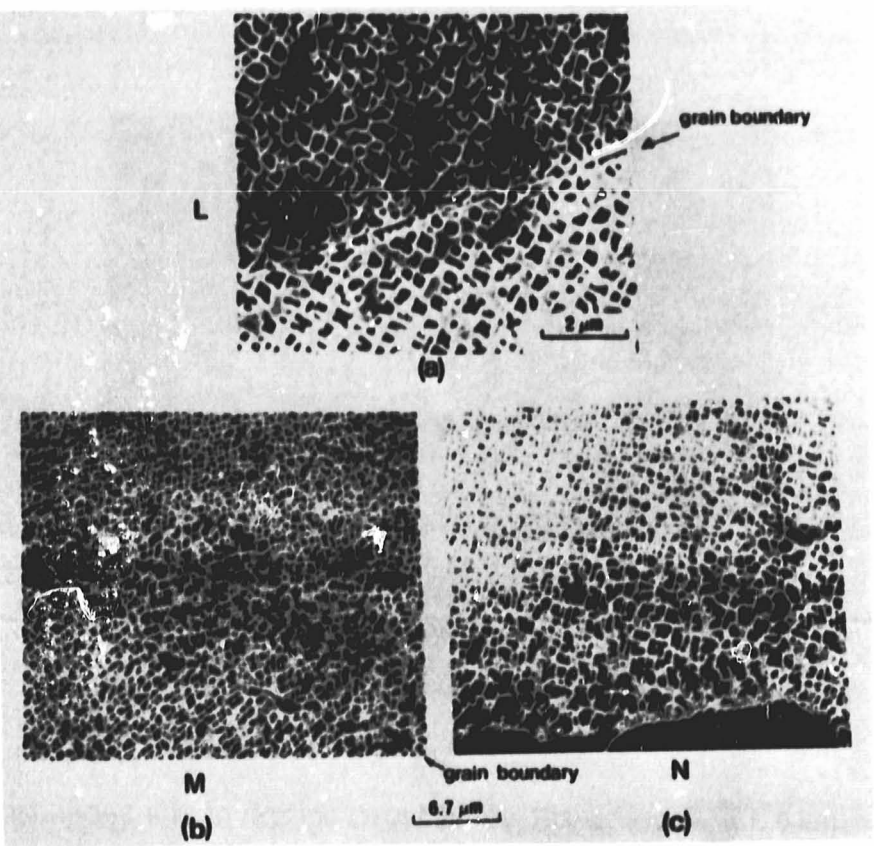


Figure 36. SEM micrographs of grain boundaries located at (a) L, (b) M and (c) N in Figure 34.

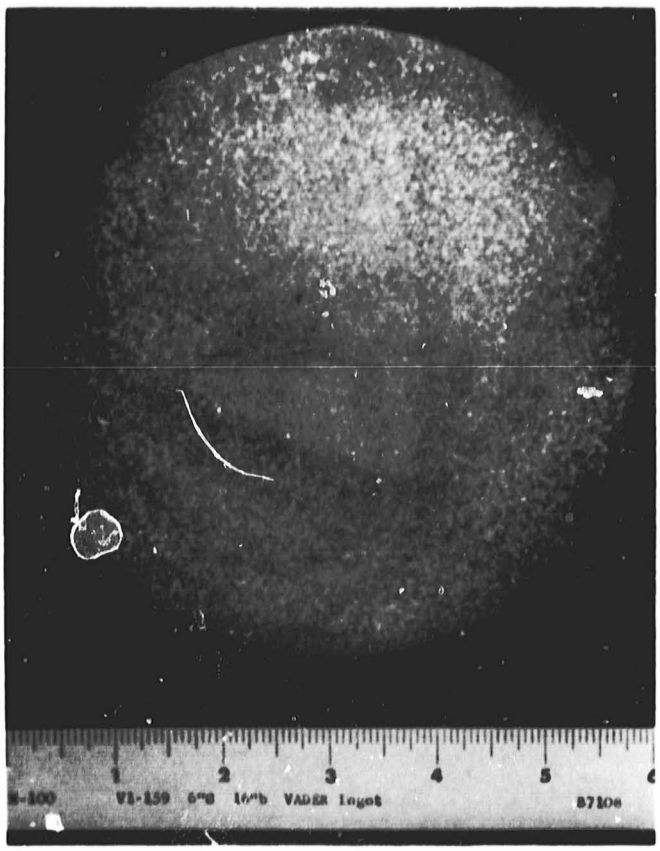


Figure 37. Macrostructure of VADER processed iN-100.

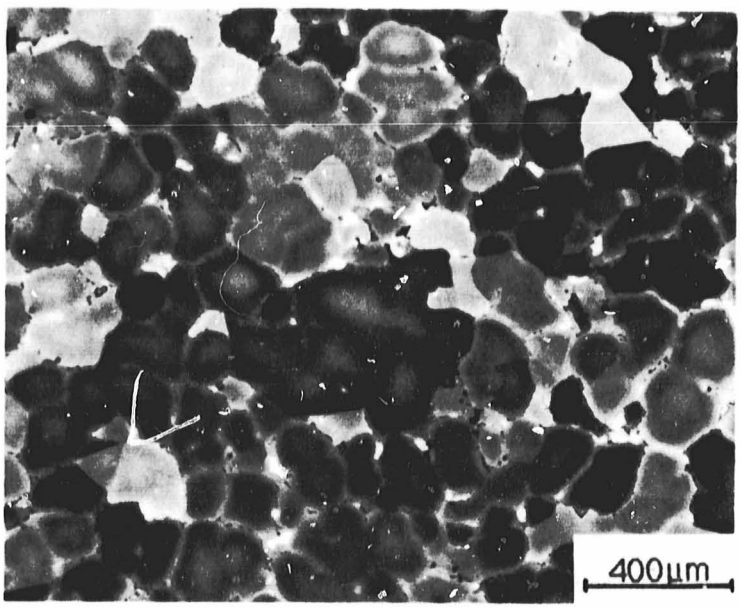


Figure 38. Representative microstructure of VADER processed IN-100.

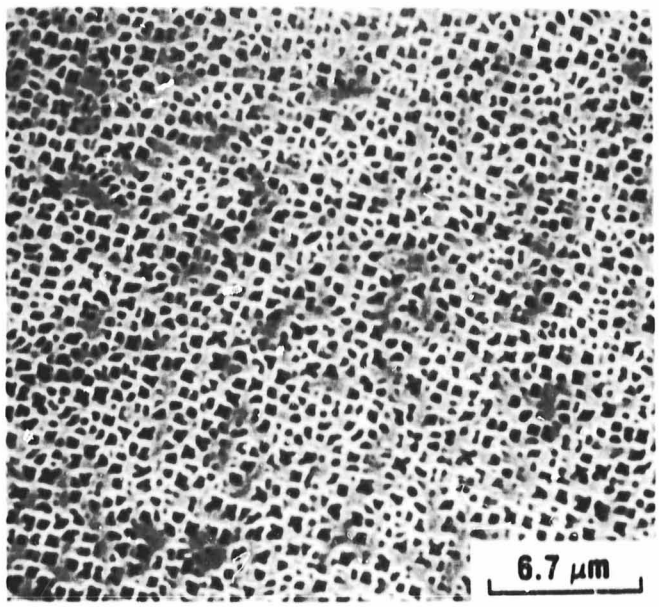


a

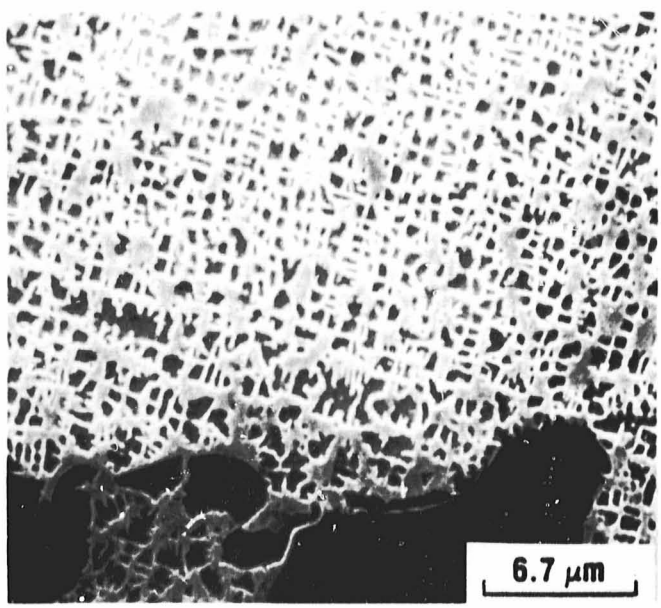


b

Figure 39. Represetnative SEM micrographs of secondary precipitated γ' in the VADER ingot, (a) at the grain center; (b) near the grain boundary.

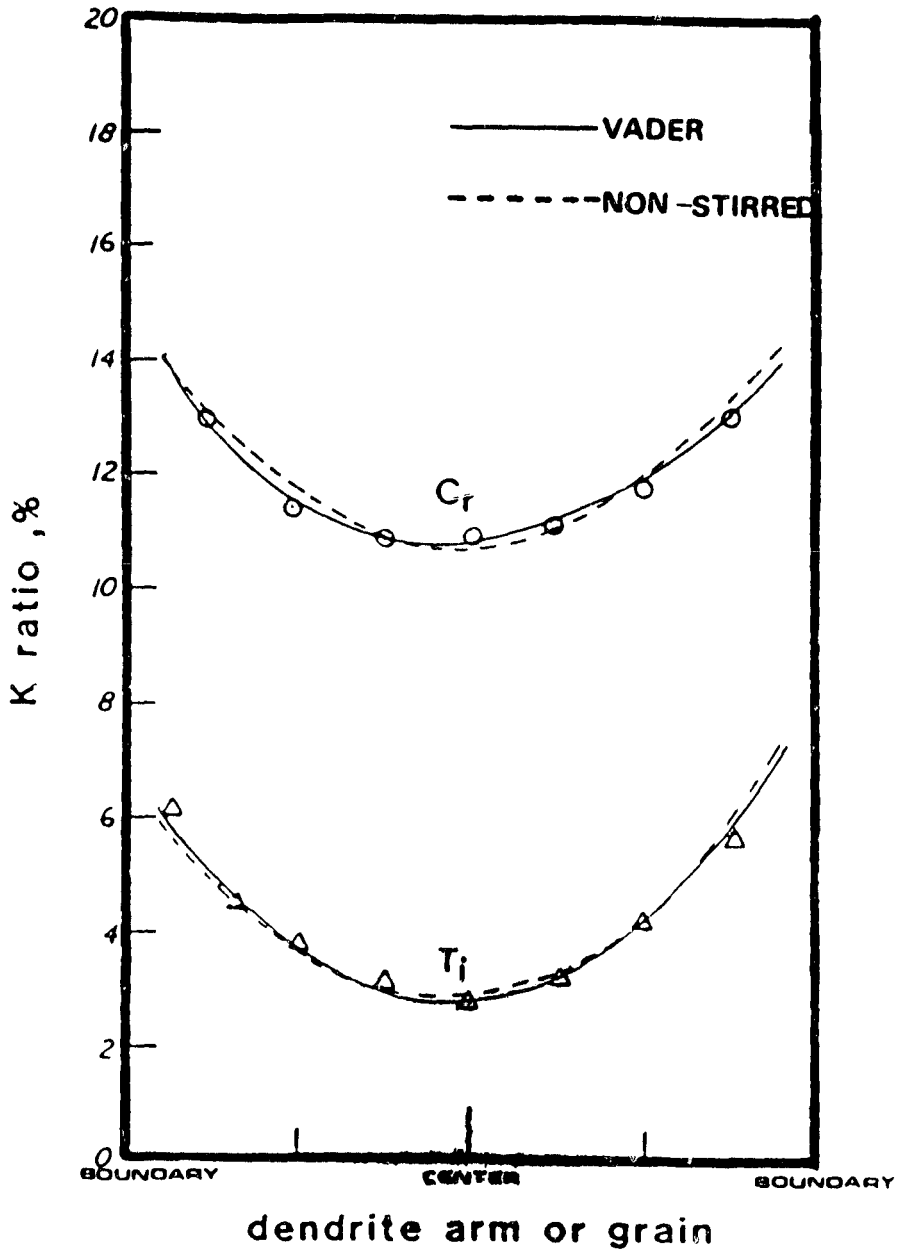


Figure 40. Ti and Cr concentration profiles in the grain of the VADER ingot.

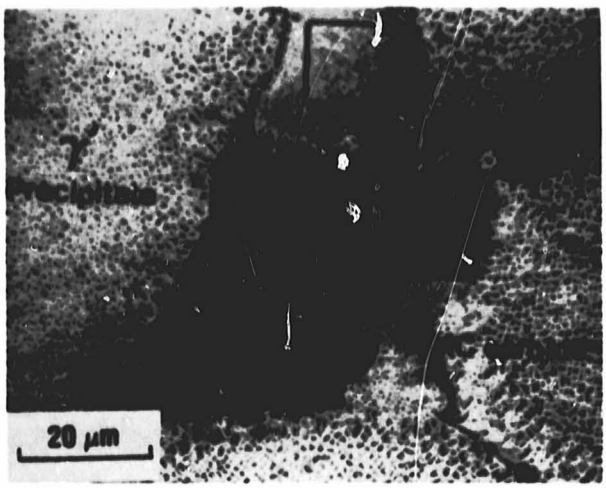


a

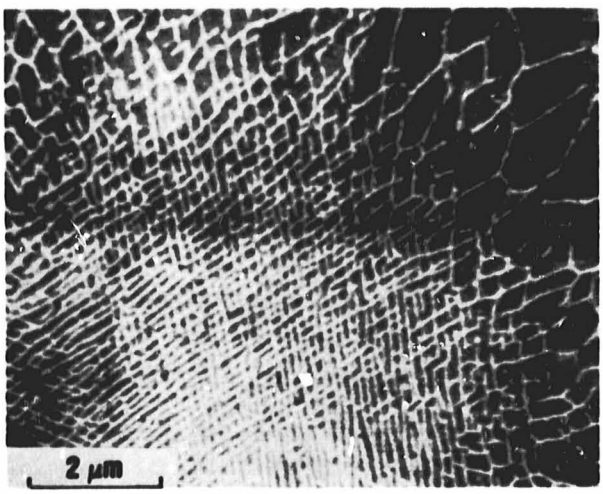


b

Figure 41. Representative SEM micrograph of (a) grain boundary phases and (b) γ-γ' network in the γ-γ' eutectic island in all the as-cast ingots.

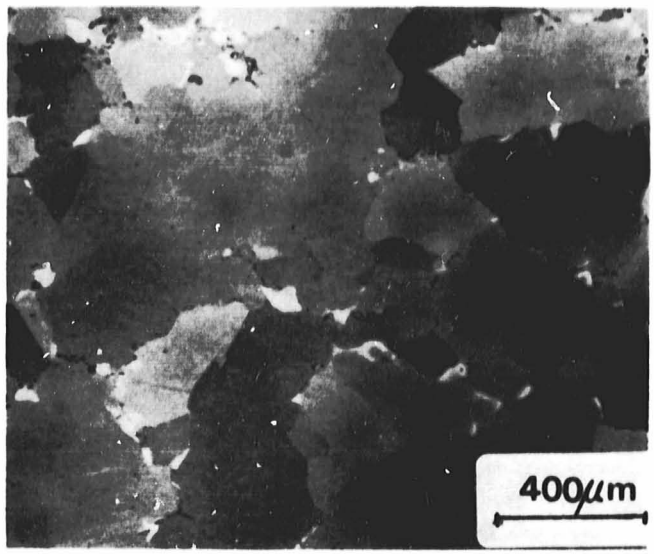


Figure 42. Representative microstructure of the rheocast ingot (stirred at y = 325 rpm, $t_s$ = 15 minutes and fs = 35%) after HIP.

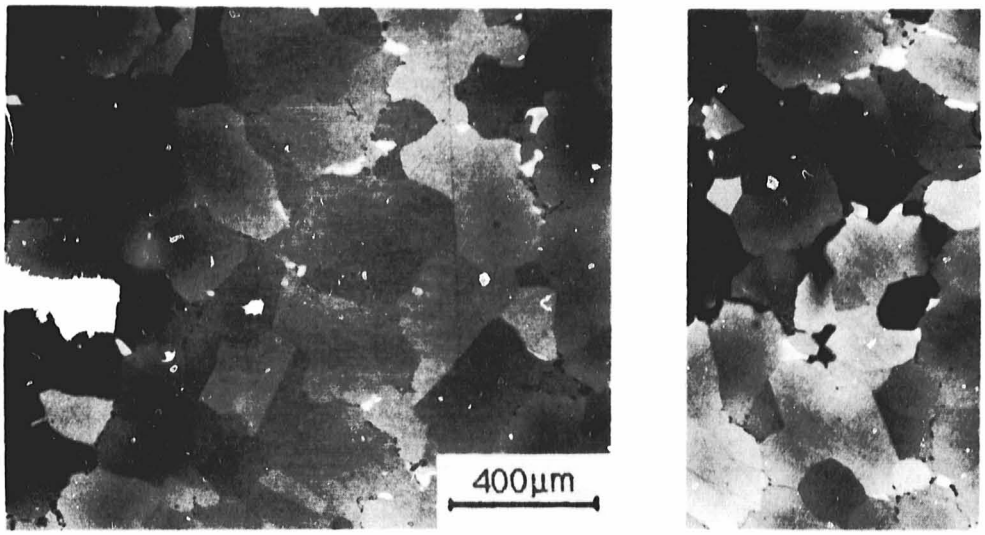


a b

Figure 43. (a) Microstrucutre, (b) pore region of the rheocast ingot (stirred at y = 560 rpm, $t_s$ = 15 minutes and fs = 35%) after HIP.

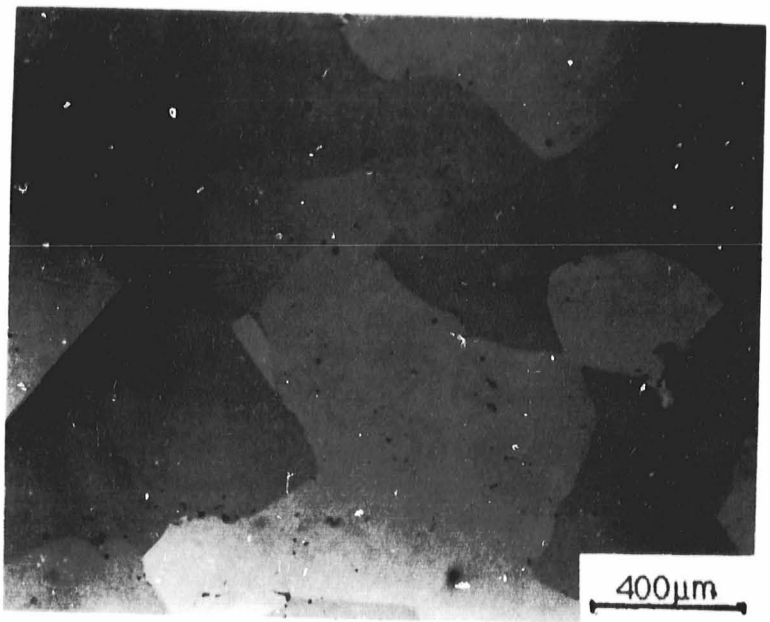


Figure 44. Representative microstructure of the VADER ingot after HIP.

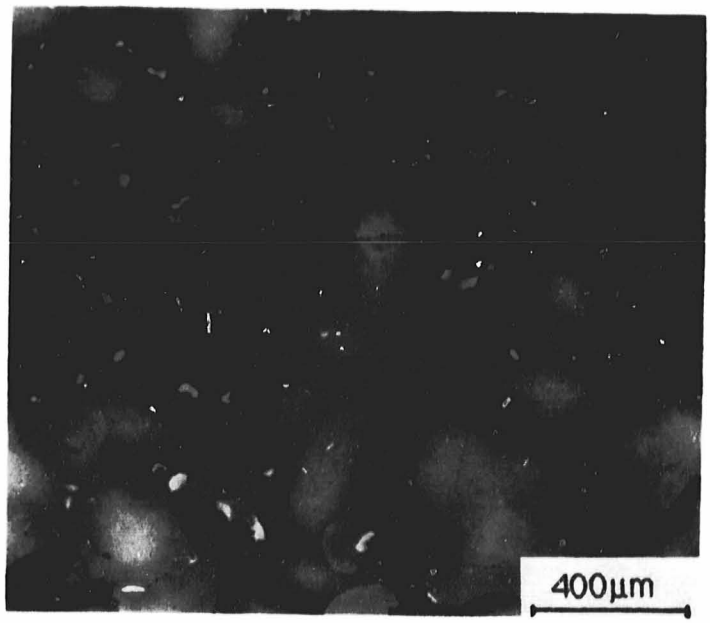


Figure 45. Representative microstructure of the non-stirred ingot after HIP and heat treating.

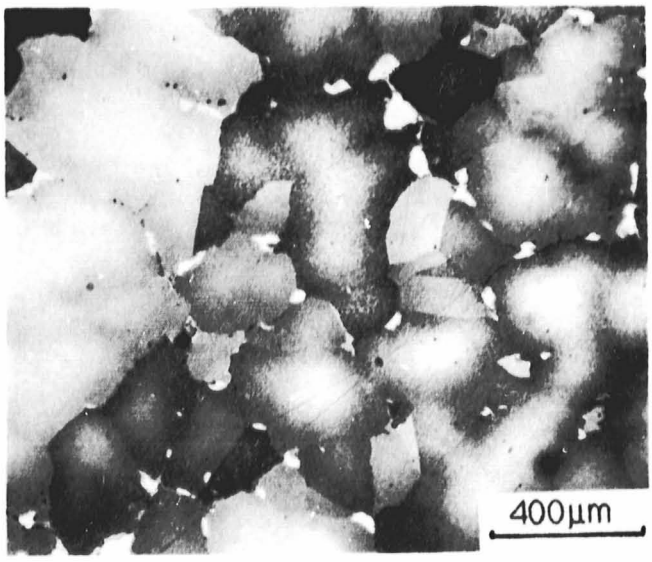


Figure 46. Representative microstructure of the rheocast ingot (stirred at $\gamma$ = 325 rpm, $t_s$ = 15 minutes and fs = 35%) after HIP and heat treating.

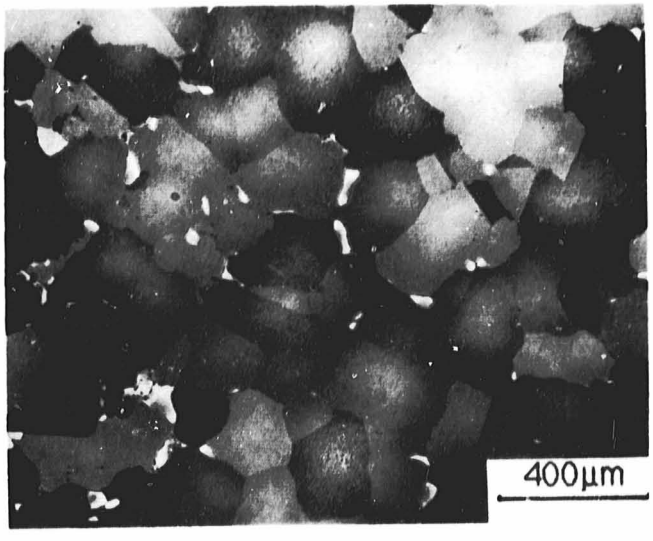


Figure 47. Represetnative microstructure of the rheocast ingot (stirred at $\gamma$ = 560 rpm, $t_s$ = 15 minutes and fs = 35%) after HIP and heat treating.

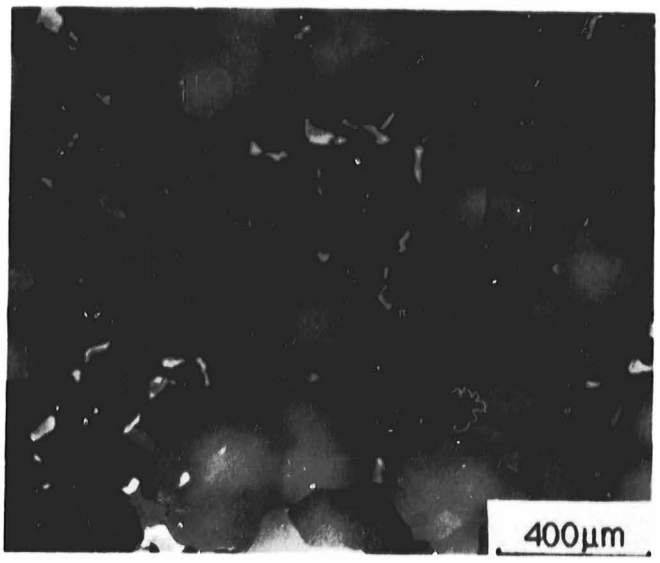


Figure 48. Representative microstructure of the rheocast ingot (stirred at $\gamma$ = 325 rpm, $t_s$ = 45 minutes and fs = 35%) after HIP and heat treating.

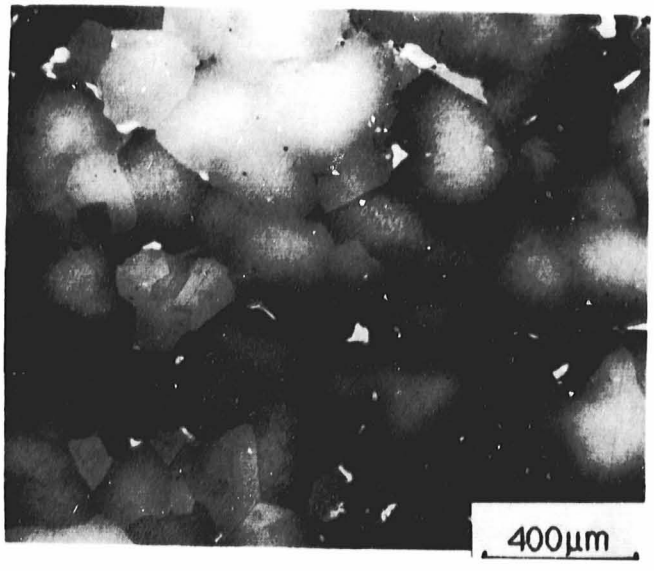


Figure 49. Representative microstructure of the rheocast ingot (stirred at $\gamma$ = 325 rpm, $t_s$ = 15 minutes and fs = 65%) after HIP and heat treating.

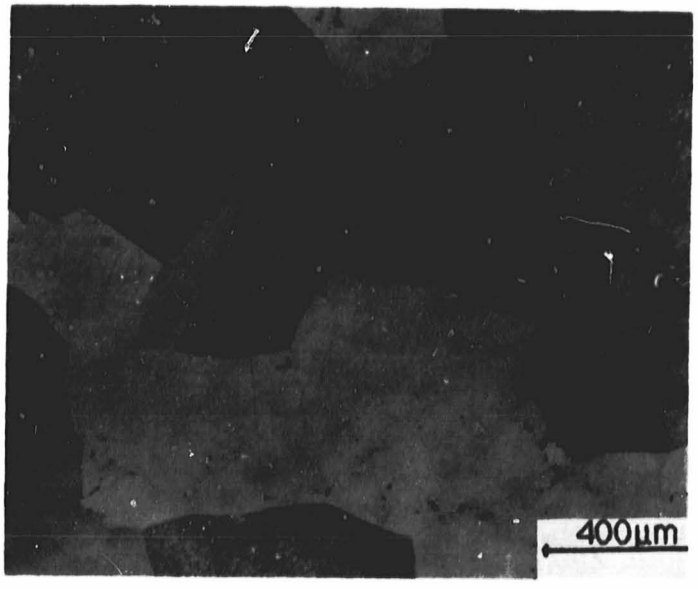


Figure 50. Representative microstructure of the VADER ingot after HIP and heat treating.

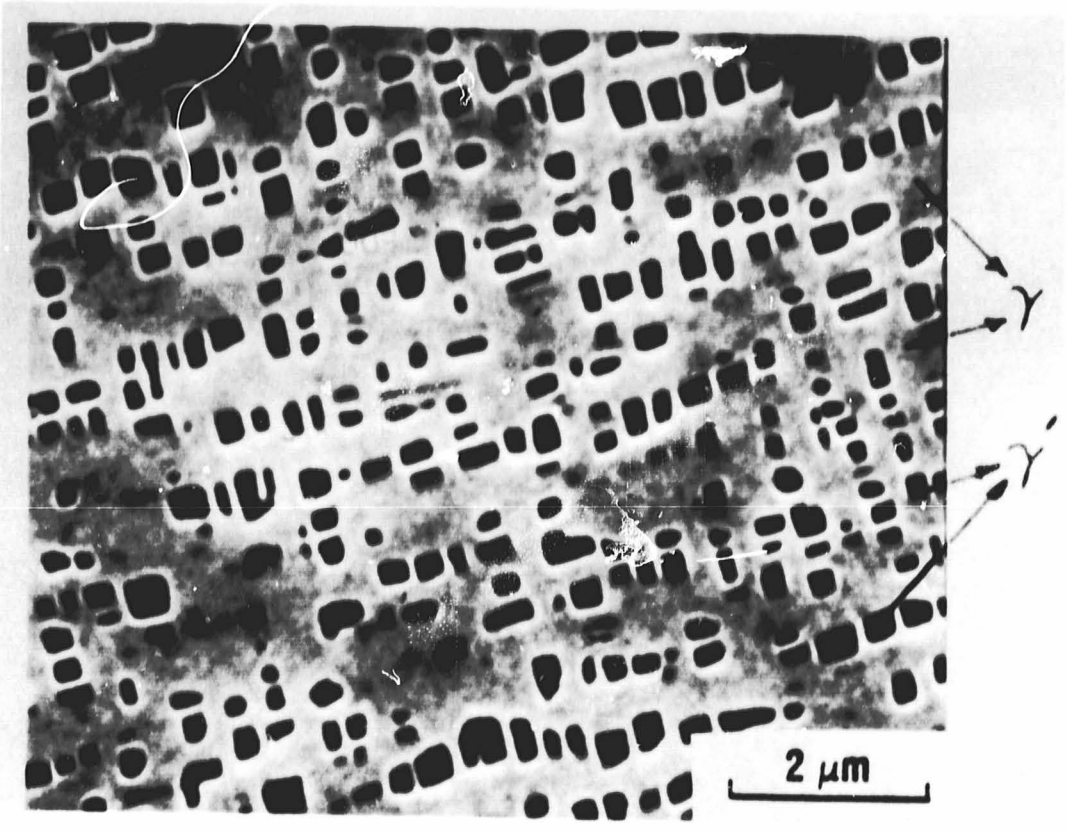


Figure 51. Representative SEM micrograph of the secondary precipitated γ' at the grain center after HIP and heat treating.

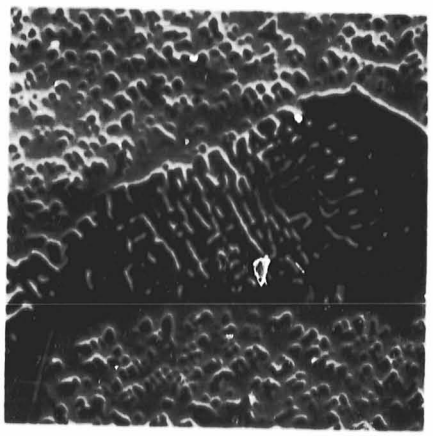

eutectic

*MC carbide

(a)

6.7 μm

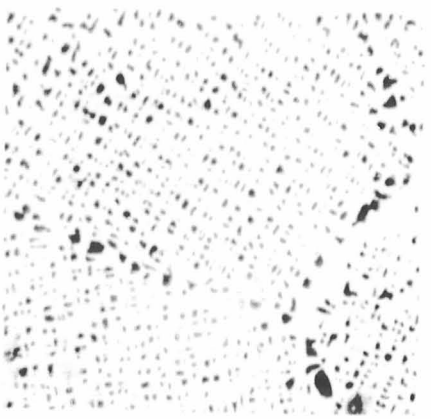

grain boundary

(b)

Figure 52. Representative SEM micrograph of the secondary precipitated γ' near the grain boundaries of (a) non-stirred or rheocast ingots, (b) VADER ingot after HIP and heat treating.

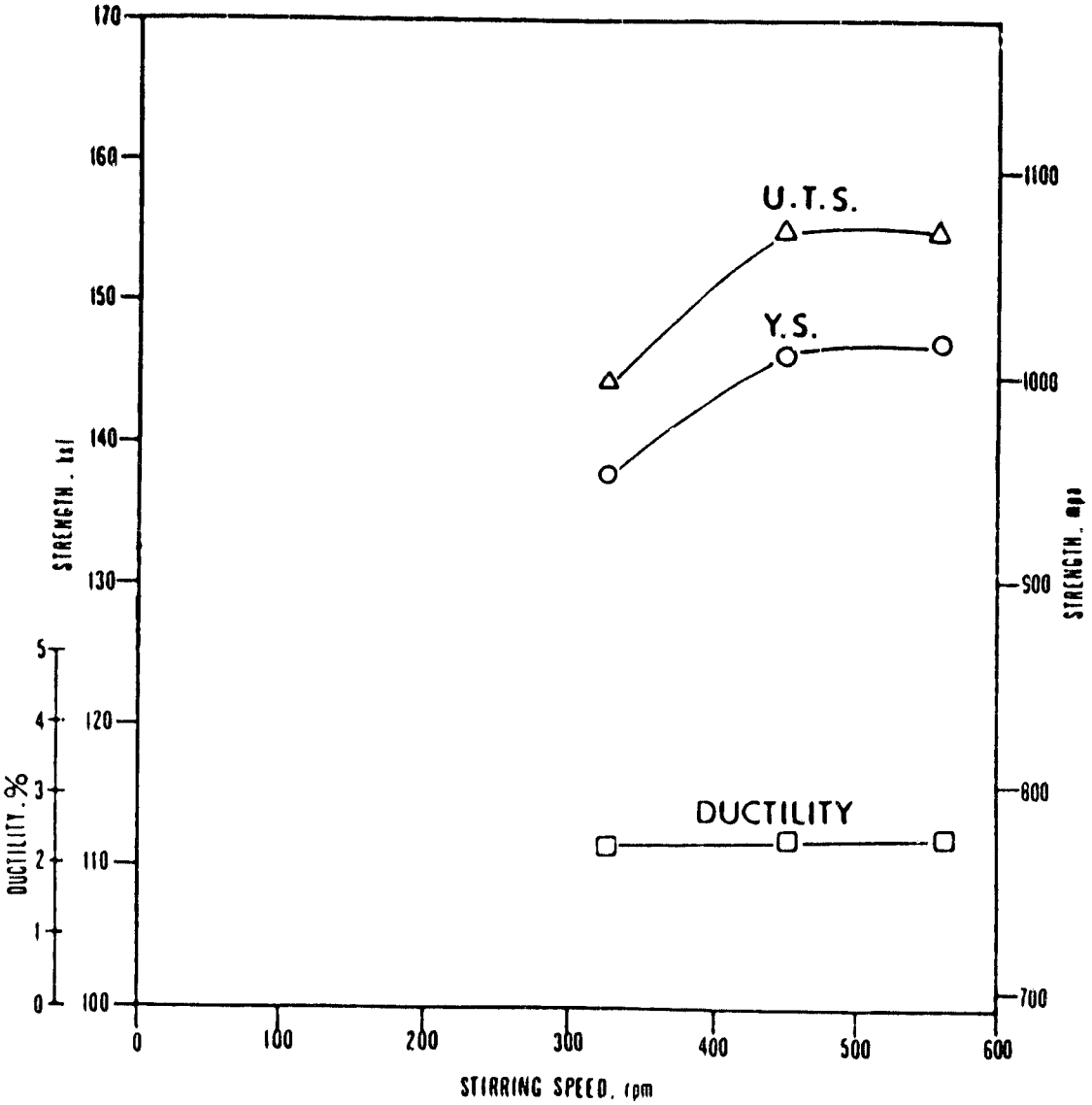


Figure 53. Tensile properties versus stirring speed at 650°C in air - at a constant isothermal stirring time (15 minutes) and volume fraction solid (35%).

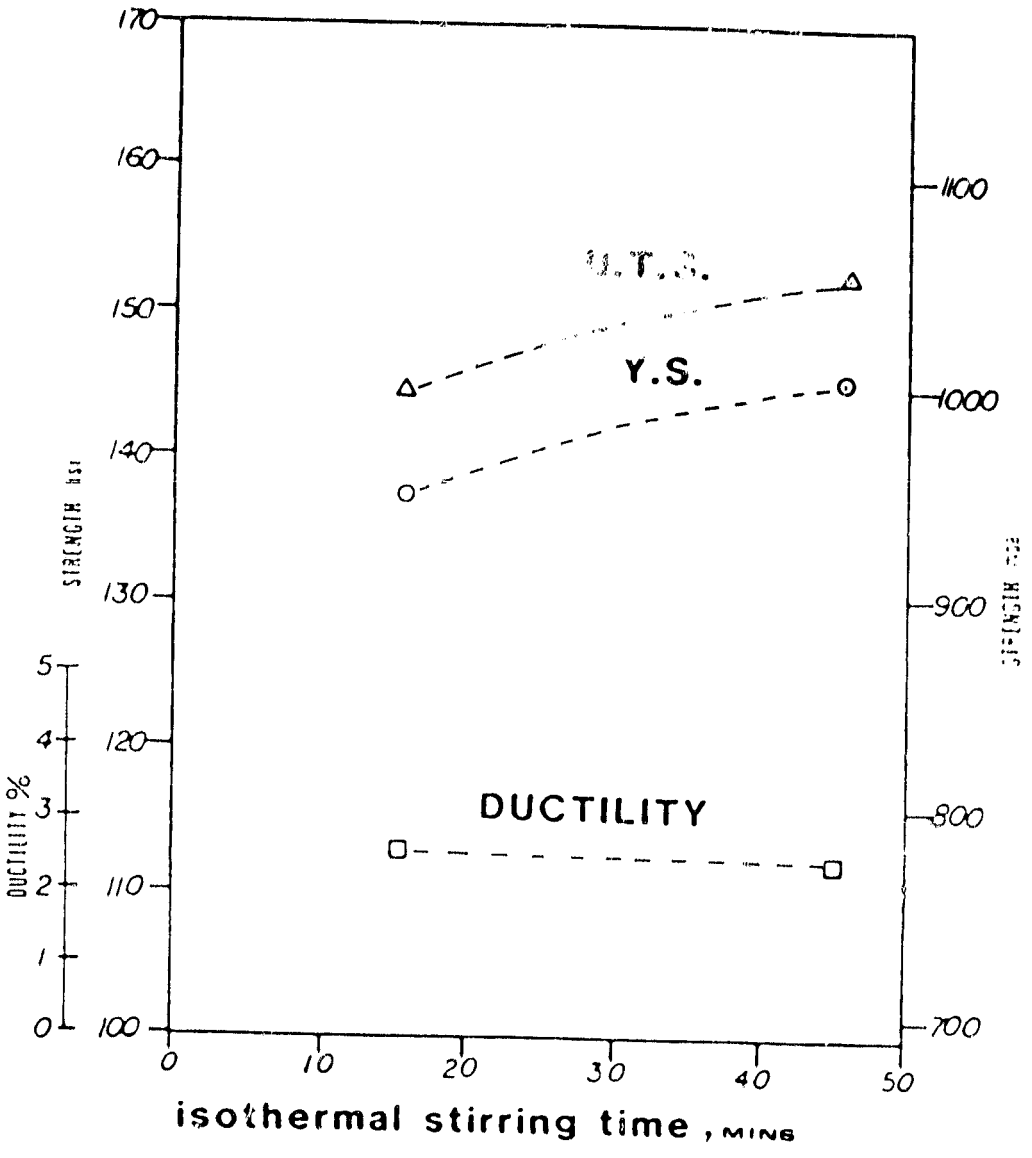


Figure 54. Tensile properties versus isothermal stirring time at 650°C in air at a constant stirring speed (325 rpm) and volume fraction solid (35%).

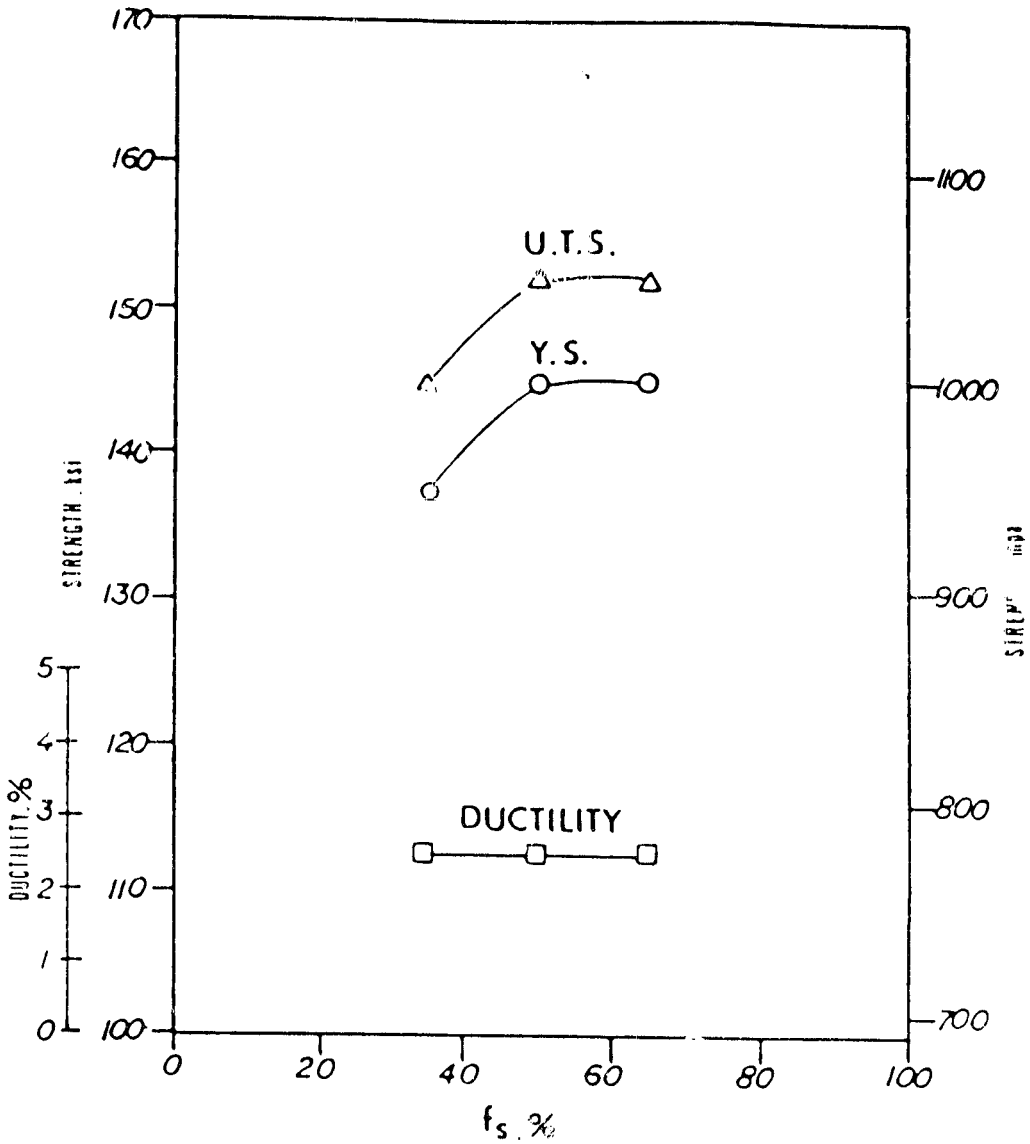


Figure 55. Tensile properties versus volume fraction solid at 650°C in air - at a constant stirring speed (325 rpm) and isothermal stirring time (15 minutes).

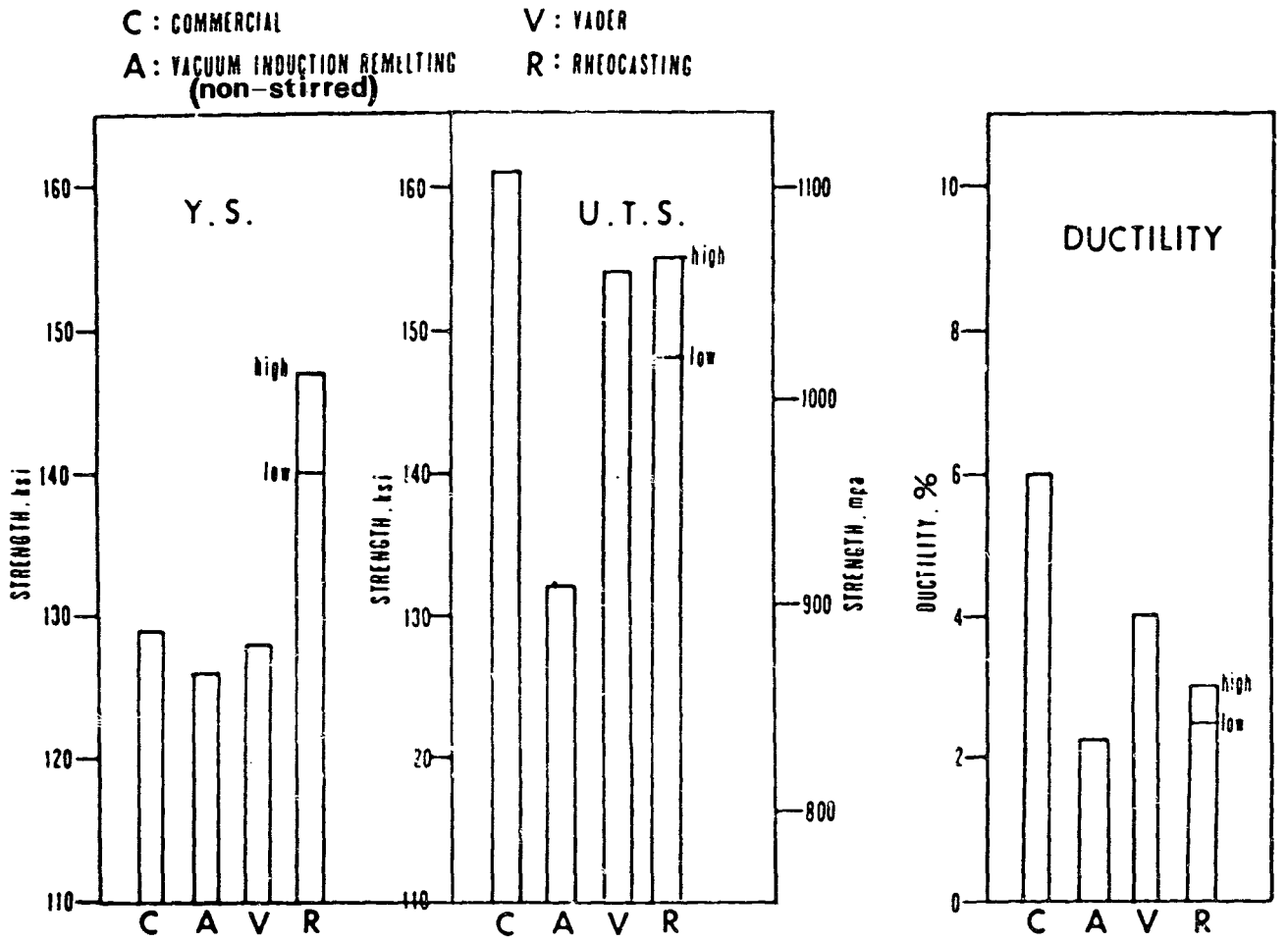


Figure 56. Tensile properties as a function of solidificaton processing technique at 650°C in air.

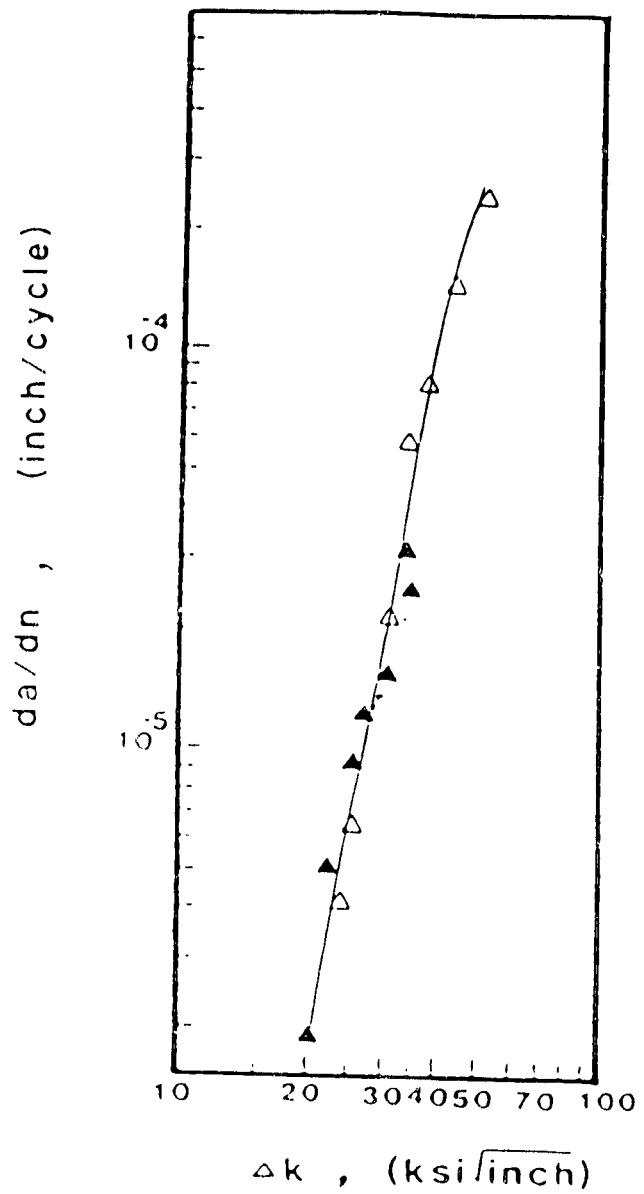


Figure 57. Fatigue crack propagation rate as a function of ΔK at 650° C in air for rheocast ingot (stirred at $\gamma$ = 560 rpm, $t_s$ = 15 minutes and fs = 35%) after HIP and heat treating. Duplicate specimens.

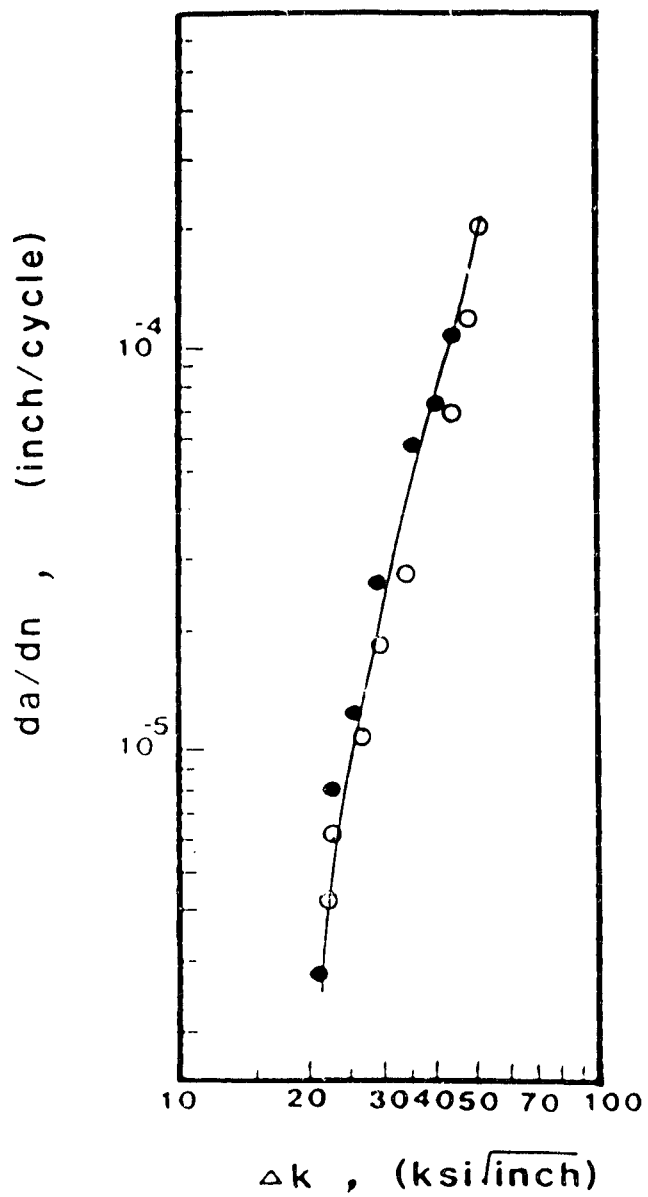


Figure 58. Fatigue crack propagation rate as a function of ΔK at 650°C in air for rheocast ingot (stirred at $\dot{\gamma}$ = 325 rpm, $t_s$ - 15 minutes and fs = 65%) after HIP and heat treating. Duplicate specimens.

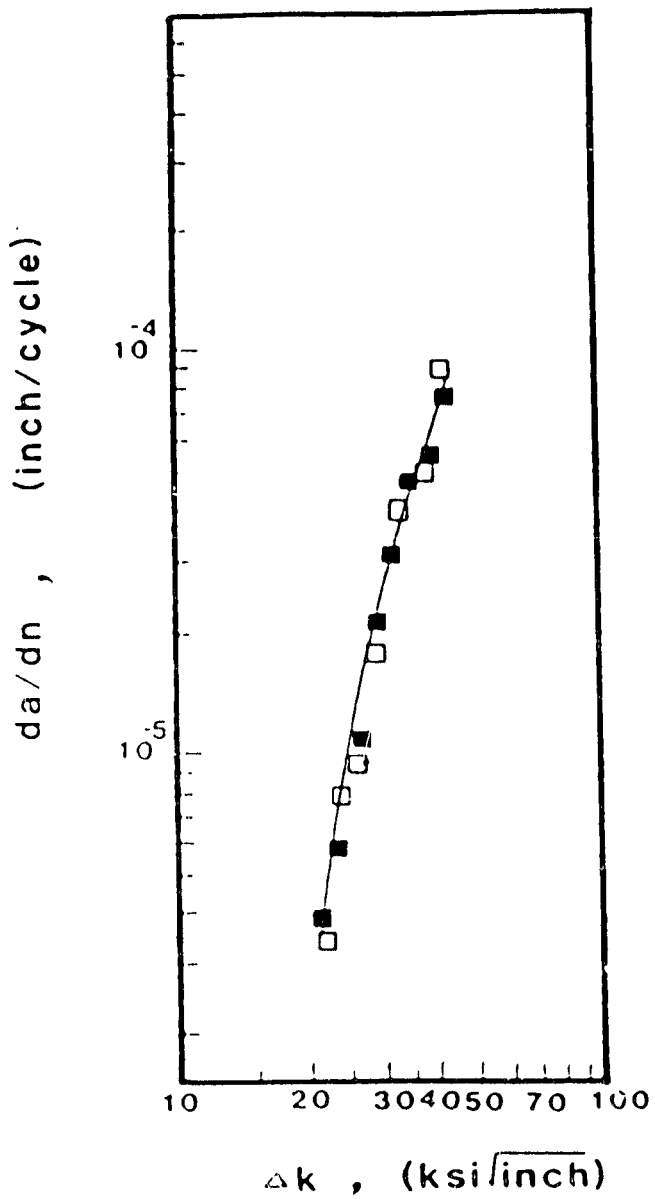


Figure 59. Fatigue crack propagation rate as a function of ΔK at 650°C in air for VADER ingot after HIP and heat treating. Duplicate specimens.

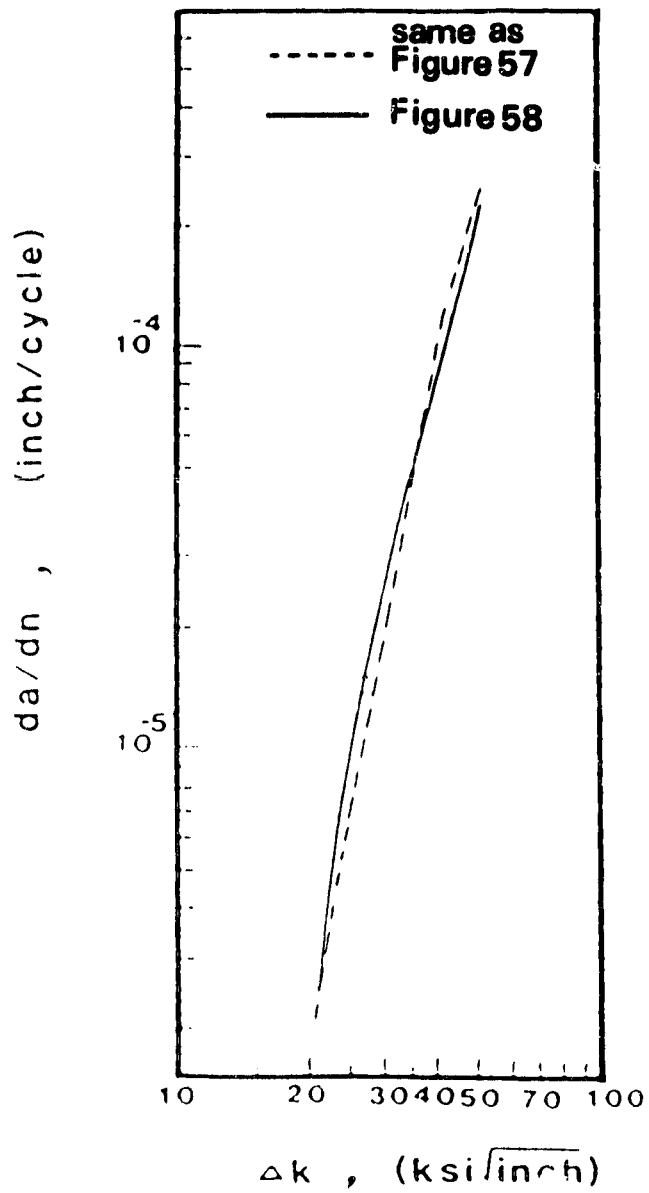


Figure 60. Fatigue crack propagation rate for two rheocast ingots at air in 650°C.

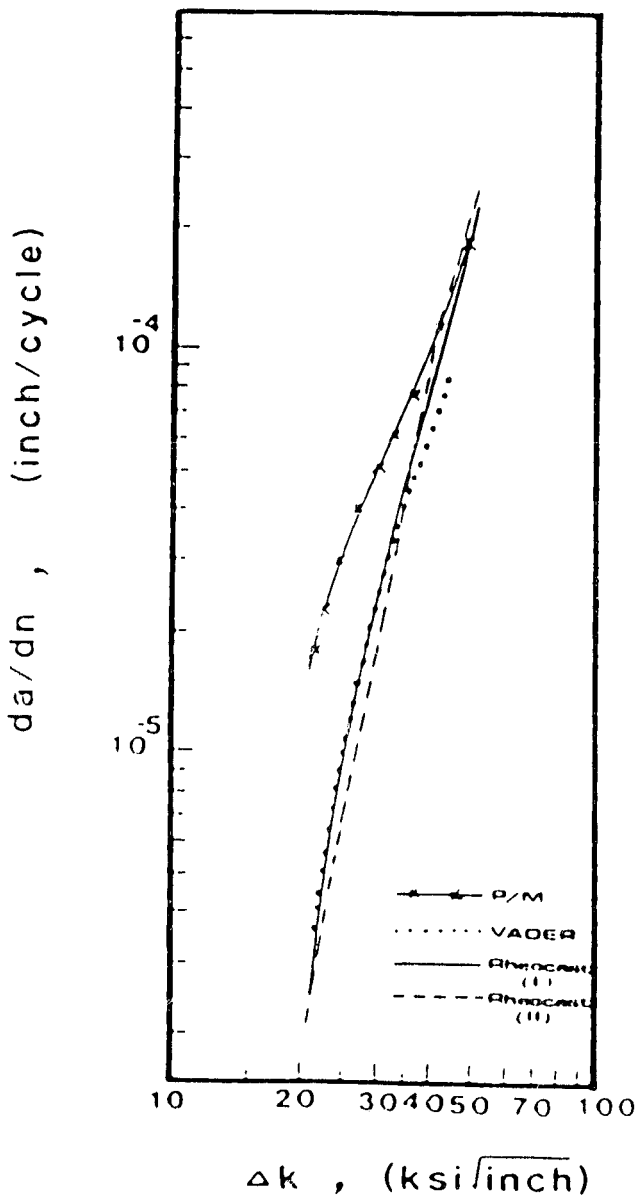


Figure 61. Fatigue crack propagation rate for various processing techniques at air in 650°C.

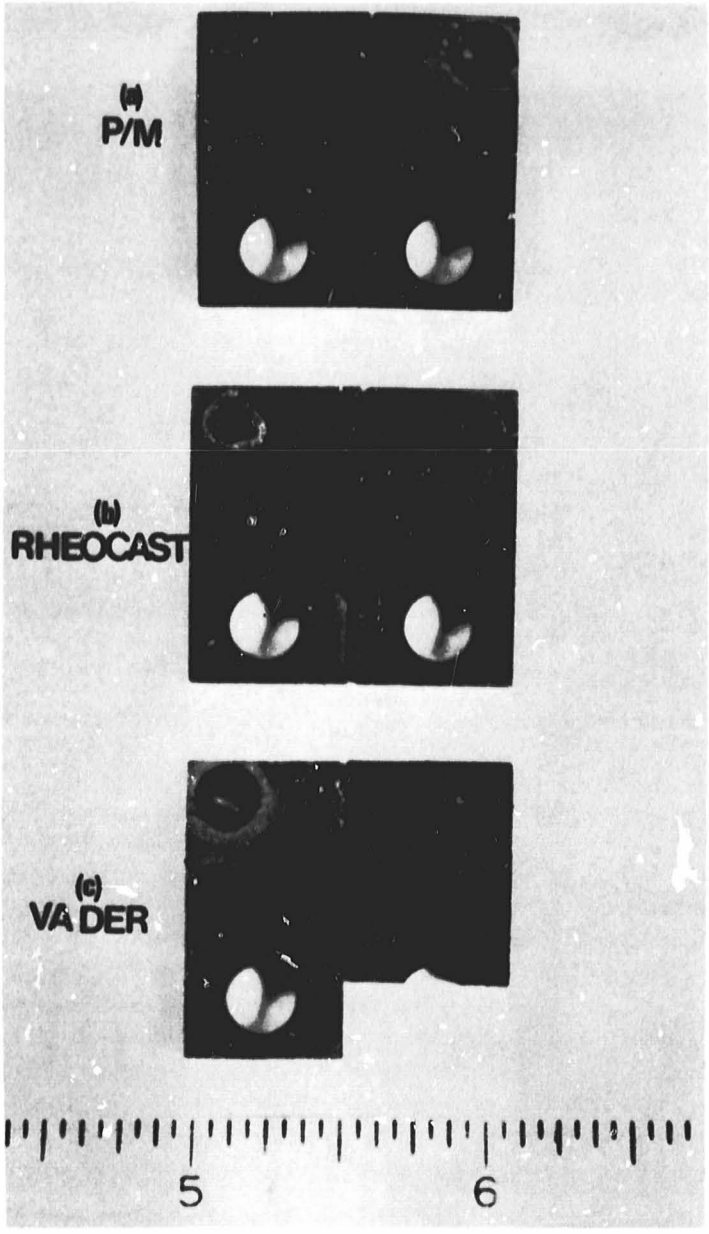


Figure 62. The macroscopic fracture appearance of the CT specimens. (a) P/M; (b) rheocast; (c) VADER process.

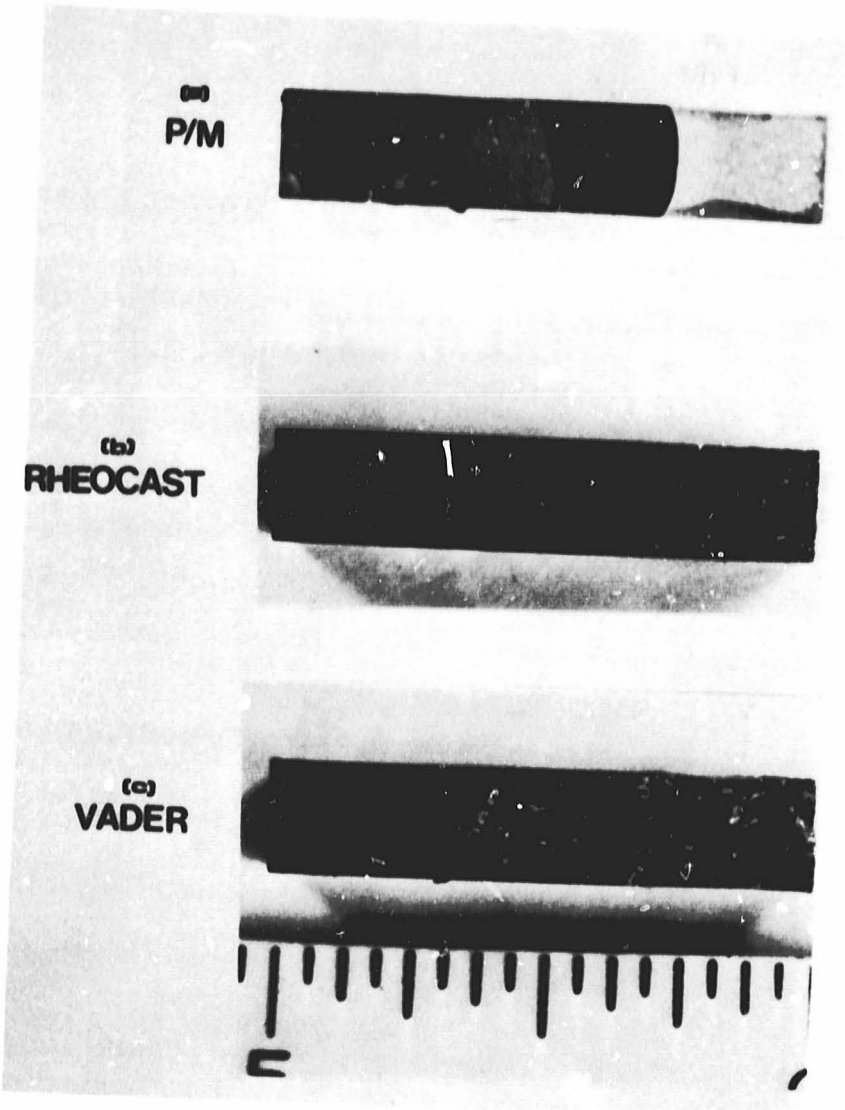


Figure 63. The fracture surface of the CT specimens. (a) P/M; (b) rheocast; (c) VADER process.

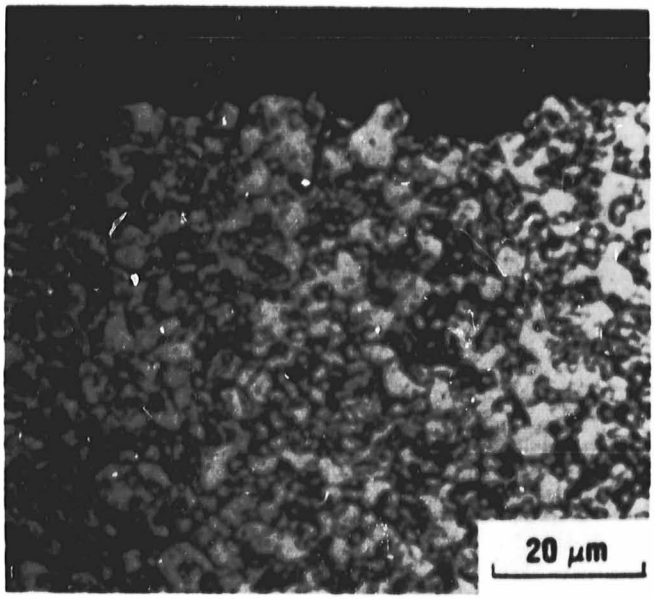


Figure 64. Optical micrograph of the stable crack growth for the P/M; crack is propagated from left to right.(99)

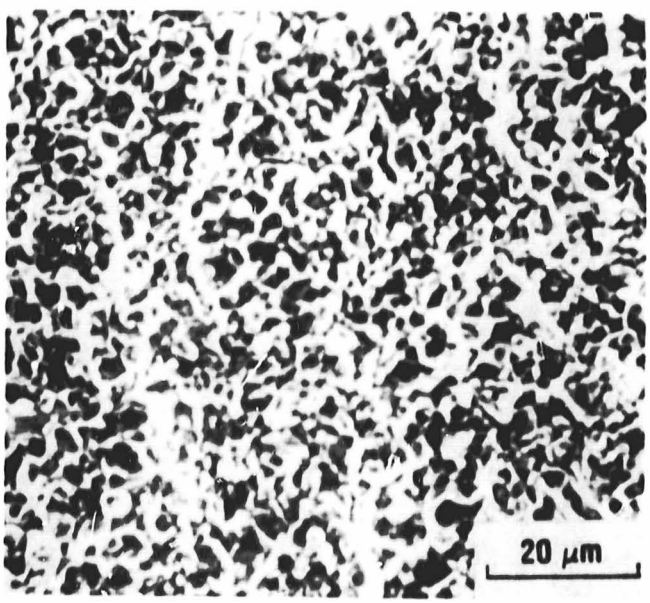


Figure 65. Representative SEM micrograph of the stable crack growth for the P/M. Crack is propagated from top to bottom.

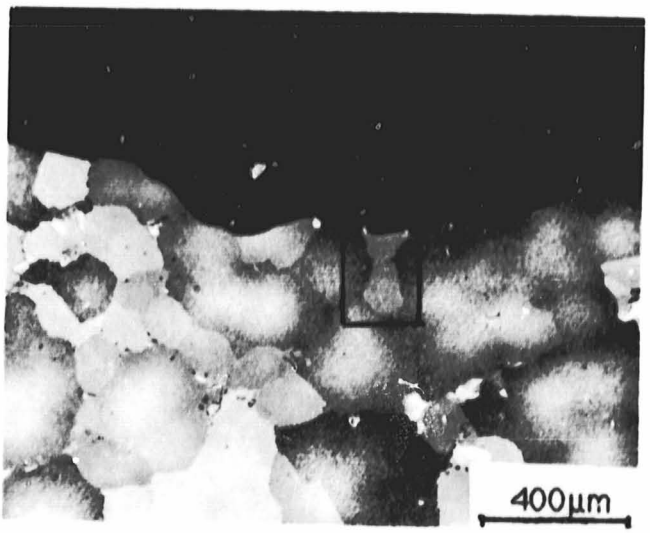


Figure 66. Optical micrograph of the stable crack growth for the rheocasting; crack is propagated from left to right.

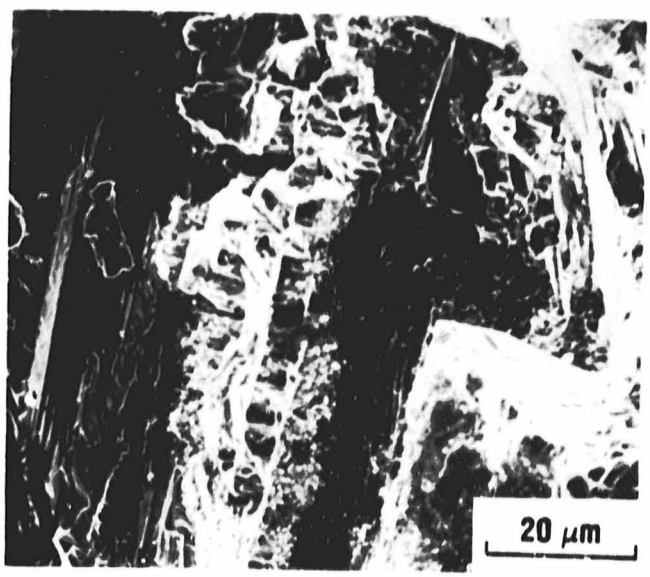


Figure 67. Representative SEM micrograph of the stable crack growth for the rheocasting; crack is propagated from top to bottom.

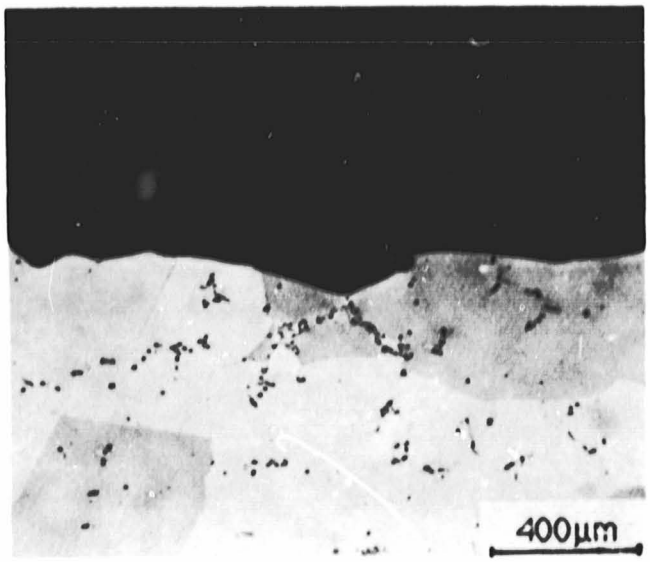


Figure 68. Optical micrograph of the stable crack growth for the VADER; crack is propagated from left to right.

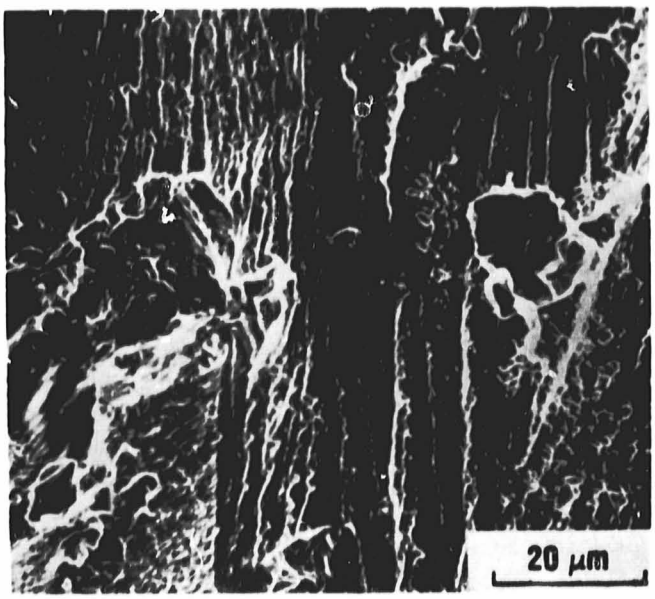


Figure 69. Representative SEM micrograph of the stable crack growth for the VADER; crack is propagated from top to bottom.

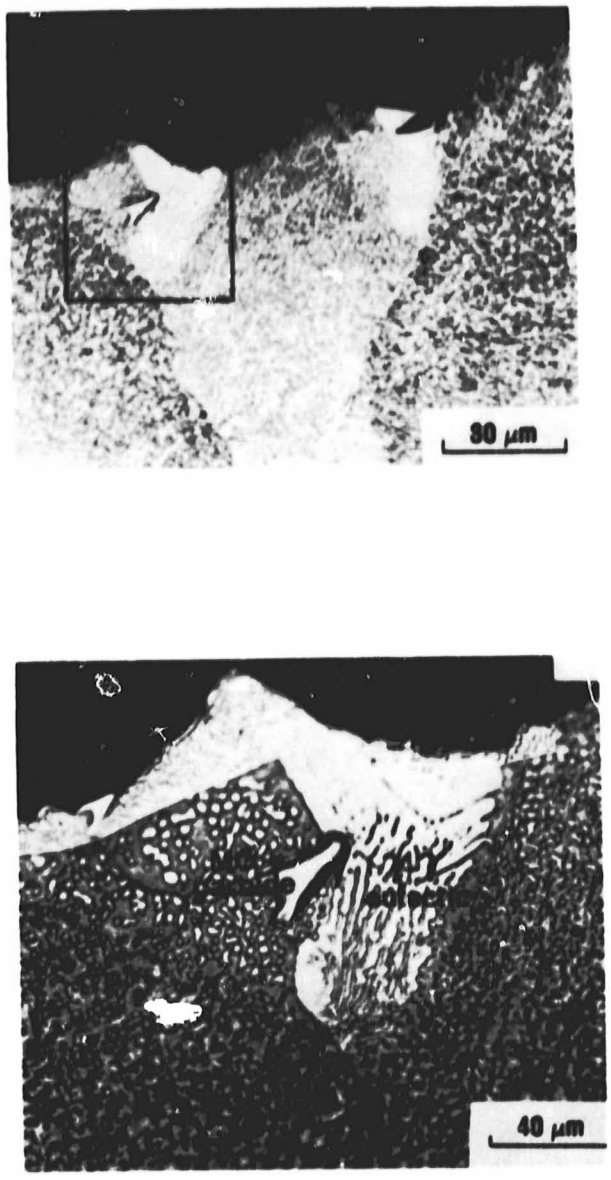


Figure 70. Crack propagation route in the region indicated in Figure 66 at high magnification.

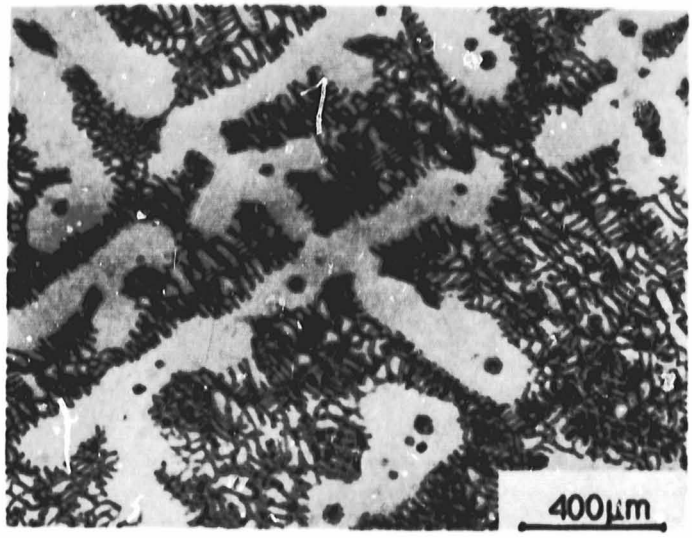


Figure 71. Representative microstructure of the reheated non-stirred IN-100 sample. 5 minutes of isothermal holding at $T_{fs}$ = 35% during reheating.

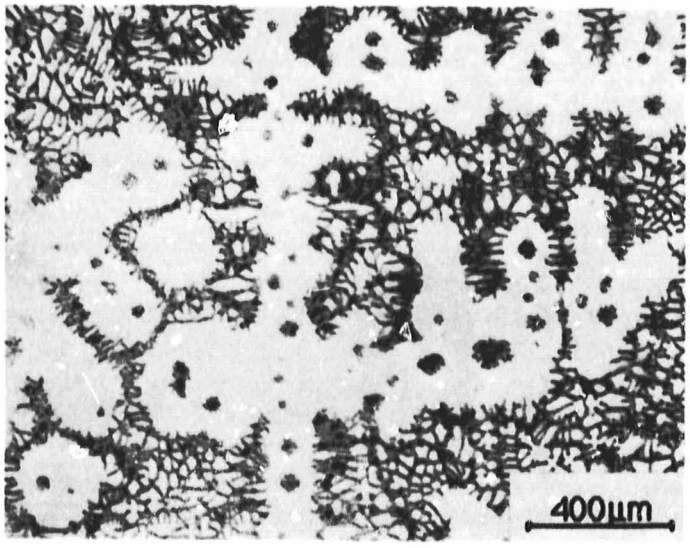


Figure 72. Representative microstructure of the reheated non-stirred IN-100 sample. 20 minutes of iscthermal holding at $T_{fs}$ = 35% during reheating.

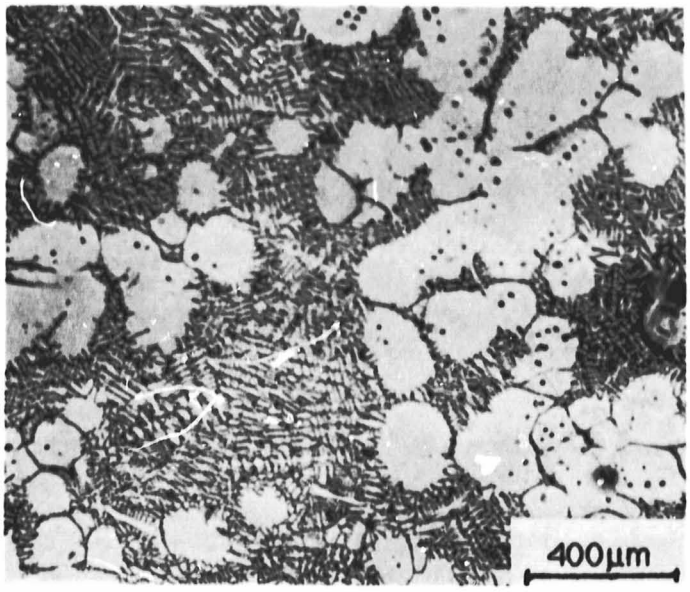


Figure 73. Representative microstructure of reheated rheocast IN-100 sample from ingot which were stirred at $\gamma$ = 325 rpm, $t_s$ = 15 minutes and fs = 35%.

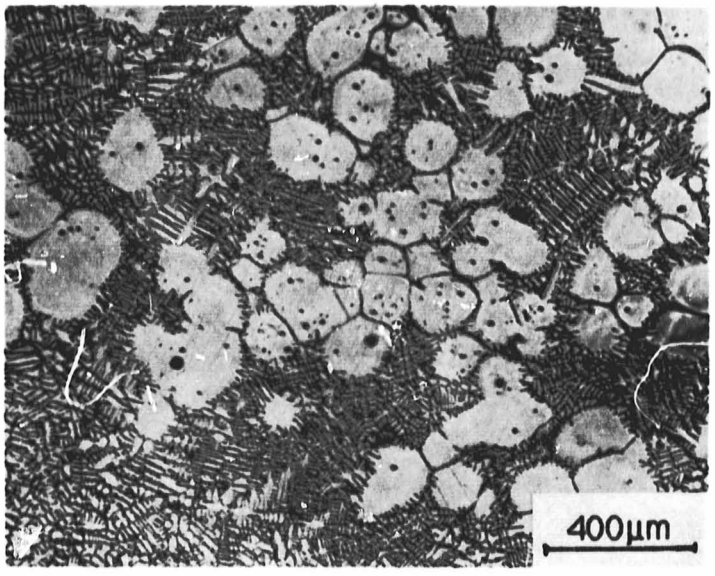


Figure 74. Representative microstructure of reheated rheocast IN-100 sample from ingots which were stirred at $\gamma$ = 560 rpm, $t_s$ = 15 minutes and fs = 35%.

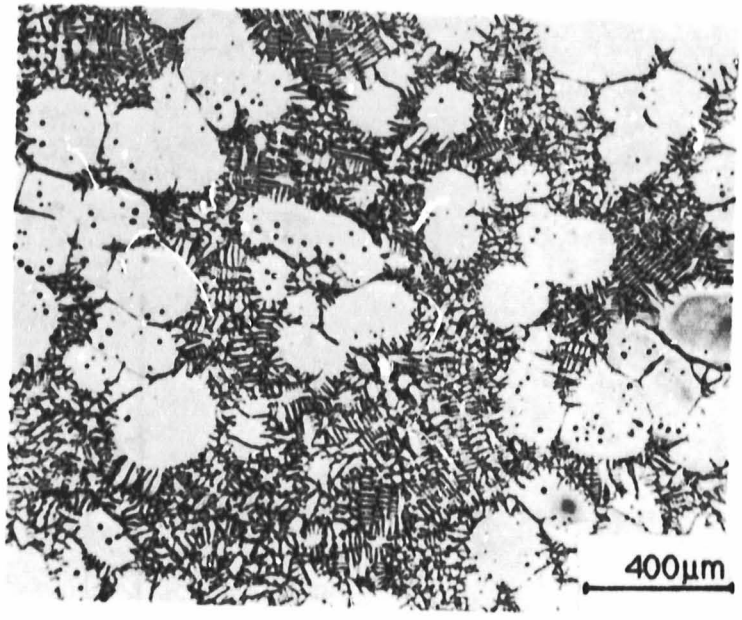


Figure 75. Representative microstructure of reheated rheocast IN-100 sample from ingot which were stirred at $\gamma$ = 325 rpm, $t_s$ = 45 minutes and fs = 35%.

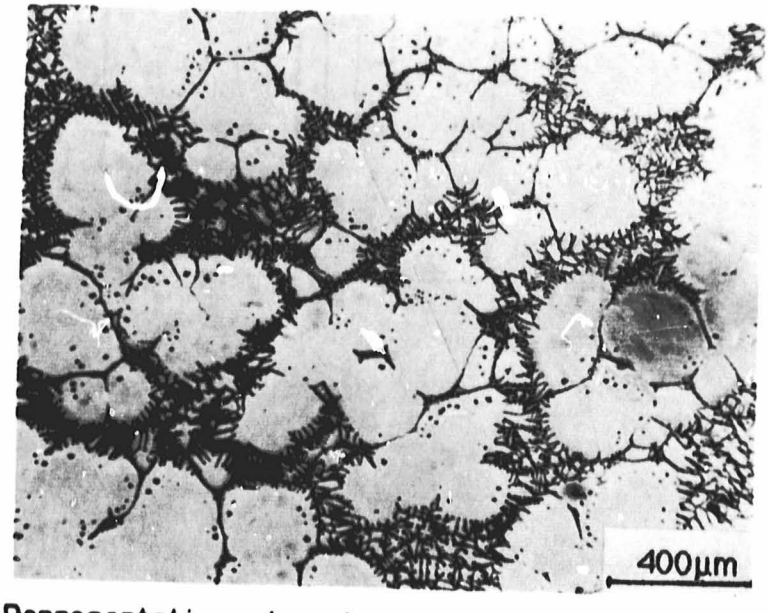


Figure 76. Representative microstructure of reheated rheocast IN-100 sample from ingot which were stirred at $\gamma$ = 325 rpm, $t_s$ = 15 minutes and fs = 65%.

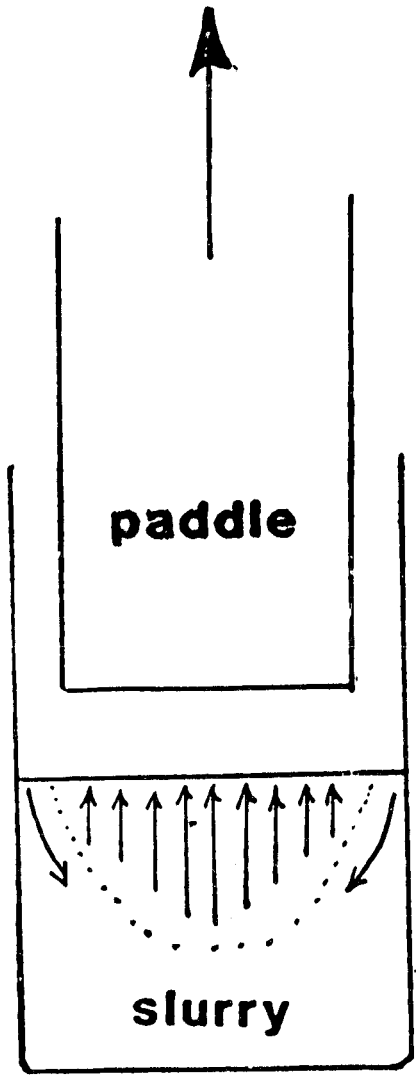


Figure 77. Assumed fluid flow pattern induced by lifting the paddle after terminating stirring.

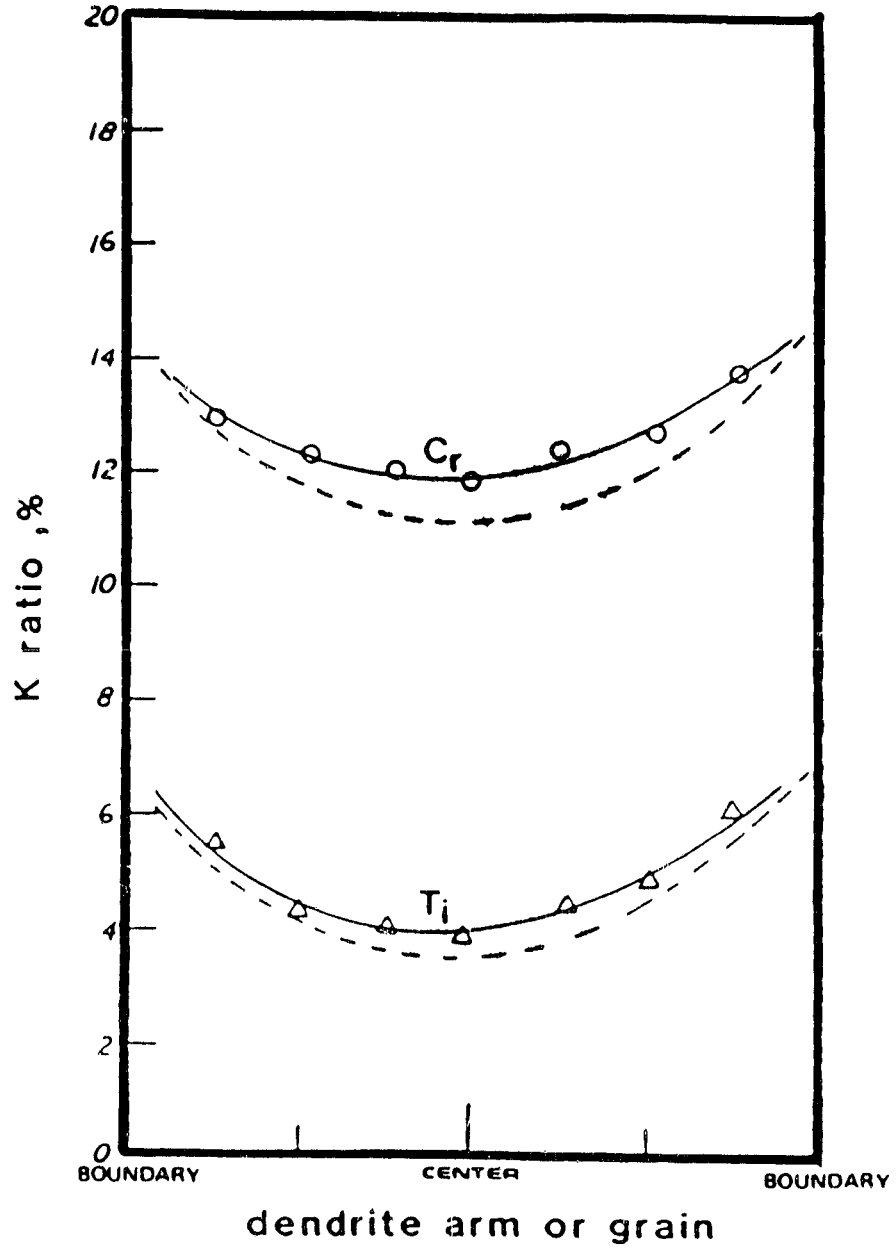


Figure 78. Ti and Cr concentration profiles of the dendrite arm in the V shaped region of the ingot from $\gamma$ = 325 rpm, $t_s$ = 15 minutesand fs = 35%. (dashed lines are concentration profiles in other locations of the ingot as shown in Figure 28).

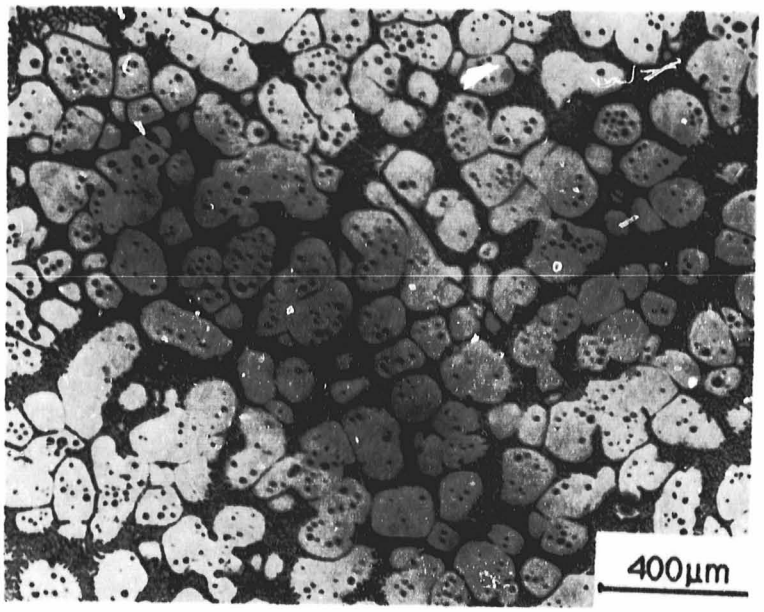


Figure 79. Representative microstructure of reheated VADER IN-100 sample. 5 minutes of isothermal holding at $T_{fs}$ - 65% during reheating.

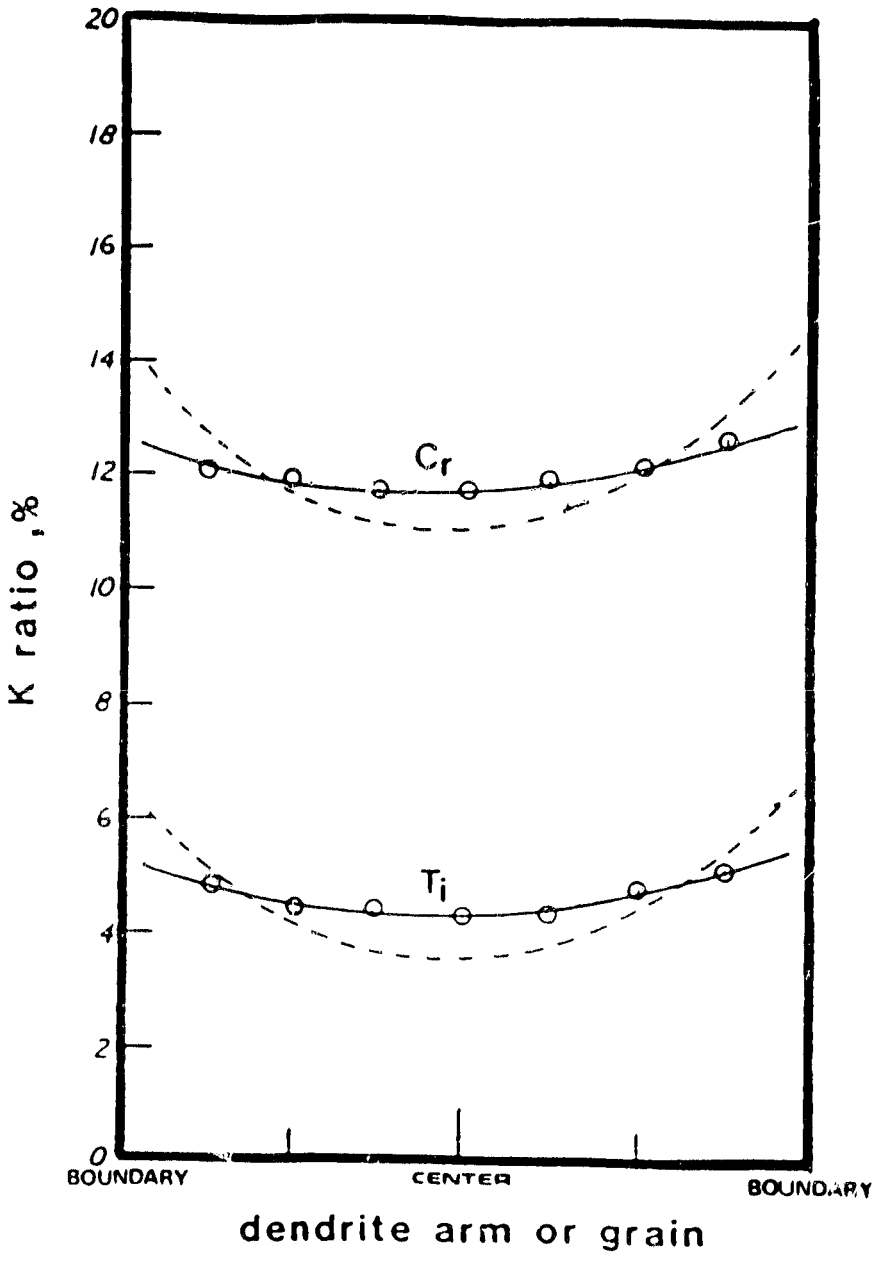


Figure 80. Ti and Cr concentration profiles of the ingot from y = 560 rpm, $t_s$ = 15 minutes and fs = 35% after HIP and heat treating (dashed lines are concentration profiles of as-cast ingot as shown in Figure 28).

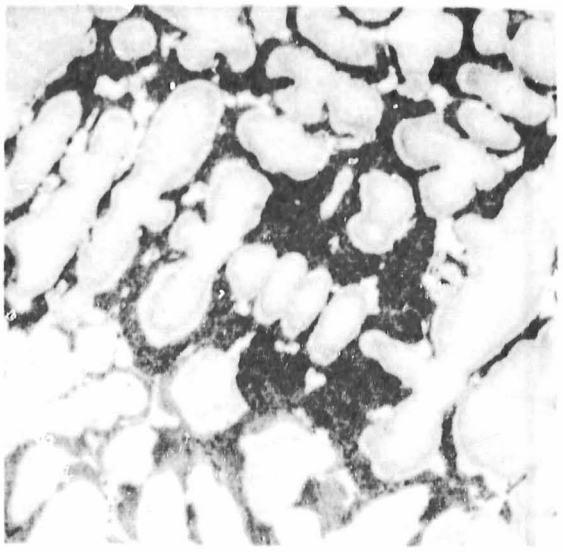

(a)

400µm



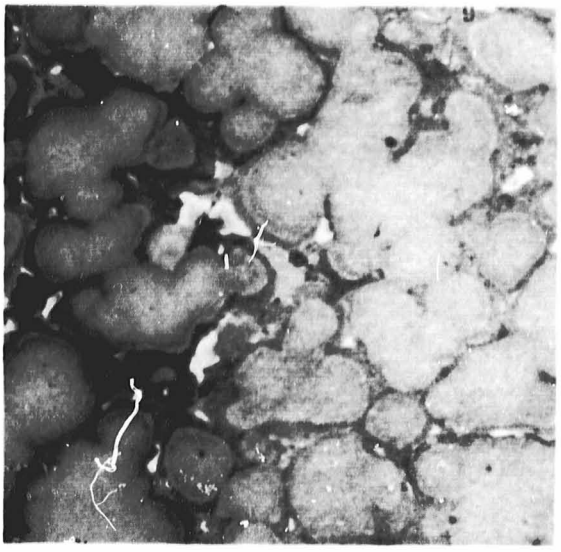

(b)

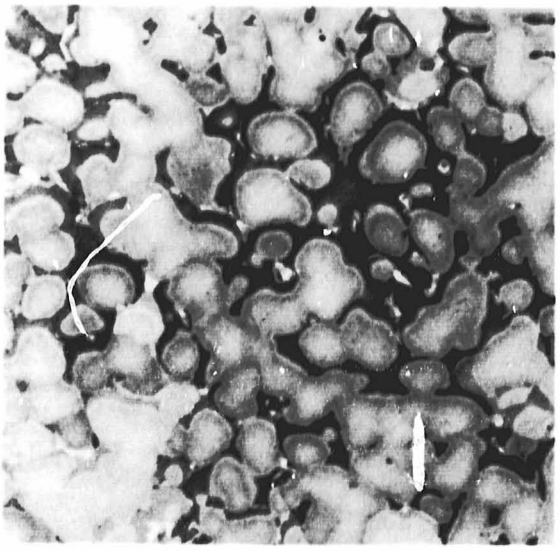

(c)

Figure 81. Representative microstructures after 3 hours of isothermal holding at temperature 1180°C (2160°F). (a) non-stirred; (b) rheocast; (c) VADER specimens.

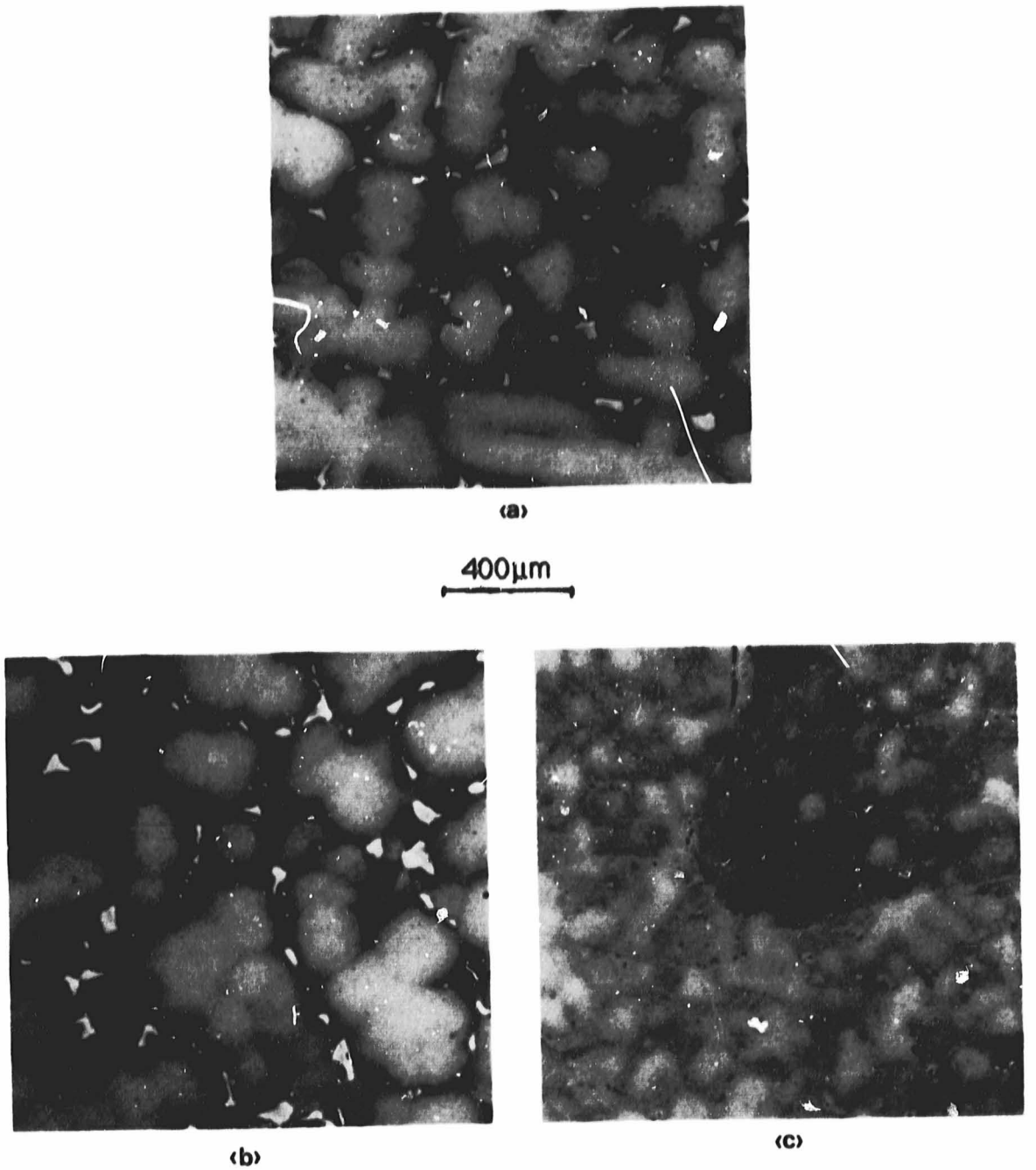


Figure 82. Representative microstructures after 3 hours of isothermal holding at temperature 1200°C (2190°F). (a) non-stirred; (b) rheocast; (c) VADER specimens.

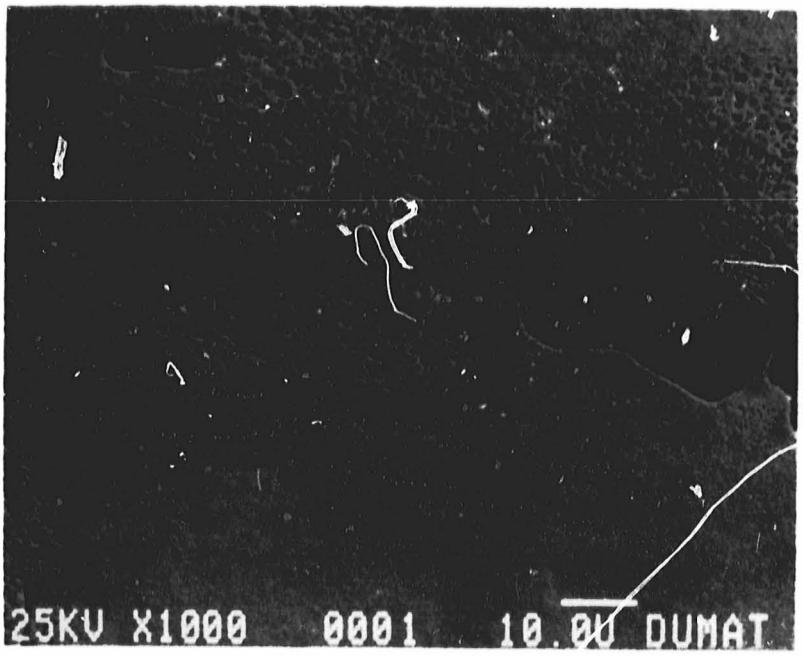


Figure 83. Representative SEM micrograph showing the size distribution of secondary precipitated γ' particles in the semi-grain or dendritic arm after homogenization experiment at 1180°C (2160°F).

a

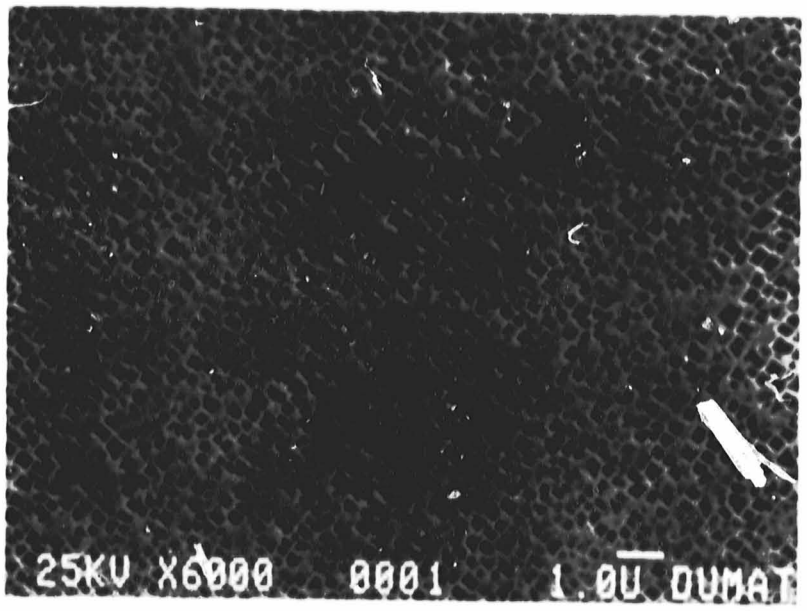


b

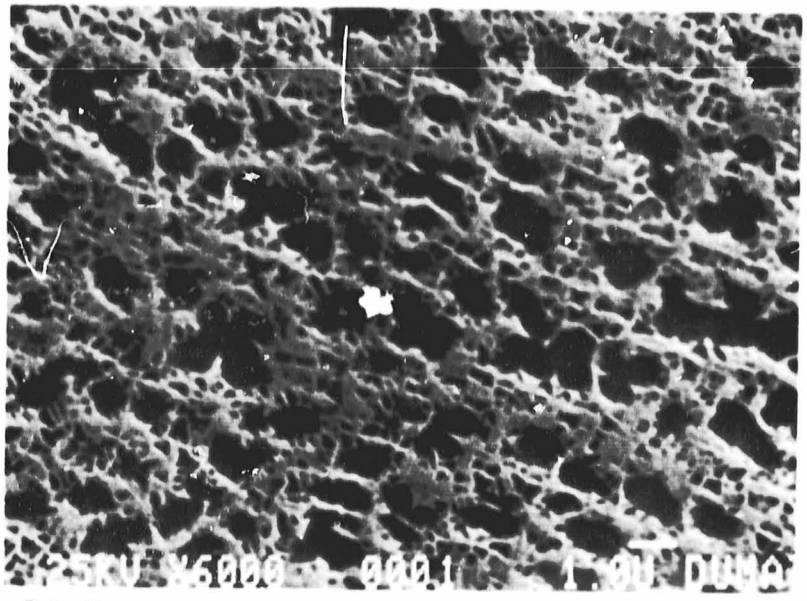

Figure 84. Representative SEM micrograph of the secondary precipitated γ'. (a) at the grain center; (b) near the boundary in Figure 83 at a higher magnification.

## REFERENCES


1. C.T. Sims and W.C. Hagel. The Superalloys, John Wiley & Sons, Inc., New York, April 1972.

2. G.W. Meetham, The Metall. and Mat. Tech., p. 307, Sept. 1982.

3. United Aircraft Corporation, U.S. Patent #3,519,503, 1970.

4. W. J. Boesch, J.K. Tien and T.E. Howson, Metal Progress, vol. 122, No. 5, p. 149, Oct. 1982.

5. W. J. Boesch, G.E. Maurer and C.B. Adasczik, paper presented in the Conference on "High Temperature Alloys for Gas Turbine - 1982" at Leige, Belgium, Oct. 1982.

6. M.C. Flemings, R.G. Riek and K.P. Young, Mat. Sci. and Eng., vol. 25, p. 103, 1976.

7. R.F. Decker, C.T. Sims, Chapter 2 in The Superalloys, Edited by C.T. Sims and W.C. Hagel, John Wiley & Sons, N.Y., p. 33, April 1972.

8. D.T. Decker, J. of Metals, vol. 33, No. 4, p. 24, 1981.

9. R.S. Cremisio, Chapter 13, in The Superalloys, Edited by C.T. Sims and W.C. Hagel, John Wiley & Sons, N.Y., April 1972, p. 373.

10. H.J. Klein and J.W. Pridgen, Superalloys - Proceedings of the Second Inter. Conf., held at Champion, PA, published by MCIC, page B, Sept. 1972.

11. J.F. Chang, G.P. Hu and L. Gao, Superalloys 1980, Edited J.K. Tien et al., ASM, Metals Park, Ohio, p. 245, 1980.

12. R. Schlatter, Superalloys - Proceedings of the Second Inter. Conf., held at Champion, PA, published by MCIC, page A, Sept. 1972,

13. J. Hockin, ibid., page C, Sept. 1972.

14. D. Apelian, AGARD Conference Proceeding No. 325: Advanced Casting Technology, published by NATO, Nevilly Sur Seive, France, p. 6:1-14, April 1982.

15. B.H. Kear and E.R. Thompson, Science, vol. 208; No. 23, p. 847, May 1980.

16. M. Gell, D.N. Duhl and A.F. Giamei, Superalloys 1980, Edited by J.K. Tien et al., ASM, Metals Park, Ohio, p. 205, 1980.

17. R. Mehrabian, B.H. Kear, M. Cohen, Rapid Solidification Processing - Principles and Technologies, Proceedings of the Int. Conf. on Rapid Solidification Processing, Baton Rouge, Claitor's Publishing Division, Nov. 1977.

18. N.J. Grant, J. of Metals, p. 20, January 1983.

19. G.H. Gessinger and M.J. Bomford, Int. Metall. Review, vol. 19, p. 5, 1974.

20. R.W. Jech, T.J. Moore, T.K. Glasgow and N.W. Orth, J. of Metals, vol. 36, No. 4, p. 41, April 1984.

21. S.T. Savage and F.H. Fores, J. of Metals, vol. 36, No. 4, p. 20, April 1984.

22. D.B. Snow, E.M. Breinan and B.H. Kear, Superalloys 1980, Edited by J.K. Tien, et al., ASM, Metals Park, Ohio, p. 189, 1980.

23. K.W. Stalken, U.S. Patent #3,758,347, Sept. 11, 1973.

24. C.T. Sims, J. of Metals, p. 1, Oct. 1966.

25. O.H. Kriege and J.M. Baris, Trans. ASM Quarterly, vol. 62, p. 195, 1969.

26. E. Hornbogen and M. Roth, Z. Metallkde, vol. 58, p. 842, 1967.

27. R.A. Ricks, A.J. Paten and R.C. Ecolb, Acta. Metall. vol. 31, p. 43, 1983.

28. P.G. Shewmon, Trans. Met. Soc., AIME, Vol. 233, p. 736, 1965.

29. W.W. Mullins and R.F. Sekerka, J. Appl. Phys., vol. 34, p. 323, 1963 and vol 35, p. 444, 1964.

30. A. Vogel, D.Phil. Thesis, University of Sussex, 1977.

31. R.D. Doherty, Metal Science, vol. 16, p. 1, January 1982.

32. B.J. Piearcey, B.H. Kear and R.W. Smachey, Trans. ASM Quarterly, vol. 60, No. 4, p. 634, Dec. 1967.

33. C.J. Burton, Superalloys - Metallurgy and Manufacture, Edited by B.H. Kear, et al., p. 147, Sept. 1976.

34. A. Havalda, Trans. ASM, vol. 62, p. 581, 1969.

35. J.R. Mihalisin, C.G. Rieber and R.T. Grant, Trans. Met. Soc. AIME, vol. 242, p. 2399, 1968.

36. G.S. Cole and R.S. Cremisio, Chapter 17 in The Superalloys, Edited by C.T. Sims and W.C. Hagel, John Wiley & Sons, N.Y., p. 479, April 1972.

37. R.F. Decker, Proceedings of Steel Strengthening Mechanisms Symposium, Zurich, Switzerland, p. 1, May 1969.

38. N.F. Stoloff, Chapter 3 in The Superalloys, Edited by C.T. Sims and W.C. Hagel, John Wiley & Sons, N.Y., p. 79, April 1972.

39. M. Doi and Y. Shimanuki, Superalloys - Proceedings of the 2nd Int. Conf., held at Champion, PA, published by MCIC, p. 0, Sept. 1972.

40. J.K. Tien and S. Purushothamang, Superalloys - Metallurgy and Manufacture, Edited by B.H. Kear, et al., p. 181, Sept. 1976.

41. B.H. Kear and D.P. Pope, to be published.

42. W.I. Mitchell, Z. Metallk. vol. 57, p. 586, 1966.

43. R.S. Cremisio and H.J. McQueen, Superalloy-Proceedings of the 2nd Int. Conf., held at Champion, PA, published by MCIC, page G, Sept. 1972.

44. S. Fulop and H.J. McQueen, ibid., page H.

45. J.W. Pridgeon, F.N. Darmara, J.S. Huntington and W.H. Sutton, Proceedings of the U.S.A. - China Bilateral Conf., held in Beijing, Nov. 1981, Edited by J. Tien and J. Elliott, p. 261, 1982.

46. J.M. Fleck, V.K. Chandhok and L.P. Clark, Superalloys - Metallurgy and Manufacture, Edited by B.H. Kear et al., p. 509, Sept. 1976.

47. P. Wildgoose, et al., Powder Met. No. 2, p. 1975, 1981.

48. F.H. Soykan and J.S. Huntington, U.S. Patent #4,261,412, April 1981.

49. M.C. Flemings, Proceedings of a Workshop held at the Army Materials and Mechanics Research Center, MCIC Report: MCIC-78-35, page 3, Jan. 1978.

50. R.A. Joly and R. Mehrabian, J. Mater. Sci., vol. 11, p. 1393, 1976.

51. R. Mehrabian and M.C. Flemings, Trans. AFS, vol. 80, p. 173, 1972.

52. H-I. Lee, D.Phil. Thesis, University of Sussex, March 1982.

53. E.F. Fascettan, R.C. Riek, R. Mehrabian and M.C. Flemings, Trans. AFS, vol. 81, p. 95, 1973.

54. D.B. Spencer, R. Mehrabian and M.C. Flemings, Metal. Trans., vol. 3, p. 1925, July 1972.

55. R.G. Riek, A. Vrachnos, K.P. Young, N. Matsumoto and R. Mehrabian, Trans. AFS, p. 25, 1975.

56. Y.V. Murty, D.G. Backman and R. Mehrabian, ibid. Ref. #51, p. 95.

57. V. Laxmanan, Master Thesis, MIT, June 1985.

58. R. Mehrabian, R.G. Riek and M.C. Flemings, Met. Trans., vol. 5, p. 1899, 1974.

59. S.D.E. Ramati, G.J. Abbaschian and R. Mehrabian, ibid Ref. #51, p. 85.

60. M.C. Flemings, Solidification Processing, McGraw Hill, 1974.

61. T.Z. Kattamis, U.T. Holmbery and M.C. Flemings, J. Inst. Metals, vol. 95, p. 343, 1967.

62. S.D.E. Ramati, D.G. Backman, Y.V. Murty, G. J. Abbaschian and R. Mehrabian, ibid Ref. #51, p. 13.

63. R.D. Doherty, H-I. Lee and E.A. Feest, Materials Science and Engineering, vol. 65, p. 181, 1984.

64. A. Vogel and B. Cantor, J. Crystal Growth, vol. 37, p. 309, 1977.

65. A. Vogel, R.D. Doherty and B. Cantor, Solidification and Casting of Metals, Proceedings of an Int. Conf. on Solidification at University of Sheffield, England, July 1977, The Metal Soc., p. 518.

66. H-I. Lee, R.D. Doherty, E.A. Feast and J.M. Tichmarsh, Solidification Technology in the Foundry and Cast House, Proceedings of an Inter. Conf. at University of Warwick, Coventry, Sept. 1980, The Metal Soc., p. 119.

67. H. Gleiter, G. Herrmann and G. Baro, Acta Met., vol. 7, p. 319, 1959.

68. C. Roques-Carmes, M. Aucouturier and P. Lacombe, Metal Science Journal, Vol. 7, p. 128, 1973.

69. MCIC Report: MCIC-78-35, Edited by R.D. French and F.S. Hodi, January 1978.

70. R.D. Doherty, Crystal Growth, edited by B.R. Ramplin, page 485, 1980.

71. K.C. Antony and J.F. Radavich, Superalloys - Metallurgy and Manufacture, Edited by B.H. Kear et al., p. 137, Sept. 1976.

72. A. Arzt, M.F. Ashby and K.E. Easterling, Metal. Trans. A, vol. 14A, p. 211, Feb. 1983.

73. K.C. Antony and J.F. Radavich, Superalloys 1980, Edited by J.K. Tien et al., ASM, Metals Park, Ohio, p. 257.

74. H.D. Hanes and J.M. McFadden, Metal Progress, vol. 123, No. 5, p. 23, April 1983.

75. H.D. Hanes, D.A. Scifer and C.R. Watts, MCIC Report: MCIC-77-34, p. 58, Nov. 1977.

76. G.H. Gessinger, P/M of Superalloys, Butterworth Co., p. 165,, 1984.

77. B.H. Kear, G.R. Leverant and J.M. Oblak, ASM Trans. Quart., Vol. 62, p. 639, 1969.

78. L.A. Weisenberg and R.J. Morris, Metal Progress, vol. 78, p. 70, Nov. 1960.

79. R.F. Decker and J.W. Freeman, Trans. AIME, vol. 218, p. 277, 1960.

80. R.W. Smashey, AIME Annual Meeting, Cleveland, Ohio, Oct. 1970.

81. E.L. Raymond, Trans. AIME, Vol. 239, p. 1415, 1967.

82. B.S. Natapon, V.I. Ol'shanetskii and E.P. Ponomarenki, Metal Science and Heat Treatment, vol. 1, p. 11, 1965.

83. W.J. Boesch and J.R. Slaney, Metal Progress, vol. 84, No. 1, p. 109, 1964.

84. J. Gayda and R.V. Miner, Met. Trans. A, vol. 14A, p. 2301, Nov. 1983.

85. G.E. Wasielewski and N.R. Lindblad, Elimination of Casting Defects Using HIP, MCIC report: MCIC-72-10, Sept. 1972.

86. P.C. Paris and F. Erdogan, J. of Basic Eng., vol. 85, p. 528, 1963.

87. S.R. Holdsworth, W. Hoffelner, Proceedings of a Conference held in Liege, Belgium, Oct. 1982, edited by R. Brunetand et al., p. 345.

88. T.C. Lindlay, C.E. Richards and P.O. Ritchie, Metall. and Metal Forming, vol. 43, p. 268, 1976.

89. M.S. Miller and J.P. Gallagher, "Fatigue Crack Growth Measurement and Data Analysis", ASTM STP 738, Edited by S.J. Hudak, Jr., et al., ASTM, page 205, 1981.

90. R.P. Wei, ASME Paper No. 73-DE-22, N.Y., April 1973.

91. M. Clavel and Pineau, Met. Trans., A, vol. 9A, p. 471, April 1978.

92. H.F. Merrick and S. Floreen, Met. Trans. A, vol. 9A, p. 231, Feb. 1978.

93. D.E. Macha, Engineering Fracture Mechanics, vol. 12, p. 1, 1979.

94. M. Gell and G.R. Leverant, Mechanisms of High Temperature Fatigue, ASTM STP 520, ASTM, p. 37, 1973.

95. A.M. Beltran, and D.A. Shores, Chapter 11 in The Superalloys, Edited by C.T. Sims and W.C. Hagel, John Wiley & Sons, N.Y., p. 317, 1972.

96. S. Floreen and R.H. Kane, Nickel Topics, vol. 34, No. 2, p. 6, 1981.

97. S. Floreen and J.M. Davidson, Met. Trans., vol. 14A, p. 895, May 1983.

98. J.C. Runkle and R.M. Pelloux, Fatigue Mechanisms, Edited by J.F. Fong, ASTM 675, ASTM, p. 135, 1979.

99. J. Gayda and R.V. Miner, NASA TM-81740, April 1981.

100. J. Gayda and R.V. Miner, Int. J. of Fatigue, Vol. 5, No. 3, p. 135, July 1983.

101. B.A. Cowels, D.L. Sims, J.R. Warren and R.V. Miner, Jr., Trans. of the ASME, vol. 102, p. 356, Oct. 1980.

102. S. Floreen and R.H. Kane, Superalloys 1980, Edited by J.K. Tien et al., ASM, Metals Park, Ohio, p. 595, 1980.

103. S. Floreen, Micro and Macro-Mechanics of Crack Growth, Edited by K. Sadananda et al., TMS-AIME, Warrendale, PA, p. 177, 1982.

104. S.K. Hwang and C.S. Pande, Met. Trans., Vol. 14A, p. 2021, Oct. 1983.

105. J.M. Oblak and W.H. Rand, Met. Trans., vol. 7B, p. 699, 1976.

106. R. Viswanathan and C. Bauer, Acta Met., vol. 21, No. 8, p. 1099, 1973.

107. M.A. Taha and N.A. Mahallawy, Proceedings of 46th Int. Foundry Conf., Madrid, paper No. 15, 1979.

108. H.B. Aaron and G.R. Kotler, Met. Trans., vol. 2, p. 393, 1971.

109. J. Gayda, R.V. Miner and T.P. Gabb, Superalloys 1984, Edited by M. Gell et al., TMS-AIME, p. 733, Sept. 1984.

110. S.J. Choe, S.V. Golwalker, D.J. Duquette and N.S. Stoloff, ibid., p. 311.

111. M. Rafalin, Ph.D. Thesis, Drexel University, 1981.

## APPENDIX A

## PROCESS DEVELOPMENTS IN NICKEL - BASE SUPERALLOYS

### A-1. Melting and Refining Technologies

The current and future melting and refining technologies that are used to process nickel-base superalloys are listed below:

- Air induction/arc melting - AIM/AIA (9)
- Vacuum induction melting - VIM (9)
- Vacuum arc remelting - VAR (9)
- Electroslag remelting - ESR (10,11)
- Plasma melting (9)
- Electron-beam melting - EBM (12)
- (Vacuum) investment casting (9,13)
- Vacuum arc double electrode remelting - VADER (4,5)

Basically, the ideal casting process should provide a clean and consistent end product with a low gas content, inclusions and impurities In addition, a high level of reliability and productivity with a low operating cost is desired (12). This is a tall order and difficult to achieve by a single melting/refining/casting process. The commercial producers have thus been forced to "marry" several processes to take advantage of and combine the best features of the individual respective processes (12). In fact, double VAR technique is an acceptable processing method to satisfy the stringent impurity

specifications.

The vast majority of the commercially produced castings (through melting and refining techniques) exhibit a dendritic structure. Control of the cast structure is the underlying objective in superalloy manufacturing processes. Most nickel-base superalloys contain a large amount of various alloying elements; therefore they freeze over a wide freezing range (liquid/solid- mushy zone). The excessive tendency of these alloys to segregate as well as the extent of hot-tearing which results during the "journey" through the mushy zone, coupled with the microsegregation which evolves during dendritic growth results in a cast structure full of inhomogeneities which makes subsequent forging and grain size control most difficult. Therefore, the amount of time spent in the mushy zone (...the local solidification time), as well as the width of the mushy zone are two important parameters which need to be addressed to control the resultant cast structure (14).

A-2. Directional Solidification (15)

Directional solidification is the process where heat is extracted in only one direction which permits the production of castings with grains aligned in the direction of the maximum stress with no grain boundaries normal to this direction. Overall segregation, porosity, carbides and grain boundary precipitates are reduced through directional solidification processing. However, the grains may diverge from the truly axial direction giving rise to grain boundary components which may be oriented normal to the applied stress direction.

A-3. Single Crystal Processing (15,16)

Single crystal processing produces castings consisting of only one crystal and results in complete absence of grain boundaries. This process eliminates the use of certain elements such as C, B, Zr and Hf which are necessary elements in conventional castings (polycrystalline castings) because they provide grain boundary strengthening. The benefit of reducing the levels of C, B, Zr, and Hf is that the solidus temperature of the casting is increased permitting high temperature solution treatments which leads to reduced levels of chemical segregation and uniform distribution of $\gamma'$ particles. The allowable operating temperature of single crystal processed castings is higher than those which have been processed otherwise.

A-4. Rapid Solidification Technologies (RST) - "Microcasting"

While segregation occuring during solidification cannot be avoided, its adverse effects can be at least partially eliminated by employing rapid solidification techniques. The local solidification time in RST is extremely small giving rise to cooling rates of $10^5$-$10^8$ °C/s; the segregate spacing and the dendrite arm spacing in the resulting castings are thus significantly reduced. In RST processed castings segregation occurs over a distance on the order of a few tens of microns or less, and thus subsequent homogenization is quite rapid. Other advantages with RST when compared to conventional casting techniques are refined grain size, increased solid solubility and the elimination of certain segregate phases (17-18).

Nickel-base superalloys have been processed by the following RST techniques:

- Powder metallurgy (19)
- Melt spinning (20)
- Splat quenching (21)
- Laser glazing (22)

## A-5. Mechanical Alloying to Produce Oxide Dispersion Strengthened (ODS) Alloys (23)

The mechanical alloying process to produce oxide dispersion strengthened nickel base superalloys is essentially a dry, high energy ball milling process in which the particles of elemental or prealloyed powder are continually being welded and broken until a homogeneous mixture of the constituent powder particles and dispersoids is achieved. Subsequently the ODS powders are consolidated and thermomechanically processed to produce the desired component.

## APPENDIX B

## General Microstructure and Strengthening Mechanisms in Nickel-Base Superalloys

### B-1. General Microstructure

In general, the nickel-base superalloys can be characterized by the following features (7):

#### B-1.1 Alloy Matrix

The continuous matrix is a FCC nickel-rich austenitic phase, which usually contains a high percentage of solid solution elements such as Co, Cr, Mo, W, Fe and V.

#### B-1.2 Gamma Prime

Al and Ti are added in amounts and mutual proportions to precipitate a high volume fraction of FCC ($A_3B$) type $\gamma'$. The compatibility of the $\gamma'$ crystal structure ($L1_2$) and lattice constant with $\gamma$ allows homogeneous nucleation of a precipitate with low surface energy and extraordinary long-time stability.

Typically, in a nickel-base superalloy, $\gamma'$ is $(Ni,Co)_3(Al,Ti)$ with Ni and Al dominating. However, the volume fraction of $\gamma'$ depends not only

on the Al and Ti content, but also on the amounts of Ni, Ta, W and Mo in the alloy, since these elements are known to partition to γ' phase (25); γ' can transform to the $Ni_3(Nb,Ta)$, when the Nb or Ta contents are sufficiently high.

The γ' phase precipitates out having a spherical morphology and subsequently this evolves to a cuboidal morphology (26). Recently, Ricks et al. (27) have investigated the growth of γ' precipitates in nickel-base superalloys. They concluded that the morphological development of γ' particles is in the following sequence: spheres - cuboids - cuboidal arrays (i.e. faceted dendritic or arrowhead particles) - dendrites (true dendrites) and that growth is most likely diffusion controlled. The onset of the cuboidal morphology is related to the magnitude of the lattice misfit of γ'/γ, and the volume fraction of γ' particles (27). However, the wavelength of the true dendritic perturbations in the final stage of the morphological sequence is not a function of the lattice mismatch but appears to be dominated by the solute profile at the growing γ' particles (27).

The formation of unusual solid state dendrites has been considered by Sherman (28) using the stability theory which was initially proposed by Mullins and Sekerka (29) in a spherical crystal growing from supersaturated vapor. Furthermore, Vogel (30) pointed out that solid impingement of the diffusion fields is also one stabilizing effect in addition to Sherman's consideration. Doherty (31) has taken the above a step further and has recently concluded that solid state dendrites may only be expected to form if the following conditions are met: (i) isotropic interface energy between the phases; (ii) low diffusivity

within the precipitate; (iii) low lattice mismatch between the two phases, and (iv) precipitates are widely spaced.

The γ' particle distribution and morphology in the cast structure is affected by the mode of microsegregation. Piearcey et al. (32) have observed the morphological transformations of γ' in directional solidified nickel-base superalloy. No significant differences in size, shape or volume fraction of precipitate is observed in similar sections taken from both the top and bottom parts of the ingot. On the other hand, a gradient in the size of the γ' precipitates was observed within the dendritic structure: a fine dispersion of γ' precipitates existed at the core of the dendrites (in both the top and bottom sections of the ingot), whereas the γ' precipitates at the outer periphery of the dendrites were much coarser.

B-1.3 Carbides

Carbon is added to levels of about 0.05 - 0.2% and with the reactive and refractory elements present to form carbides. The common classes of carbides in nickel-base superalloys are MC, $M_{23}C_6$, $Cr_7C_3$ and $M_6C$ (7).

The MC carbides, e.g. TiC, VC and (Ti,Mo)C, are believed to evolve in the mushy zone. Precipitation takes place immediately following formation of the primary dendrites (33). The MC carbides are FCC and usually exhibit coarse and discrete cubic or script morphology (1). The MC particles are heterogeneously distributed throughout the matrix, both at the intergranular and transgranular locations and often interdendritically.

$Cr_7C_3$ carbides have been found as irregular blocky particles in simple alloys with low Cr content and low reactive and refractory element content. They are not usually stable in nickel-base superalloys. Addition of Co, Mo, W or Cb prevents the formation of the $Cr_7C_3$ carbide (34).

$M_{23}C_6$ carbides , e.g., $Cr_{21}(Mo,W)_2C_6$, are profuse in alloys with moderate to high Cr content. They form during low-temperature heat treatment and service, that is 760°C - 980°C (1400 - 1800°F), both from degeneration of MC carbides and from soluble carbon residual in the alloy matrix. The $M_{23}C_6$ carbides are present not only at grain boundaries but also occasionally along twin lines and stacking faults. $M_{23}C_6$ carbides have a complex cubic structure. $M_{23}C_6$ can be avoided by heat treatment and chemistry control.

$M_6C$ carbides form at slightly higher temperatures such as 815-980°C (1500-1800°F), than $M_{23}C_6$. They usually precipitate when the refractory metal content in the alloy is high. Typical formulas for $M_6C$ are $(Ni,Co)_3Mo_3C$ and $(Ni,Co)_2W_4C$. Since $M_6C$ carbides are stable at higher temperatures than $M_{23}C_6$ carbides, $M_6C$ is more beneficial as a grain boundary precipitate to control the grain size.

B-1.4 Borides

Boron is generally present to the extent of 50-500 ppm in superalloys and is an essential ingredient. Boron reacts to form boride,

i.e. $M_3B_2$. Borides are hard, refractory particles observed only at grain boundaries. The shape of borides varies from blocky to half-moon shape. They often will appear to grow from a grain boundary into an adjacent grain.

B-1.5 TCP (Topologically Closed Packed) Type Phases

The TCP phases commonly found in nickel-base superalloys are ß, μ and Laues. These phases may appear as thin plates and are often found near grain boundaries where elements critical to the formation of TCP, such as Cr and Mo, are high (35).

B-1.6 Grain Boundary γ'

An example of this is the γ-γ' eutectic which forms preferentially at grain boundaries and in the interdendritic areas (33). These γ-γ' islands are affected by one or more of the following factors during freezing: local changes in composition arising from segregation; the presence of nuclei in the liquid upon which these phases can nucleate (36). γ' also forms upon reaction of γ with the metal carbides at the grain boundaries. This reaction is maintained by substitutional solutes, such as Cr, diffusing to the grain boundary.

B-2 Strengthening Mechanisms in Nickel-Base Superalloys

Nickel base superalloys are characterized by the basic structure of γ matrix and precipitation hardened by γ', $Ni_3(Al,Ti)$. Moreover, the alloys are further hardened by variation of relative amounts of Al and Ti, or by some optimum additions of such elements as Co, Fe, Mo, W, B,

Zr and C. The strengthening mechanisms of nickel base superalloys have been discussed and reviewed in several publications (37-42). The hardening is believed to be mainly influenced by the relative contribution of the following two features which are further discussed below:

(a) solid solution hardening of the matrix $\gamma$

(b) precipitation hardening due to $\gamma'$ precipitates

(a) Solid Solution Hardening

Solid solution hardening capability of various alloying elements up to 0.6 $T_M$ has been related to atomic size misfit in the matrix $\gamma$ as measured by lattice expansion (38). In addition, a superimposed effect can be attributed to the electron vacancy number. Part of this additional effect may result from lowering of the stacking fault energy which inhibits cross-slip. At higher temperatures, above 0.6 $T_M$ and in the range of high temperature creep, $\gamma$ strengthening is diffusion dependent. Elements such as Mo and W are quite influential at these high temperatures.

(b) Precipitation Hardening

The strengthening of alloys by precipitates can be expressed in the simplest form in terms of alloy hardness vs. particle size; such a diagram for a Ni-Cr-Ti-Al alloy is seen in Figure 2 (42). On the ascending curve, $\gamma'$ is cut by dislocations; on the descending curve, dislocation bypass the $\gamma'$ phase. The important factors which effect the extent of hardening are: anti-phase boundary and stacking fault

energy of $\gamma'$, solid-solution of $\gamma'$, coherency strains, volume fraction of $\gamma'$, $\gamma'$ particle size, diffusivity in $\gamma'$, $\gamma'$ phase stability and $\gamma$-$\gamma'$ modulus mismatch. These contributing factors are not additive. Specific details of strengthening mechanisms in superalloys are given by Decker (37) and Stoloff (38).

Factors that increase the strength of the nickel-base superalloy due to $\gamma'$ precipitation hardening are summarized as follows (37):

- increase volume fraction of $\gamma'$
- increase fault energy of $\gamma'$
- solid solution hardened $\gamma'$
- increase coherency strains for $T < 0.6$ TM
- decrease ripening rate for $T > 0.6$ TM

In addition to solid solution hardening of $\gamma$ and $\gamma'$ precipitation hardening, carbide particle morphology, grain boundary chemistry, TCP phase and grain size affect the strength of the nickel-base superalloy.

## APPENDIX C

## HEALING OF CASTING BY HOT ISOSTATIC PRESSING (HIP)

Microporosity and voids, the interval defects that have an adverse effect on mechanical properties and performance, are present in nickel-base superalloy castings. These interval defects can be minimized by adjusting composition and casting practice so as to increase the local pressure during solidification (71). However, hot isostatic pressing (HIP), which is routinely used to consolidate and manufacture near- net-shape parts from powders in P/M, has been found to be the only effective means of totally eliminating microporosity and voids in castings.

The HIP process collapses voids and porosity by creep or plastic deformation (72). It also diffusion bonds the surfaces of the collapsed areas and creates a fully dense casting. HIP also provides the metallurgical benefit of structural homogenization, reducing the chemistry gradients created by segregation of alloying constituents. Secondary phases are dissolved and reprecipitated in a manner peculiar to the cooling rate of the HIP unit. Primary phases, depending on composition, may also be altered (73).

HIP does not usually affect dimensions since the voids and pores are small. Typically porosity in casting can be eliminated as effectively in large castings as in small ones (74). However, HIP has a

limitation: it cannot heal surface connected porosity, e.g. the chilled surface of investment cast superalloys are generally leak-tight. Much work has been done to either eliminate such surface-connected porosity or to isolate it from the pressurizing medium (75). Occasionally this has been accomplished by fusion and weld sealing of the cut surfaces. A patented remedy, which has been extensively investigated and even patented, involves coating of the defective surfaces or encapsulation of superalloy castings in wrought containers (75). However, all of these are time consuming and can add significantly to the difficulty and cost of processing.

The HIP process has three principal variables - pressure, temperature and time. An inert gas, usually argon, is the pressurizing medium. Since pressures, ranging up to 200 MPa (30,000 psi), are applied isostatically (uniformly in all directions); parts of almost any shape including those with combinations of thick and thin cross sections can be HIP without distortion and with uniform properties throughout. Processing tempeature, which may be as high as 2000°C (3600°F), are within the plastic range of the material being formed - high enough for diffusion bonding to occur, yet low enough to prevent undesirable microstructural changes. Close temperature control is critical to success in HIPing. If temperatures are too high, incipient melting may occur which in turn may cause accelerated grain growth in superalloys. If temperatures are too low, voids and pores will not collapse. In a HIP cycle, sufficient time is also necessary to achieve full densification of the casting. After HIP cycle, the castings are cooled in the pressure vessel under an inert cover.

## APPENDIX D

## MECHANICAL PROPERTIES OF NICKEL-BASE TURBINE DISK SUPERALLOYS

### D-1. Tensile Properties

The tensile strength of nickel base superalloys is an important consideration at operating temperature less than 700°C (1300°F); however, as the operating temperature increases to above 700°C (1300°F), the creep strength becomes more important than tensile strength (77). The mechanical properties at temperatures less than 700°C (1300°F) are reviewed in this section.

Nickel-base superalloys are essentially a Ni/Cr solid solution alloy hardened by additions of Al and Ti to precipitate in the $\gamma'$ phase, $Ni_3(Al,Ti)$. The strengthening mechanisms of the solid-solution hardening of $\gamma$ and precipitation hardening of $\gamma'$ has been reviewed briefly in the previous section A-3.

The role of carbides in superalloys is a complex phenomenon; the carbides appear to nucleate preferentially at grain boundaries location in nickel base superalloys. Certain grain boundary carbide morphologies have been noted to have detrimental effects on ductility and thus efforts are taken to reduce the carbon levels (41). Carbides do play a major role in the make-up of superalloys. At the grain boundaries the carbides have a significant and beneficial effect for high temperature strength and the carbide morphology influences the ductility level of the alloy.

MC carbides are dense and very strong and will transform to $M_{23}C_6$ or M6C carbides during cooling or heat treating. $M_{23}C_6$ carbides have a significant effect on nickel alloy properties. A continuous grain boundary $M_{23}C_6$ film results in poor ductility. Cracks usually initiate either by fracture of these grain boundary $M_{23}C_6$ or by decohesion of the $M_{23}C_6$-$\gamma$ interface. In addition, cellular $M_{23}C_6$ has been reported to cause rapid crack propagation and premature failure (78). In contrast, the intergranular-$\gamma'$ coated blocky $M_{23}C_6$ is associated with a significantly better combination of strength and ductility (79). Surrounding the hard grain boundary carbides with $\gamma'$ phase allows controlled slip which inhibits the onset of intergranular fracture (80). $M_6C$ carbides are stable at higher temperature than $M_{23}C_6$ carbides, therefore, $M_6C$ is more beneficial as a grain boundary precipitate to control grain size in wrought alloys. However, the Widmanstatten $M_6C$ phase should be avoided for an acceptable level of ductility.

Raymond studied the effect of grain boundary denudation of $\gamma'$ on notch-rupture ductility of Inconel alloys X-750 and 718 (81). The presence of a $\gamma'$ denuded zone adjacent to the grain boundaries is a consequence of solute depletion caused by precipitation of carbides in the grain boundaries. Raymond (81) and Decker (79) showed that in the absence of these denuded zones, there is evidence of intergranular $\gamma'$ deformation. In contrast, in the presence of denuded zones, intergraunular $\gamma'$ deformation was not seen and a high density of dislocations were observed in the denuded zones which makes the material notch-brittle.

In nickel-based superalloys, the addition of elements such as B, Zr and Mg offer alternative approaches to retard grain boundary diffusion by grain boundary segregates. B, Zr and Mg segregate at grain boundaries and it should be noted that there is a large difference in their atomic diameter with respect to nickel - 21-29% over or undersize (82). However, Antony et al. (71) has shown that B and Zr influence the solidification range of these alloys such that the level of microporosity is increased.

Sigma and other TCP phases (μ and Laves) have a specific and detrimental effect on properties of the alloy. Their plate-like configuration act as crack initiation sites leading to low-temperature brittle failure (83). They contain a high refractory metal content, which depletes the γ matrix, resulting in alloy weakening (37).

The tensile properties of superalloys is also greatly affected by the grain size of the alloy. As will be seen in this work, the grain size of cast nickel base superalloys can be controlled through processing such as in rheocasting and VADER. For a given aging sequence, Gayda et al. (84) have shown that the yield strength increased significantly with decreasing grain size at testing temperatures of 650°C. The ultimate tensile strength also exhibits similar behavior but the effect is less pronounced than that for the yield strength. Alloy ductility and strength were seen to exhibit opposing trends.

Many cast nickel-base superalloys respond favorably to HIPing. As a result of the investigations with cast hafnium modified IN 792. Wasielewski et al. (85) showed that HIP densification can result in significant improvements in tensile strength and elongation through the elimination of shrinkage and hot tears. The improvement in tensile

properties through HIPing make it possible to employ nickel-base superalloy castings in highly stressed critical applications.

D-2 Fatigue Crack Propagation (FCP) Rates

Nickel-base superalloys, used in stationary turbines, generally exhibit 3 regimes of FCP behavior (88). Low levels of $\Delta K$ (stress-intensity factor range) is generally responsible for propagation rates of less than $10^{-8}$m.cycles$^{-1}$, while at high levels of $\Delta K$ the maximum stress-intensity factor, $k_{max}$, approaches the critical failure stress-intensity value or $K_C$. In the mid $\Delta K$ regime, FCP rates are commonly described by the Paris-Erdogan law (86):

$$da/dn = C\Delta K^m$$

a: crack length

n: number of cycles

$\Delta K$: stress-intensity-factor range ($\Delta K = K_{max} - K_{min}$)

C,m: function of testing conditions

The R ratio is the ratio of the minimum stress intensity factor to that of the maximum value, kmin/kmax; all three regions of FCP are influenced by the magnitude of the R ratio. However, the R ratio effect is more pronounced in high and low levels of $\Delta K$ than in the medium level $\Delta K$ region (89). For all the blade and disk materials, Holdsworth et al. (87) showed that increasing R ratio from 0.1 to 0.8 resulted in a

reduction of crack growth rate. A similar result was also obtained by Wei (90) for R ratio increasing from 0.05 to 0.9.

The effect of frequency and wave form on the FCP behavior have been studied by Clavel et al. (91) on Inconel 718 alloy at a temperature of 550°C (1000°F). It was concluded that the FCP rate at 550°C (1000°F) was increased by a decrease in frequency from 20 to $5 \times 10^{-3}$ Hz. This increase in fatigue crack propagation rate with decreasing frequency was suggested to have occurred with a transition in the fracture mode which became progressively more intergranular as the frequency was decreased. Moreover, the examination by Clavel et al. (91) on the substructures present in the fatigue plastic zones showed that the increase in strain rate, obtained either by increased frequency or by using square wave shape stress cycling, promoted a more homogeneous plastic deformation as compared to that occurring at lower strain rates obtained either by decreasing the frequency or by using transgranular wave shape stress cycling. The trend to intergranular crack growth at lower frequency has been noted by Merrick et al. (92).

Clavel et al. (91) have evaluated the effect of temperature on the FCP rate of Inconel 718 in air. It was found that FCP rate was accelerated, particularly at low stress intensity levels, by an increase in temperature. Macha (93) has confirmed this temperature effect by examining the FCP retardation behavior of IN-100 superalloy. It was suggested that high temperature oxidation made a great contribution to the increasing propagation rate (93,94). Due to oxidation of the grain boundaries in the elevated temperature air environment, the mode of crack propagation changed from transgranular at room temperature to

intergranular at high temperature. However, in the high ΔK range, the mechanical properties of the bulk material would dominate the crack growth behavior.

It is a known fact that the environment can seriously affect the elevated temperature crack growth in nickel-base superalloys. Air, in particular, is recognized as being aggressive, when compared to vacuum or inert gas environment (95). However, the environment has also been suspected of increasing the rate of crack propagation when frequency is reduced in high temperature fatigue test (86).

The influence of 14 different gas environments on the FCP rate of Inconel alloy 718 at 650°C (1200°F) has been studied by Floreen and Kane (96). The results of this study showed that the presence of oxygen or sulfur-bearing species in a gas environment produces large increases in the FCP rate at 650°C. Even minor amounts of either species in the environment produces significant affects. It was concluded that there was a marked enhancement of intergranular crack growth rate in each case (96). Floreen et al. (97) and Gayda et al. (84) also showed that the FCP rate at 650°C was higher when tested in air than in helium or vacuum.

Numerous investigations have been carried out (71,84,92,97-104) to evaluate the effects of microstructure on FCP rate if nickel base superalloy were tested at intermediate temperatures in air. The microstructures which have been studied, include grain size, γ' particle size and grain boundary phases.

Studies by Cowles et al. (101) and Gayda et al. (99,100) to examine the fatigue behavior at 650°C of several nickel-base disk alloys,

including Waspaloy, Astroloy, MERL 76, IN-100, Rene 95 and NASA IIB-7, showed that the higher strength, fine grain size alloys possessed longer total fatigue life at low strain ranges of interest in disk applications. However, these high strength fine grain alloys were also the least resistant to fatigue crack propagation at 650°C. A complete fractographic analysis of these samples was conducted by Gayda et al. (99); it was shown that the rapid crack propagation rates exhibited by the high strength, fine grain alloys were associated with an intergranular failure mode, while the slow crack propagation rates of the low strength, coarse grain alloys were associated with a transgranular failure mode. It was suggested that these crack propagation might be linked to environmental embrittlement and/or creep damage associated with a grain size. Earlier reports by Merrick et al. (92) and Floreen et al. (102) also showed that a coarse grain size is beneficial to crack growth resistance. Recently, Gayda et al. (84) have further studied the effect of grain size on 650°C fatigue crack propagation in P/M Astroloy. For a given $\Delta K$, the crack growth rates were found to be inversely related to the product of strength and to the half power of grain size. Transitional crack propagation behavior was obtained with an intermediate grain size (20μm). A fine grain size (<20μm) promoted rapid intergranular crack propagation which was virtually unaffected by variations in strength, while a coarse grain size (>20 μm) promoted slower , transgranular crack growth which decreased with increasing strength.

A study on the FCP at 650°C in Waspaloy by Merrick and Floreen (92) showed that changes in $\gamma'$ size and distribution did not markedly

affect fatigue crack propagation. However, Gayda and Miner in their recent paper (84) concluded that for the coarse grain microstructure (>20μm) of P/M Astroloy, the FCP rate tend to decrease with decreasing γ' size or increasing volume fraction of fine γ'.

Runkle and Pelloux (98) have investigated the effect of grain boundary phases on the FCP in Astroloy at various temperatures. They concluded that serrated grain boundaries were beneficial in minimizing grain boundary sliding and lowering grain boundary cracking growth rates. The most effective serrated grain boundaries were produced by both coarse intergranular carbides and primary γ'. However, Merrick and Floreen (92), based on the observation of fatigue crack behavior in nickel-base superalloy at 650°C, stated that serrated grain boundaries improved the crack growth in creep but appeared to have little effect on either FCP rate.

The FCP rate was also influenced by the existence of the grain boundary primary γ' denuded zone. Hwang and Pande (104) showed that a pronounced grain boundary cavitation took place along primary γ' denuded zones and that grain boundary sliding was the responsible mechanism for the cavitation.

| 1. Report No. | 2. Government Accession No. | 3. Recipient's Catalog No. |
|---|---|---|
| NASA CR-175014 | | |

| 4. Title and Subtitle | 5. Report Date |
|---|---|
| Structure-Property Characterization of Rheocast and VADER Processed IN-100 Superalloy | June 1985 |
| | 6. Performing Organization Code |
| 7. Author(s) | 8. Performing Organization Report No. |
| Jung-Jen Allen Cheng and Diran Apelian | None |
| | 10. Work Unit No. |
| 9. Performing Organization Name and Address | 11. Contract or Grant No. |
| Drexel University<br>Philadelphia, Pennsylvania | NAG 3-14 |
| | 13. Type of Report and Period Covered |
| 12. Sponsoring Agency Name and Address | Contractor Report |
| National Aeronautics and Space Administration<br>Washington, D.C. 20546 | 14. Sponsoring Agency Code |
| | 505-63-01 |

15. Supplementary Notes

Final Report. Project Manager, T.K. Glasgow, Materials Division, NASA Lewis Research Center, Cleveland, Ohio. This report was submitted in partial fulfillment of the requirements for the degree Doctor of Philosophy to Drexel University, Philadelphia, PA June 1985.

16. Abstract

Two recent solidification processes have been applied in the production of IN-100 nickel-base superalloy: rheocasting and vacuum arc double electrode remelting (VADER). A detailed microstructural examination has been made of the products of these two processes; associated tensile strength and fatigue crack propagation (FCP) rate at an elevated temperature were evaluated. In rheocasting, processing variables that have been evaluated include stirring speed, isothermal stirring time and volume fraction solid during isothermal stirring. VADER processed IN-100 was purchased from Special Metals Corp., New Hartford, NY. As-cast ingots were subjected to hot isostatic pressing (HIP) and heat treatment. Both rheocasting and VADER processed materials yield fine and equiaxed spherical structures, with reduced macrosegregation in comparison to ingot materials. The rheocast structures are discussed on the basis of the Vogel-Doherty-Cantor model of dendrite arm fragmentation. The rheocast ingots evaluated were superior in yield strength to both VADER and commercially cast IN-100 alloy. Rheocast and VADER ingots may have higher crack propagation resistance than P/M processed material.

| 17. Key Words (Suggested by Author(s)) | 18. Distribution Statement |
|---|---|
| Superalloys; Fatigue; Casting | Unclassified - unlimited<br>STAR Category 26 |

| 19. Security Classif. (of this report) | 20. Security Classif. (of this page) | 21. No. of pages | 22. Price* |
|---|---|---|---|
| Unclassified | Unclassified | 233 | A11 |

*For sale by the National Technical Information Service, Springfield, Virginia 22161